Mathematical Problems in Engineering

Advanced Techniques for Networked Systems with Applications

Guest Editors: Zhiyong Chen, Haitao Zhang, Lijun Zhu, Steffi Knorn, and Zhao Cheng

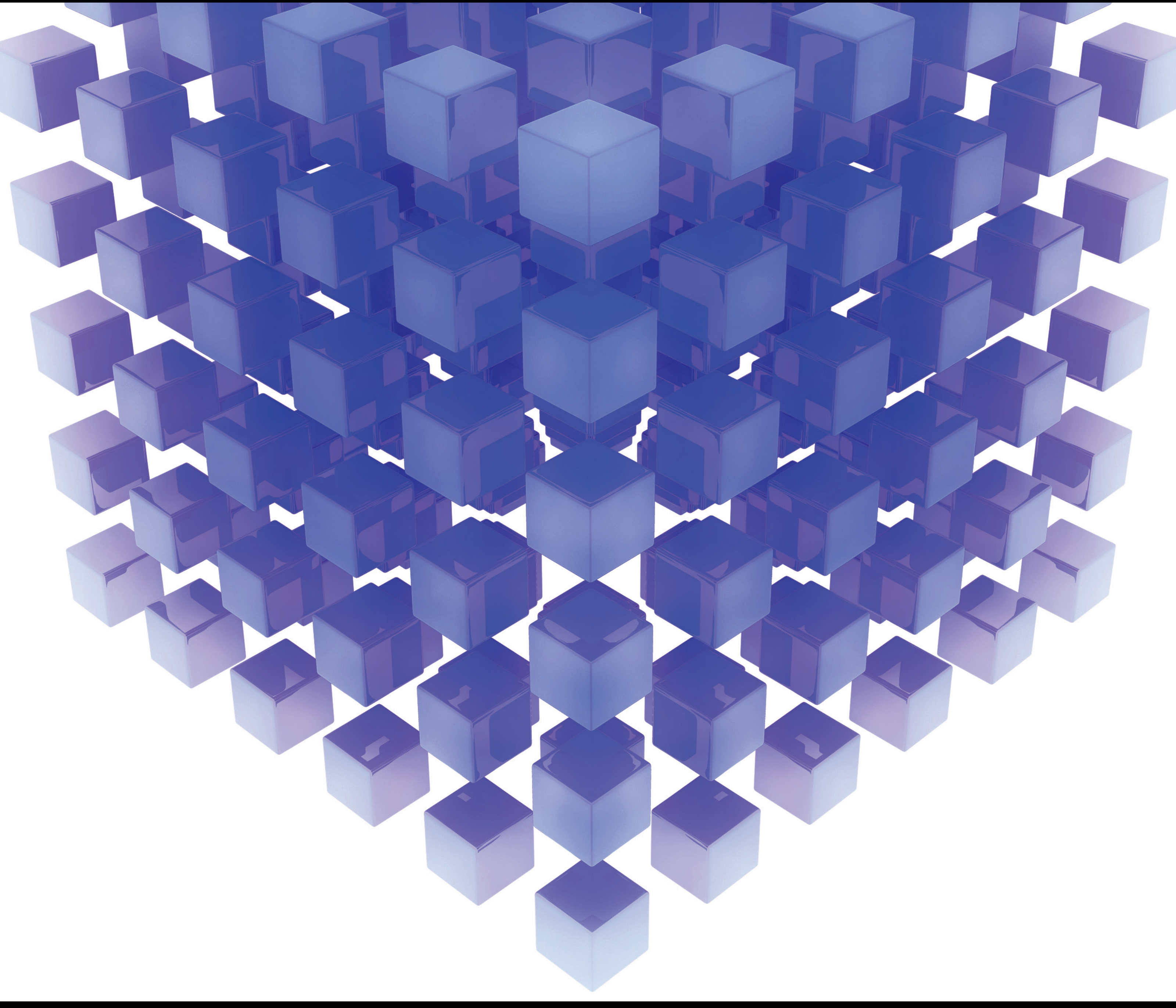

Advanced Techniques for Networked Systems with Applications

Mathematical Problems in Engineering

Advanced Techniques for Networked Systems with Applications

Guest Editors: Zhiyong Chen, Haitao Zhang, Lijun Zhu, Steffi Knorn, and Zhao Cheng

Editorial Board

Contents

Hindawi
Mathematical Problems in Engineering
Volume 2017, Article ID 3849019, 2 pages
https://doi.org/10.1155/2017/3849019

Editorial

Advanced Techniques for Networked Systems with Applications

Zhiyong Chen,[1] Haitao Zhang,[2] Lijun Zhu,[3] Steffi Knorn,[4] and Zhao Cheng[5]

[1] *School of Electrical Engineering and Computer Science, University of Newcastle, Callaghan, NSW, Australia*
[2] *Department of Control Science and Engineering, Huazhong University of Science and Technology, Wuhan, China*
[3] *Department of Electrical and Electronic Engineering, University of Hong Kong, Pokfulam, Hong Kong*
[4] *Department of Engineering Sciences, Uppsala University, Uppsala, Sweden*
[5] *Thayer School of Engineering, Dartmouth College, Hanover, NH, USA*

Correspondence should be addressed to Zhiyong Chen; zhiyong.chen@newcastle.edu.au

Received 13 December 2016; Accepted 15 December 2016; Published 12 April 2017

Cooperative control of networked systems is a fast-growing field, in which mathematical methods are typically used to investigate the theories and algorithms that address efficiency, availability, and robustness of networked systems. Main aspects of rich collaborative behaviors of networked systems include agent dynamics, network communication, and interagent dynamic coupling.

The objective of this special issue is for scientists, engineers, and practitioners to present their latest theoretical and technological achievements on networked systems. It aims at identifying sound theoretical foundation and promising technological solutions to analysis, control, and applications of networked systems.

This special issue has received many submissions. The authors of the papers submitted to this special issue are from Canada, China, Iran, Korean, United Kingdom, United State, Vietnam, and so on. After rigorous peer-review process, six papers have been accepted for publication. These papers present recent research processes in multirobot cooperation control, fault detection, and network communication. The acceptance rate of this special issue is 13%.

In the field of multirobot cooperative control, C. Ruan et al. develop a method to form robust synchronization in the networked system of unmanned combat aerials vehicles (UCAVs). The route temporary blind avoidance (RTBA) model is proposed to prevent the combat aerials vehicles from physical and functional bind. The synchronization is achieved through maximizing the efficiency of UCAV formation in terms of connectivity and delay robustness.

C. Peng et al. investigate the attitude motion synchronization problem for multiple robotic helicopters with three degrees of freedom. The directed graph is used to model the communication topology for the multirobot system. Stability and tracking performance of the whole network is improved by estimating the expected control term and the synchronization error in each individual robot with a finite-time convergent estimator.

Chaotic time series prediction is a challenging problem for neural networks due to its uncertainty. Q. Li and R.-C. Lin Chaotic propose the self-constructing fuzzy neural network (SCFNN) for time series prediction. This SCFNN extends from the fuzzy neural network by conducting the structure learning and parameter learning concurrently and can achieve similar performance with less number of hidden layer nodes.

In order to provide quality-adaptive mobile video streaming services in MIMO-capable heterogeneous wireless access networks, H. Oh extends from the FMIPv6 method whose performance is affected due to large prediction inaccuracy in the case of sudden direction change of the mobile nodes. By optimizing video quality and handover delayer with more appropriate selected metrics, the proposed method is able to provide quality-adaptive service for handing over and forwarding mobile video streaming in MIMO-capable heterogeneous wireless access networks.

X. Ren and M. He developed the Appropriate Degree Gossip Detection (ADGD) which discovers faulty links and peers through depth-first search on the peer degree. In addition, a routing failure restoration strategy (RFRS) that handles single-link failure, multilink failure, and peer failure is proposed to improve the reliability of the P2P dynamic systems.

In addition, N. H. A. Nguyen et al. address stability analysis and control synthesis for the semi-Markovian Jump systems (S-MJSs) with the more applicable feature, uncertain probability intensity. The boundary constraints of the probability intensity are discussed and they are related to the basis of time-varying transition rates. The authors also investigate the effectiveness of the control design of the S-MJSs.

Acknowledgments

We appreciate the authors for their contributions to this special issue. Special thanks to the reviewers for their valuable feedback, which helps improve the quality of the papers submitted.

Zhiyong Chen
Haitao Zhang
Lijun Zhu
Steffi Knorn
Zhao Cheng

Hindawi Publishing Corporation
Mathematical Problems in Engineering
Volume 2016, Article ID 8417475, 12 pages
http://dx.doi.org/10.1155/2016/8417475

Research Article

Stabilization of Semi-Markovian Jump Systems with Uncertain Probability Intensities and Its Extension to Quantized Control

Ngoc Hoai An Nguyen,[1] Sung Hyun Kim,[1] and Jun Choi[2]

[1] *School of Electrical Engineering, University of Ulsan, Daehak-ro 93, Nam-Gu, Ulsan 680-749, Republic of Korea*
[2] *Korea Institute of Industrial Technology, Jongga-ro 55, Jung-gu, Ulsan 44413, Republic of Korea*

Correspondence should be addressed to Sung Hyun Kim; ie222.kim@gmail.com

Received 19 July 2016; Accepted 1 November 2016

Academic Editor: Haitao Zhang

This paper concentrates on the issue of stability analysis and control synthesis for semi-Markovian jump systems (S-MJSs) with uncertain probability intensities. Here, to construct a more applicable transition model for S-MJSs, the probability intensities are taken to be uncertain, and this property is totally reflected in the stabilization condition via a relaxation process established on the basis of time-varying transition rates. Moreover, an extension of the proposed approach is made to tackle the quantized control problem of S-MJSs, where the infinitesimal operator of a stochastic Lyapunov function is clearly discussed with consideration of input quantization errors.

1. Introduction

Over the past few decades, considerable attention has been paid to Markovian jump systems (MJSs) since such systems are suitable for representing a class of dynamic systems subject to random abrupt variations. In addition to the growing interest from their representation ability, MJSs have been widely applied in many practical applications, such as manufacturing systems, aircraft control, target tracking, robotics, networked control systems, solar receiver control, and power systems (see [1–9] and references therein). Following this trend, numerous investigations are underway to deal with the issue of stability analysis and control synthesis for MJSs with complete/incomplete knowledge of transition probabilities in the framework of filter and control design problems: [10–13] with a complete description of transition rates and [14–20] without a complete description. Generally, in MJSs, the sojourn-time is given as a random variable characterized by the continuous exponential probability distribution, which tends to make the transition rates time-invariant due to the memoryless property of the probability distribution. The thing to be noticed here is that the use of constant transition rates plays a limited role in representing a wide range of application systems (see [21–23]). Thus, another interesting topic has recently been studied in semi-Markovian jump systems (S-MJSs) to overcome the limitation of this memoryless property.

As reported in [24–26], the mode transition of S-MJSs is driven by a continuous stochastic process governed by the nonexponential sojourn-time distribution, which leads to the appearance of time-varying transition rates. Thus, it has been well recognized that S-MJSs are more general than MJSs in real situations. Further, with this growing recognition, various problems on S-MJSs have been widely studied for successful utilization of a variety of practical applications (see [21, 22, 25, 27–29] and references therein). Of them, the first attempt to overcome the limits of MJSs was made by [21, 22] for the stability analysis of systems with phase-type (PH) semi-Markovian jump parameters, which was extended to the state estimation and sliding mode control by [29]. Besides, [25] considered the Weibull distribution for the stability analysis of S-MJSs and introduced a sojourn-time partition technique to make the derived stability criterion less conservative. Continuing this, [28] applied the sojourn-time partition technique to the design of $\mathscr{H}_\infty$ state-feedback control for S-MJSs with time-varying delays. After that, another partition technique of dividing the range of transition rates was proposed by [27] to derive the stability and stabilization conditions of S-MJSs with norm-bounded uncertainties. Most recently, [30] designed a reliable mixed passive and $\mathscr{H}_\infty$ filter for semi-Markov jump delayed systems with randomly occurring uncertainties and sensor failures. Also, [26] considered semi-Markovian switching and random measurement while designing a sliding mode control for networked control systems (NCSs). Based on the above observations, it can be found that their key issue mainly lies in finding more applicable transition models for S-MJSs, capable of a broad range of cases. In this light, one needs to explore the impacts of uncertain probability intensities in the study of S-MJSs and then provide a relaxed stability criterion absorbing the property of the resultant time-varying transition rates. However, until now, there have been almost no studies that intensively establish a kind of relaxation process corresponding to the stabilization problem of S-MJSs with uncertain probability intensities.

This paper addresses the issue of stability analysis and control synthesis for S-MJSs with uncertain probability intensities. One of our main contributions is to discover more reliable and scalable transition models for S-MJSs on the basis of their time-varying and boundary properties. To this end, this paper provides a valuable theoretical approach of constructing practical transition models for S-MJSs (1) by taking into account uncertain probability intensities and (2) by reflecting their available bounds in the transition rate description. Further, in a different manner from other works, all constraints on time-varying transition rates are totally incorporated into the stabilization condition via a relaxation process established on the basis of time-varying transition rates. Here, it is worth noticing that our relaxation process is developed in such a way that all possible slack variables can be included therein. In contrast to other works, our relaxation process plays a key role in obtaining a finite and solvable set of linear matrix inequalities (LMIs) from parameterized matrix inequalities (PLMIs) arising from uncertain probability intensities. On the other hand, the quantization module that converts real-valued measurement signals into piecewise constant ones has been commonly used to implement a variety of networked control systems over wired or wireless communications (see [31, 32]). Especially among optical wireless communications, the visible light communication can be applied as a data communication channel to transmit the control input to the S-MJSs under consideration. Thus, as an extension, this paper tackles the quantized control problem of S-MJSs, where the infinitesimal operator of a stochastic Lyapunov function is clearly discussed with consideration on input quantization errors. In addition, this paper proposes a method for reducing the influence of input quantization errors in the control of S-MJSs, which is also one of our main contributions. Finally, simulation examples show the effectiveness of the proposed method.

Notation. The notations $X \geq Y$ and $X - Y$ means that $X - Y$ is positive semidefinite and positive definite, respectively. In symmetric block matrices, $(*)$ is used as an ellipsis for terms induced by symmetry. For any square matrix $\mathcal{Q}$, $\mathbf{He}[\mathcal{Q}] = \mathcal{Q} + \mathcal{Q}^T$. For $\mathbb{N}_s^+ \triangleq \{1, 2, \ldots, s\}$,

$$
\begin{aligned}
\left[\mathcal{Q}_i\right]_{i\in\mathbb{N}_s^+} &\triangleq \left[\mathcal{Q}_1 \mathcal{Q}_2 \cdots \mathcal{Q}_s\right], \\
\left[\mathcal{Q}_{ij}\right]_{i,j\in\mathbb{N}_s^+} &\triangleq \begin{bmatrix} \mathcal{Q}_{11} & \cdots & \mathcal{Q}_{1s} \\ \vdots & \ddots & \vdots \\ \mathcal{Q}_{s1} & \cdots & \mathcal{Q}_{ss} \end{bmatrix}, \\
\left[\mathcal{Q}_i\right]^{\mathbf{D}}_{i\in\mathbb{N}_s^+} &\triangleq \begin{bmatrix} \mathcal{Q}_1 & 0 & \cdots & 0 \\ 0 & \mathcal{Q}_2 & \ddots & \vdots \\ \vdots & \ddots & \ddots & 0 \\ 0 & \cdots & 0 & \mathcal{Q}_s \end{bmatrix}, \\
\left[\mathcal{Q}_{ij}\right]^{\mathbf{U}}_{i,j\in\mathbb{N}_s^+} &\triangleq \begin{bmatrix} 0 & \mathcal{Q}_{12} & \mathcal{Q}_{13} & \cdots & \mathcal{Q}_{1s} \\ 0 & 0 & \mathcal{Q}_{23} & \cdots & \mathcal{Q}_{2s} \\ \vdots & \ddots & \ddots & \ddots & \vdots \\ 0 & \cdots & \cdots & 0 & \mathcal{Q}_{(s-1)s} \\ 0 & \cdots & \cdots & 0 & 0 \end{bmatrix},
\end{aligned} \tag{1}
$$

where $\mathcal{Q}_i$ and $\mathcal{Q}_{ij}$ denote real submatrices with appropriate dimensions or scalar values. The notation $\mathbf{E}[\bullet]$ denotes the mathematical expectation and $\mathrm{diag}(\bullet)$ stands for a block-diagonal matrix. The notation $\lambda_{\max}(\bullet)$ denotes the maximum eigenvalue of the argument, and $\exp(\bullet)$ indicates the exponential distribution.

2. System Description

Let us consider the following continuous-time semi-Markovian jump linear systems (S-MJSs):

$$\dot{x}(t) = A(\zeta(t))x(t) + B(\zeta(t))u(t), \tag{2}$$

where $x(t) \in \mathbb{R}^{n_x}$ and $u(t) \in \mathbb{R}^{n_u}$ denote the state and the control input, respectively. Here, $\{\zeta(t), t \geq 0\}$ denotes a continuous-time semi-Markov process that takes values in the finite space $\mathbb{N}_s^+$ and further has the mode transition probabilities:

$$
\begin{aligned}
&\mathbf{Pr}(\zeta(t+h) = j \mid \zeta(t) = i) \\
&\quad = \begin{cases} \pi_{ij}(h)h + o(h), & \text{if } j \neq i \\ 1 + \pi_{ii}(h)h + o(h), & \text{if } j = i, \end{cases}
\end{aligned} \tag{3}
$$

where $\lim_{h\to 0}(o(h)/h) = 0$ and $\pi_{ij}(h)$ denotes the transition rate from mode i to mode j at time $t+h$. Further, h indicates the sojourn-time elapsed when the system stays at mode i from the last jump (i.e., h is set to 0 when the system jumps).

In particular, the transition rate matrix $\prod(h) \triangleq [\pi_{ij}(h)]_{i,j\in\mathbb{N}_s^+}$ belongs to the following set:

$$\mathcal{S}_{\Pi}^{(1)} \triangleq \left\{ \left[\pi_{ij}\right]_{i,j\in\mathbb{N}_s^+} \mid 0 = \sum_{j\in\mathbb{N}_s^+} \pi_{ij},\ 0 \le \mu_{ij}\pi_{ij}, \text{ where } \mu_{ij}\big|_{j\neq i} = 1,\ \mu_{ij}\big|_{j=i} = -1,\ \forall i, j \in \mathbb{N}_s^+ \right\}. \quad (4)$$

Before going ahead, for later convenience, we define the system matrix for the ith mode as $(A_i, B_i) \triangleq (A(\zeta_k = i), B(\zeta_k = i))$, and set $\prod_i(h) \triangleq [\pi_{i1}(h) \ \ \cdots \ \ \pi_{is}(h)]^T = [\pi_{ij}(h)]_{j\in\mathbb{N}_s^+}^T$. Also, to deal with the stability analysis problem in such a stochastic setting, we consider the following definition.

Definition 1. An S-MJS (2) with $u(t) = 0$ is stochastically stable if its solution is such that, for any initial condition x_0 and ζ_0,

$$\lim_{t\to\infty} \mathbf{E}\left[\int_0^t \|x(\tau)\|^2 d\tau \mid x_0, \zeta_0\right] < \infty. \quad (5)$$

3. Stochastic Stability Analysis

First of all, let us consider (2) with $u(t) \equiv 0$:

$$\dot{x}(t) = A(\zeta(t))\, x(t). \quad (6)$$

The following lemma presents the stochastic stability condition for (6) with $\prod(h) \in \mathcal{S}_{\Pi}^{(1)}$.

Lemma 2. *Suppose that there exists $P_i > 0$, for all $i \in \mathbb{N}_s^+$, such that*

$$0 > \mathcal{Q}_i(h), \quad \prod(h) \in \mathcal{S}_{\Pi}^{(1)}, \quad \forall i \in \mathbb{N}_s^+, \quad (7)$$

where $\mathcal{Q}_i(h) \triangleq \mathbf{He}(P_iA_i) + \sum_{j=1}^s \pi_{ij}(h)P_j$. Then, S-MJSs (6) with $\prod(h) \in \mathcal{S}_{\Pi}^{(1)}$ are stochastically stable.

Proof. Let us consider a stochastic Lyapunov function candidate of the following form:

$$V(x(t), \zeta(t)) (= V(t)) = x^T(t)\, P(\zeta(t))\, x(t), \quad (8)$$

where $P(\zeta(t))$ is taken to be positive definite. Then, the infinitesimal generator ∇ of the stochastic process $\{x(t), \zeta(t), t \ge 0\}$ acting on $V(t)$ is given by

$$\begin{aligned}\nabla V(t) &= \lim_{\Delta\to 0} \frac{\mathbf{E}\left[V\left(x(t+\Delta), \zeta(t+\Delta) = j \mid x(t), \zeta(t) = i\right)\right] - V(x(t), r(t))}{\Delta} \\ &= \lim_{\Delta\to 0} \frac{1}{\Delta}\left[\sum_{j=1}^s p_{ij}(t,\Delta)\, x^T(t+\Delta) P_j x(t+\Delta) - x^T(t) P_i x(t)\right] = \Psi_1(t) + \Psi_2(t) + \Psi_3(t),\end{aligned} \quad (9)$$

where $p_{ij}(t,\Delta) = \mathbf{Pr}(\zeta(t+\Delta) = j \mid \zeta(t) = i)$,

$$\begin{aligned}\Psi_1(t) &\triangleq \lim_{\Delta\to 0} \frac{1}{\Delta} \sum_{j=1,\, j\neq i}^s p_{ij}(t,\Delta)\, x^T(t+\Delta) P_j x(t+\Delta), \\ \Psi_2(t) &\triangleq \lim_{\Delta\to 0} \frac{1}{\Delta} p_{ii}(t,\Delta)\, x^T(t+\Delta) P_i x(t+\Delta), \\ \Psi_3(t) &\triangleq \lim_{\Delta\to 0} \frac{1}{\Delta} \left(-x^T(t) P_i x(t)\right).\end{aligned} \quad (10)$$

Here, the probabilities $p_{ij}(t,\Delta)$ and $p_{ii}(t,\Delta)$ are described as

$$\begin{aligned}p_{ij}(t,\Delta) &= \frac{\mathbf{Pr}(\zeta(t+\Delta) = j, \zeta(t) = i)}{\mathbf{Pr}(\zeta(t) = i)} \\ &= \frac{q_{ij}(G_i(h+\Delta) - G_i(h))}{1 - G_i(h)}, \quad \forall j \neq i,\end{aligned} \quad (11)$$

$$\begin{aligned}p_{ii}(t,\Delta) &= \frac{\mathbf{Pr}(\zeta(t+\Delta) = i, \zeta(t) = i)}{\mathbf{Pr}(\zeta(t) = i)} \\ &= \frac{1 - G_i(h+\Delta)}{1 - G_i(h)},\end{aligned} \quad (12)$$

where $G_i(h)$ denotes the cumulative distribution function of the sojourn-time h at mode i and q_{ij} stands for the probability intensity such that $\sum_{j=1,\, j\neq i}^s q_{ij} = 1$ and $q_{ii} = -1$. Especially in (11), the probability intensity q_{ij} is taken to have uncertainties. Meanwhile, from (6), it follows that $x(t+\Delta) = (A_i\Delta + I)x(t)$, for $\Delta \to 0$, which leads to

$$\begin{aligned}&x^T(t+\Delta) P_j x(t+\Delta) \\ &= x^T(t) \left(A_i\Delta + I\right)^T P_j \left(A_i\Delta + I\right) x(t) \\ &= x^T(t) \left(\Delta^2 \cdot A_i^T P_j A_i + \Delta \cdot \mathbf{He}\left(P_jA_i\right) + P_j\right) x(t).\end{aligned} \quad (13)$$

That is, from (11) and (12), it is clear that

$$\lim_{\Delta\to 0}\frac{1}{\Delta}p_{ij}(t,\Delta)x^T(t+\Delta)P_jx(t+\Delta) = \lim_{\Delta\to 0}p_{ij}(t,\Delta)x^T(t)\mathbf{He}(P_jA_i)x(t) + \lim_{\Delta\to 0}\frac{1}{\Delta}p_{ij}(t,\Delta)x^T(t)P_jx(t). \tag{14}$$

Thus, using (14), $\Psi_1(t)$ and $\Psi_2(t)$ become

$$\begin{aligned}\Psi_1(t) &= \sum_{j=1,\, j\neq i}^{s}\lim_{\Delta\to 0}p_{ij}(t,\Delta)x^T(t)\mathbf{He}(P_iA_i)x(t) + \lim_{\Delta\to 0}\frac{1}{\Delta}\sum_{j=1,\, j\neq i}^{s}p_{ij}(t,\Delta)x^T(t)P_jx(t)\\ &= \lim_{\Delta\to 0}\frac{1}{\Delta}\sum_{j=1,\, j\neq i}^{s}p_{ij}(t,\Delta)x^T(t)P_jx(t),\\ \Psi_2(t) &= \lim_{\Delta\to 0}p_{ii}(t,\Delta)x^T(t)\mathbf{He}(P_iA_i)x(t) + \lim_{\Delta\to 0}\frac{1}{\Delta}p_{ii}(t,\Delta)x^T(t)P_ix(t)\\ &= x^T(t)\mathbf{He}(P_iA_i)x(t) + \lim_{\Delta\to 0}\frac{1}{\Delta}p_{ii}(t,\Delta)x^T(t)P_ix(t).\end{aligned} \tag{15}$$

That is, $\nabla V(t)$ becomes

$$\begin{aligned}\nabla V(t) &= \lim_{\Delta\to 0}\frac{1}{\Delta}\sum_{j=1,\, j\neq 1}^{s}p_{ij}(t,\Delta)x^T(t)P_jx(t) + x^T(t)\cdot\mathbf{He}(P_iA_i)x(t) + \lim_{\Delta\to 0}\frac{1}{\Delta}(p_{ii}(t,\Delta)-1)x^T(t)P_ix(t) = x^T(t)\\ &\cdot\Bigg\{\mathbf{He}(P_iA_i) + \lim_{\Delta\to 0}\frac{1}{\Delta}\Bigg(\sum_{j=1,\, j\neq i}^{s}p_{ij}(t,\Delta)P_j + (p_{ii}(t,\Delta)-1)P_i\Bigg)\Bigg\}\\ &\cdot x(t) = x^T(t)\Bigg\{\mathbf{He}(P_iA_i) + \lim_{\Delta\to 0}\frac{1}{\Delta}\Bigg(\sum_{j=1,\, j\neq i}^{s}q_{ij}P_j - P_i\Bigg)\frac{G_i(h+\Delta)-G_i(h)}{1-G_i(h)}\Bigg\}\\ &\cdot x(t) = x^T(t)\Bigg\{\mathbf{He}(P_iA_i) + \Bigg(\sum_{j=1,\, j\neq i}^{s}q_{ij}P_j - P_i\Bigg)\frac{g_i(h)}{1-G_i(h)}\Bigg\}x(t) = x^T(t)\\ &\cdot\Bigg\{\mathbf{He}(P_iA_i) + \Bigg(\sum_{j=1,\, j\neq i}^{s}q_{ij}P_j - P_i\Bigg)\pi_i(h)\Bigg\}x(t),\end{aligned} \tag{16}$$

where $\pi_i(h) = g_i(h)/1-G_i(h)$ denotes the transition rate of the system jumping from mode i. As a result, by defining $\pi_{ij}(h) = q_{ij}\pi_i(h)$, for $j \neq i$, and $\pi_{ii}(h) = -\sum_{j=1,\, j\neq i}^{s}\pi_{ij}(h) = -\pi_i(h)$, we have

$$\begin{aligned}\nabla V(t) &= x^T(t)\cdot\Bigg\{\mathbf{He}(P_iA_i) + \sum_{j=1,\, j\neq i}^{s}\pi_{ij}(h)P_j + \pi_{ii}(h)P_i\Bigg\}x(t)\\ &= x^T(t)\mathcal{Q}_i(h)x(t).\end{aligned} \tag{17}$$

In what follows, by the generalized Dynkin's formula [33], it is clear that

$$\begin{aligned}\mathbf{E}[V(t)] - V(0) &= \mathbf{E}\left[\int_0^t \nabla V(\tau)\,d\tau \mid x_0,\zeta_0\right]\\ &\leq \max_{i\in\mathbb{N}_s^+,\, 0\leq h\leq t}(\lambda_{\max}(\mathcal{Q}_i(h)))\cdot\mathbf{E}\left[\int_0^t \|x(\tau)\|_2^2\,d\tau \mid x_0,\zeta_0\right],\end{aligned} \tag{18}$$

which results in

$$\begin{aligned}&-\max_{i\in\mathbb{N}_s^+,\, 0\leq h\leq t}(\lambda_{\max}(\mathcal{Q}_i(h)))\cdot\mathbf{E}\left[\int_0^t \|x(\tau)\|_2^2\,d\tau \mid x_0,\zeta_0\right] \leq V(0) - \mathbf{E}[V(t)]\\ &\leq V(0).\end{aligned} \tag{19}$$

Thus, from (7), it follows that

$$\begin{aligned}&\lim_{t\to\infty}\mathbf{E}\left[\int_0^t \|x(\tau)\|_2^2\,d\tau \mid x_0,\zeta_0\right]\\ &\leq -\frac{V(0)}{\max_{i\in\mathbb{N}_s^+,\, 0\leq h}(\lambda_{\max}(\mathcal{Q}_i(h)))} < \infty.\end{aligned} \tag{20}$$

Finally, by Definition 1, the proof can be completed. □

In this paper, as a model of probability distribution for the sojourn-time $h \geq 0$, we utilize the Weibull distribution with shape parameter $\beta > 0$ and scale parameter $\alpha > 0$, since such a distribution has been witnessed as an appropriate choice for representing the stochastic behavior of practical systems. In other words, to represent the probability distribution of

h, its cumulative function $G_i(h)$ and probability distribution function $g_i(h)$ are given as follows: for all i and $j (j \neq i) \in \mathbb{N}_s^+$,

$$\begin{aligned} G_i(h) &= 1 - \exp\left(-\left(\frac{h}{\alpha_i}\right)^{\beta_i}\right), \\ g_i(h) &= \frac{\beta_i}{\alpha_i^{\beta_i}} h^{\beta_i - 1} \exp\left(-\left(\frac{h}{\alpha_i}\right)^{\beta_i}\right), \end{aligned} \tag{21}$$

which leads to

$$\pi_{ij}(h) = q_{ij}\pi_i(h) = q_{ij}\frac{g_i(h)}{1 - G_i(h)} = q_{ij}\frac{\beta_i}{\alpha_i^{\beta_i}} h^{\beta_i - 1}. \tag{22}$$

As a special case, let $\beta_i = 1$. Then, we can represent MJSs from (22); that is, the transition rate $\pi_{ij}(h)$ can be reduced to an h-independent value as follows: $\pi_{ij}(h) = q_{ij}\pi_i(h) = q_{ij}/\alpha_i$. Accordingly, it can be claimed that (22) expresses a more generalized transition model, compared to the case of MJSs.

Remark 3. As shown in (22), the transition rate $\pi_{ij}(h)$ is time-varying and depends on the probability intensity q_{ij}. Thus, to derive a finite number of solvable conditions from (7), there is a need to consider the lower and upper bounds of both $\pi_i(h)$ and q_{ij}, respectively, as follows: $\pi_{i,1} \leq \pi_i(h) \leq \pi_{i,2}$ and $q_{ij,1} \leq q_{ij} \leq q_{ij,2}$. Then, from $\pi_{ij}(h) = q_{ij}\pi_i(h)$, the bounds of $\pi_{ij}(h)$ are decided as follows: $\pi_{ij,1} \leq \pi_{ij}(h) \leq \pi_{ij,2}$, where

$$\begin{aligned} \pi_{ij,1} &= \begin{cases} q_{ij,1} \cdot \pi_{i,1}, & \text{if } j \neq i \\ -\pi_{i,2}, & \text{otherwise}, \end{cases} \\ \pi_{ij,2} &= \begin{cases} q_{ij,2} \cdot \pi_{i,2}, & \text{if } j \neq i \\ -\pi_{i,1}, & \text{otherwise}. \end{cases} \end{aligned} \tag{23}$$

In accordance with Remark 3, an auxiliary constraint can be established as follows: $\prod(h) \in \mathcal{S}_\Pi^{(2)}$, where

$$\mathcal{S}_\Pi^{(2)} \triangleq \left\{ \left[\pi_{ij}\right]_{i,j\in\mathbb{N}_s^+} \mid \pi_{ij,1} \leq \pi_{ij} \leq \pi_{ij,2},\ \forall i, j \in \mathbb{N}_s^+ \right\}. \tag{24}$$

The following lemma presents the stochastic stability condition for S-MJSs (6) with $\prod(h) \in \mathcal{S}_\Pi^{(1)} \cap \mathcal{S}_\Pi^{(2)}$.

Lemma 4. *Suppose that there exists $P_i > 0$, for all $i \in \mathbb{N}_s^+$, such that*

$$\begin{aligned} 0 &> \mathcal{Q}_i(h), \\ \prod(h) &\in \mathcal{S}_\Pi^{(1)} \cap \mathcal{S}_\Pi^{(2)}, \\ &\forall i \in \mathbb{N}_s^+, \end{aligned} \tag{25}$$

where $\mathcal{Q}_i(h) \triangleq \mathbf{He}(P_iA_i) + \sum_{j=1}^{s}\pi_{ij}(h)P_j$ and $\pi_{ij}(h) \in [\pi_{ij,1}, \pi_{ij,2}]$. Then, S-MJSs (6) with $\mathcal{S}_\Pi^{(1)} \cap \mathcal{S}_\Pi^{(2)}$ are stochastically stable.

However, it is worth noticing that solving (25) of Lemma 4 is still equivalent to solving an infinite number of LMIs, which is an extremely difficult problem. Thus, it is necessary to find a finite number of solvable LMI-based conditions from (25). To this end, the following theorem provides a relaxed stochastic stability condition for (6) with $\prod(h) \in \mathcal{S}_\Pi^{(1)} \cap \mathcal{S}_\Pi^{(2)}$.

Theorem 5. *Suppose that there exists matrices $\{G_i, S_{ij}, X_{ij}, Y_{ij}\}_{i,j\in\mathbb{N}_s^+} \in \mathbb{R}^{n_x\times n_x}$ and symmetric matrices $\{P_i > 0\}_{i\in\mathbb{N}_s^+} \in \mathbb{R}^{n_x\times n_x}$ such that*

$$0 > \left[\begin{array}{c|c} (1,1) & (1,2) \\ \hline (*) & (2,2) \end{array}\right], \quad \forall i \in \mathbb{N}_s^+, \tag{26}$$

$$0 \leq \mathbf{He}\left(X_{ij}\right), \quad \forall i, j \in \mathbb{N}_s^+, \tag{27}$$

$$0 \leq \mathbf{He}\left(Y_{ij}\right), \quad \forall i, j \in \mathbb{N}_s^+, \tag{28}$$

where $\mu_{ij}|_{j\neq i} = 1$, $\mu_{ij}|_{j=i} = -1$,

$$\begin{aligned} (1,1) &= \mathbf{He}\left(P_iA_i\right) - \sum_{j\in\mathbb{N}_s^+} \mathbf{He}\left(\pi_{ij,1}\pi_{ij,2}X_{ij}\right), \\ (1,2) &= \left[\frac{1}{2}P_j + G_i + \left(\pi_{ij,1} + \pi_{ij,2}\right)X_{ij} + \mu_{ij}Y_{ij}\right]_{j\in\mathbb{N}_s^+}, \\ (2,2) &= \left[\mathbf{He}\left(S_{ia} - X_{ia}\right)\right]^{\mathbf{D}}_{a\in\mathbb{N}_s^+} \\ &\quad + \mathbf{He}\left(\left[S_{ia} + S_{ib}\right]^{\mathbf{U}}_{a,b\in\mathbb{N}_s^+}\right). \end{aligned} \tag{29}$$

Then, S-MJSs (6) with $\prod(h) \in \mathcal{S}_\Pi^{(1)} \cap \mathcal{S}_\Pi^{(2)}$ are stochastically stable.

Proof. From the first constraint $\prod(h) \in \mathcal{S}_\Pi^{(1)}$, we can obtain, under (28),

$$\begin{aligned} 0 &\equiv \mathbf{He}\left(\left(\sum_{j\in\mathbb{N}_s^+}\pi_{ij}(h)\right)\left(G_i + \sum_{j\in\mathbb{N}_s^+}\pi_{ij}(h)S_{ij}\right)\right), \\ &\qquad \forall i \in \mathbb{N}_s^+, \end{aligned} \tag{30}$$

$$0 \leq \sum_{j\in\mathbb{N}_s^+}\mu_{ij}\pi_{ij}\mathbf{He}\left(Y_{ij}\right), \quad \forall i \in \mathbb{N}_s^+. \tag{31}$$

Further, under (27), the second constraint $\prod(h) \in \mathcal{S}_\Pi^{(2)}$ provides

$$\begin{aligned} 0 &\leq -\sum_{j\in\mathbb{N}_s^+}\left(\pi_{ij}(h) - \pi_{ij,1}\right)\left(\pi_{ij}(h) - \pi_{ij,2}\right)\mathbf{He}\left(X_{ij}\right), \\ &\qquad \forall i \in \mathbb{N}_s^+. \end{aligned} \tag{32}$$

Here, note that (30)–(32) can be converted, respectively, into

$$0 \equiv \left[\frac{I}{\prod_i(h)\otimes I}\right]^T \left[\begin{array}{c|c} 0 & [G_i]_{i\in\mathbb{N}_s^+} \\ \hline (*) & (2,2)^* \end{array}\right] \left[\frac{I}{\prod_i(h)\otimes I}\right], \quad (33)$$

$$0 \le \left[\frac{I}{\prod_i(h)\otimes I}\right]^T \left[\begin{array}{c|c} 0 & [\mu_{ij}Y_{ij}]_{j\in\mathbb{N}_s^+} \\ \hline (*) & 0 \end{array}\right] \left[\frac{I}{\prod_i(h)\otimes I}\right], \quad (34)$$

$$0 \le \left[\frac{I}{\prod_i(h)\otimes I}\right]^T \cdot \left[\begin{array}{c|c} (1,1)^* & \left[\left(\pi_{ij,1}+\pi_{ij,2}\right)X_{ij}\right]_{j\in\mathbb{N}_s^+} \\ \hline (*) & [\mathbf{He}(-X_{ia})]^{\mathbf{D}}_{a\in\mathbb{N}_s^+} \end{array}\right] \left[\frac{I}{\prod_i(h)\otimes I}\right], \quad (35)$$

where $(1,1)^* = -\sum_{j\in\mathbb{N}_s^+}\mathbf{He}(\pi_{ij,1}\pi_{ij,2}X_{ij})$ and $(2,2)^* = [\mathbf{He}(S_{ia})]^{\mathbf{D}}_{a\in\mathbb{N}_s^+} + \mathbf{He}([S_{ia}+S_{ib}]^{\mathbf{U}}_{a,b\in\mathbb{N}_s^+})$. Likewise, according to the form of (33)–(35), we can rewrite $\mathcal{Q}_i(h) < 0$ in Lemma 4 as follows:

$$\mathcal{Q}_i(h) = \left[\frac{I}{\prod_i(h)\otimes I}\right]^T \cdot \left[\begin{array}{c|c} \mathbf{He}(P_iA_i) & [(1/2)P_j]_{j\in\mathbb{N}_s^+} \\ \hline (*) & 0 \end{array}\right] \left[\frac{I}{\prod_i(h)\otimes I}\right] < 0. \quad (36)$$

As a result, by combining (36) with (33)–(35) through the S-procedure [34], the stochastic stability condition (25) is given by

$$0 > \left[\frac{I}{\prod_i(h)\otimes I}\right]^T \left[\begin{array}{c|c} (1,1) & (1,2) \\ \hline (*) & (2,2) \end{array}\right] \left[\frac{I}{\prod_i(h)\otimes I}\right], \quad (37)$$

where $(1,1)$, $(1,2)$, and $(2,2)$ are given in the body of Theorem 5. Therefore, as (26) implies (37), the proof can be completed. □

4. Control Design

Let us consider the following mode-dependent state-feedback control law:

$$u(t) = F_i x(t), \quad (38)$$

where $F_i \triangleq F(\zeta(t)=i)$. Thereby, the resultant closed-loop system under (2) and (38) is given by

$$\begin{aligned}\dot{x}(t) &= A_i x(t) + B_i u(t) = (A_i + B_iF_i)x(t) \\ &= \overline{A}_i x(t).\end{aligned} \quad (39)$$

The following theorem provides a relaxed stochastic stabilization condition for S-MJSs (39) with $\prod(h) \in \mathcal{S}_\Pi^{(1)} \cap \mathcal{S}_\Pi^{(2)}$.

Theorem 6. *Suppose that there exist matrices* $\{\overline{F}_i\}_{i\in\mathbb{N}_s^+} \in \mathbb{R}^{n_x\times n_x}$ *and* $\{G_i, S_{ij}, X_{ij}, Y_{ij}, Q_{ij}\}_{i,j\in\mathbb{N}_s^+} \in \mathbb{R}^{n_x\times n_x}$ *and symmetric matrices* $\{\overline{P}_i > 0\}_{i\in\mathbb{N}_s^+} \in \mathbb{R}^{n_x\times n_x}$ *such that*

$$0 > \left[\begin{array}{c|c} (1,1) & (1,2) \\ \hline (*) & (2,2) \end{array}\right], \quad \forall i \in \mathbb{N}_s^+, \quad (40)$$

$$0 \le \mathbf{He}\left(X_{ij}\right), \quad \forall i,j \in \mathbb{N}_s^+, \quad (41)$$

$$0 \le \mathbf{He}\left(Y_{ij}\right), \quad \forall i,j \in \mathbb{N}_s^+, \quad (42)$$

$$0 \le \begin{bmatrix} Q_{ij} & \overline{P}_i \\ (*) & \overline{P}_j \end{bmatrix}, \quad \forall i, j \ne i \in \mathbb{N}_s^+, \quad (43)$$

where $\epsilon_{ij}|_{j\ne i} = 1$, $\epsilon_{ij}|_{j=i} = 0$, $\mu_{ij}|_{j\ne i} = 1$, $\mu_{ij}|_{j=i} = -1$,

$$\begin{aligned}(1,1) &= \mathbf{He}\left(A_i\overline{P}_i + B_i\overline{F}_i\right) - \sum_{j\in\mathbb{N}_s^+}\mathbf{He}\left(\pi_{ij,1}\pi_{ij,2}X_{ij}\right), \\ (1,2) &= \Big[\left(\frac{1}{2}\epsilon_{ij}Q_{ij} + \frac{1}{2}\left(1-\epsilon_{ij}\right)\overline{P}_i\right) + G_i \\ &\quad + \left(\pi_{ij,1}+\pi_{ij,2}\right)X_{ij} + \mu_{ij}Y_{ij}\Big]_{j\in\mathbb{N}_s^+}, \\ (2,2) &= [\mathbf{He}(S_{ia}-X_{ia})]^{\mathbf{D}}_{a\in\mathbb{N}_s^+} + \mathbf{He}\left([S_{ia}+S_{ib}]^{\mathbf{U}}_{a,b\in\mathbb{N}_s^+}\right).\end{aligned} \quad (44)$$

Then, closed-loop system (39) with $\prod(h) \in \mathcal{S}_\Pi^{(1)} \cap \mathcal{S}_\Pi^{(2)}$ *is stochastically stable, where* $F_i = \overline{F}_i\overline{P}_i^{-1}$.

Proof. In light of (25), the stabilization condition of (39) is given by

$$0 > \mathbf{He}\left(P_i\overline{A}_i\right) + \sum_{j=1}^{s}\pi_{ij}(h)P_j. \quad (45)$$

Also, pre- and postmultiplying (45) by $\overline{P}_i \triangleq P_i^{-1}$ yields

$$0 > \overline{\mathcal{Q}}_i(h) \triangleq \mathbf{He}\left(A_i\overline{P}_i + B_i\overline{F}_i\right) + \sum_{j=1}^{s}\pi_{ij}(h)\overline{P}_iP_j\overline{P}_i, \quad (46)$$

where $\overline{F}_i \triangleq F_i\overline{P}_i$. Here, by employing Q_{ij} such that (43) holds (i.e., $Q_{ij} \ge \overline{P}_iP_j\overline{P}_i$), we can convert (46) into

$$\begin{aligned}0 &> \overline{\mathcal{Q}}_i(h) \\ &= \mathbf{He}\left(A_i\overline{P}_i + B_i\overline{F}_i\right) \\ &\quad + \sum_{j=1}^{s}\pi_{ij}(h)\left(\epsilon_{ij}Q_{ij} + \left(1-\epsilon_{ij}\right)\overline{P}_i\right).\end{aligned} \quad (47)$$

Thereupon, $\overline{\mathcal{Q}}_i(h)$ is factorized as follows:

$$\overline{\mathcal{Q}}_i(h) = \left[\frac{I}{\prod_i(h)\otimes I}\right]^T \cdot \left[\begin{array}{c|c} \mathbf{He}\left(A_i\overline{P}_i + B_i\overline{F}_i\right) & (1,2)^* \\ \hline (*) & 0 \end{array}\right] \left[\frac{I}{\prod_i(h)\otimes I}\right], \quad (48)$$

where $(1,2)^* = [(1/2)\epsilon_{ij}Q_{ij} + (1/2)(1-\epsilon_{ij})\overline{P}_i]_{j\in\mathbb{N}_s^+}$.

Next, as in the proof of Theorem 5, the constraint $\prod(h) \in \mathcal{S}_{\Pi}^{(1)} \cap \mathcal{S}_{\Pi}^{(2)}$ can be represented as

$$\begin{aligned} 0 &\equiv \left[\frac{I}{\prod_i(h)\otimes I}\right]^T \left[\begin{array}{c|c} 0 & [G_i]_{i\in\mathbb{N}_s^+} \\ \hline (*) & (2,2)^* \end{array}\right]\left[\frac{I}{\prod_i(h)\otimes I}\right], \\ 0 &\leq \left[\frac{I}{\prod_i(h)\otimes I}\right]^T \left[\begin{array}{c|c} 0 & [\mu_{ij}Y_{ij}]_{j\in\mathbb{N}_s^+} \\ \hline (*) & 0 \end{array}\right]\left[\frac{I}{\prod_i(h)\otimes I}\right], \\ 0 &\leq \left[\frac{I}{\prod_i(h)\otimes I}\right]^T \\ &\cdot \left[\begin{array}{c|c} (1,1)^* & \left[\left(\pi_{ij,1}+\pi_{ij,2}\right)X_{ij}\right]_{j\in\mathbb{N}_s^+} \\ \hline (*) & [\mathbf{He}(-X_{ia})]^{\mathbf{D}}_{a\in\mathbb{N}_s^+} \end{array}\right]\left[\frac{I}{\prod_i(h)\otimes I}\right], \end{aligned} \tag{49}$$

where $(1,1)^* = -\sum_{j\in\mathbb{N}_s^+}\mathbf{He}(\pi_{ij,1}\pi_{ij,2}X_{ij})$ and $(2,2)^* = [\mathbf{He}(S_{ia})]^{\mathbf{D}}_{a\in\mathbb{N}_s^+} + \mathbf{He}([S_{ia}+S_{ib}]^{\mathbf{U}}_{a,b\in\mathbb{N}_s^+})$. As a result, by the S-procedure, combining (48) with (49) results in

$$0 > \left[\frac{I}{\prod_i(h)\otimes I}\right]^T \left[\begin{array}{c|c} (1,1) & (1,2) \\ \hline (*) & (2,2) \end{array}\right]\left[\frac{I}{\prod_i(h)\otimes I}\right], \tag{50}$$

where $(1,1)$, $(1,2)$, and $(2,2)$ are given in the Theorem 6. Therefore, as (40) implies (50), the proof can be completed. □

Hereafter, as a practical extension of the proposed approach, we consider the following input-quantized S-MJSs:

$$\dot{x}(t) = A_i x(t) + B_i\mathbf{q}(u(t)), \tag{51}$$

where $\mathbf{q}(\bullet)$ stands for a uniform quantization operator with the quantization level $\delta > 0$; that is, $\mathbf{q}(u(t)) = \delta\cdot\text{round}(u(t)/\delta)$. Here, note that $\mathbf{q}(u(t)) = u(t)+\varphi(t)$, where the kth element of the quantization error $\varphi(t)$ satisfies

$$|\varphi_k(t)| \leq \frac{\delta}{2}, \quad \forall k\in\mathbb{N}_{n_u}^+. \tag{52}$$

Thus, (51) can be rewritten as

$$\dot{x}(t) = A_i x(t) + B_i(u(t)+\varphi(t)), \tag{53}$$

where $\varphi(t) = \mathbf{q}(u(t)) - u(t)$ is known. Continuously, as a mode-dependent state-feedback law, we adopt

$$u(t) = F_i x(t) + \nu_i(t). \tag{54}$$

Then, the resultant closed-loop system is described as

$$\dot{x}(t) = \overline{A}_i x(t) + B_i(\nu_i(t)+\varphi(t)). \tag{55}$$

The following theorem provides a relaxed stochastic stabilization condition for S-MJSs (55) with input quantization error.

Theorem 7. *Let $\nu_{i,k}$ (i.e., the kth element of ν_i) be given as follows:*

$$\begin{aligned} \nu_{i,k}(t) &= -\delta\cdot\text{sgn}(s_{i,k}(t)) \\ &\quad\cdot\max\left(0,\text{sgn}\left(s_i^T(t)\varphi(t)\right)\right), \\ &\qquad\qquad \forall i\in\mathbb{N}_s^+,\ k\in\mathbb{N}_{n_u}^+, \end{aligned} \tag{56}$$

where $s_i(t) = B_i^T P_i x(t) \in \mathbb{R}^{n_u}$ and $s_{i,k}(t)$ denotes the kth element of $s_i(t)$. Suppose that there exist matrices $\{\overline{F}_i\}_{i\in\mathbb{N}_s^+} \in \mathbb{R}^{n_x\times n_x}$ and $\{G_i, S_{ij}, X_{ij}, Y_{ij}, Q_{ij}\}_{i,j\in\mathbb{N}_s^+} \in \mathbb{R}^{n_x\times n_x}$ and symmetric matrices $\{\overline{P}_i > 0\}_{i\in\mathbb{N}_s^+} \in \mathbb{R}^{n_x\times n_x}$ such that (40)–(43) hold. Then, the closed-loop system (55) with $\prod(h) \in \mathcal{S}_{\Pi}^{(1)} \cap \mathcal{S}_{\Pi}^{(2)}$ is stochastically stable, where $F_i = \overline{F}_i\overline{P}_i^{-1}$.

Proof. From (55), it follows that $x(t+\Delta) = (\overline{A}_i\Delta + I)x(t) + B_i\Delta(\nu_i(t)+\varphi(t))$, for $\Delta\to 0$, which yields

$$\begin{aligned} &x^T(t+\Delta)P_j x(t+\Delta) \\ &\quad = \Delta\cdot x^T(t)\mathbf{He}\left(P_j\overline{A}_i\right)x(t) + x^T(t)P_j x(t) + \Delta \\ &\qquad\cdot 2x^T(t)P_jB_i(\nu_i(t)+\varphi(t)) + \Delta^2\cdot(\bullet). \end{aligned} \tag{57}$$

Thus, it is given that

$$\begin{aligned} &\lim_{\Delta\to 0}\frac{1}{\Delta}p_{ij}(t,\Delta)x^T(t+\Delta)P_jx(t+\Delta) = \lim_{\Delta\to 0}p_{ij}(t,\Delta) \\ &\quad\cdot\left(x^T(t)\mathbf{He}\left(P_j\overline{A}_i\right)x(t)\right. \\ &\quad\left.+2x^T(t)P_jB_i(\nu_i(t)+\varphi(t))\right) + \lim_{\Delta\to 0}\frac{1}{\Delta}p_{ij}(t,\Delta) \\ &\quad\cdot x^T(t)P_jx(t). \end{aligned} \tag{58}$$

Then, based on (11) and (12), we have

$$\Psi_1(t) = \sum_{j=1,\,j\neq i}^{s}\lim_{\Delta\to 0}\frac{1}{\Delta}p_{ij}(t,\Delta)x^T(t)P_jx(t), \tag{59}$$

$$\begin{aligned} &\Psi_2(t)+\Psi_3(t) \\ &\quad = x^T(t)\mathbf{He}\left(P_i\overline{A}_i\right)x(t) \\ &\qquad + 2x^T(t)P_iB_i(\nu_i(t)+\varphi(t)) \\ &\qquad + \lim_{\Delta\to 0}\frac{1}{\Delta}(p_{ii}(t,\Delta)-1)x^T(t)P_ix(t), \end{aligned} \tag{60}$$

which leads to

$$\begin{aligned} \nabla V(t) &= x^T(t)\left(\mathbf{He}\left(P_i\overline{A}_i\right)+\sum_{j=1}^{s}\pi_{ij}(h)P_j\right)x(t) \\ &\quad + 2s_i^T(t)(\nu_i(t)+\varphi(t)), \\ s_i(t) &= B_i^TP_ix(t)\in\mathbb{R}^{n_u}. \end{aligned} \tag{61}$$

Hence, for $s_i^T(t)\varphi(t)\leq 0$, letting $\nu_i(t)\equiv 0$ implies

$$\nabla V(t) \leq x^T(t)\left(\mathbf{He}\left(P_i\overline{A}_i\right)+\sum_{j=1}^{s}\pi_{ij}(h)P_j\right)x(t). \tag{62}$$

Further, for $s_i^T(t)\varphi(t) > 0$, letting $\nu_{i,k}(t) = -\delta \cdot \mathrm{sgn}(s_{i,k}(t))$ yields

$$\begin{aligned} 2s_i^T(t)(\nu_i(t)+\varphi(t)) &= \sum_{k=1}^{n_u} 2s_{i,k}(t)(\nu_{i,k}(t)+\varphi_k(t)) \\ &\le \sum_{k=1}^{n_u} -2\delta|s_{i,k}(t)| + 2|s_{i,k}(t)| \\ &\quad \cdot |\varphi_k(t)| \le -\sum_{k=1}^{n_u}\delta|s_{i,k}(t)| < 0. \end{aligned} \tag{63}$$

That is, (56) allows (61) to be reduced to (62) for all $s_i^T(t)\varphi(t)$. In what follows, we need to derive the stabilization condition from (62), which is omitted herein because it is in line with the proof of Theorem 6. □

5. Numerical Examples

Example 1. Consider the following system with three different modes: for $x_0 = (3.0, -5.0)$ and $\zeta_0 = 3$,

$$\begin{aligned} A_1 &= \begin{bmatrix} -0.5 & -0.75 \\ 1.00 & 1.00 \end{bmatrix}, \\ A_2 &= \begin{bmatrix} -2.40 & -0.33 \\ 1.00 & -1.40 \end{bmatrix}, \\ A_3 &= \begin{bmatrix} -0.20 & 0.10 \\ 1.00 & -1.00 \end{bmatrix}, \\ B_1 &= \begin{bmatrix} 5.0 \\ 0.0 \end{bmatrix}, \\ B_2 &= \begin{bmatrix} -2.0 \\ -1.0 \end{bmatrix}, \\ B_3 &= \begin{bmatrix} 1.0 \\ -2.0 \end{bmatrix}. \end{aligned} \tag{64}$$

Here, the Weibull distribution for the sojourn-time is set by $(\alpha_1, \beta_1) = (0.5, 2.0)$, $(\alpha_2, \beta_2) = (1.0, 2.0)$, and $(\alpha_3, \beta_3) = (1.5, 2.0)$ (see Figure 1). Thereby, a reasonable interval $h \in [h_0, h_1]$ can be obtained such that $\int_{h_0}^{h_1} g_i(h)dh \ge 0.99$, from which the lower and upper bounds $(\pi_{i,1}, \pi_{i,2})$ of $\pi_i(h)$ can be also found. As a result, by considering the uncertain probability intensities such that $0.3 \le q_{ij} \le 0.7$, for all i and j, the following matrices such that $\pi_{ij}(h) \in [\pi_{ij,1}, \pi_{ij,2}]$ are established from Remark 3:

$$\begin{aligned} [\pi_{ij,1}]_{i,j\in\mathbb{N}_3^+} &= \begin{bmatrix} -8.6880 & 0.0384 & 0.0896 \\ 0.0192 & -4.3420 & 0.0448 \\ 0.0128 & 0.0299 & -2.8951 \end{bmatrix}, \\ [\pi_{ij,2}]_{i,j\in\mathbb{N}_3^+} &= \begin{bmatrix} -0.1280 & 2.6064 & 6.0816 \\ 1.3026 & -0.0640 & 3.0394 \\ 0.8685 & 2.0266 & -0.0427 \end{bmatrix}. \end{aligned} \tag{65}$$

Figure 2(a) shows the mode evolution generated from the stochastic setting. Besides, from Theorem 6, the following control gains are obtained:

$$\begin{aligned} F_1 &= [0.2654 \quad -0.0063], \\ F_2 &= [-0.7178 \quad -0.1854], \\ F_3 &= [-1.9513 \quad 0.6293]. \end{aligned} \tag{66}$$

Figure 2(b) shows the behavior of the state response coupled with the mode transition depicted in Figures 2(a) and 2(c) which presents the Monte Carlo simulation result of the settling time for 5000 different mode transition configurations, where its mean value and standard deviation are 12.2979 and 3.126, respectively. From Figure 2(b), it can be seen that the states converge from the initial condition $(3.0, -5.0)$ to the equilibrium point as time increases. Consequently, Theorem 6 provides an applicable method for deriving a relaxed stabilization condition for S-MJSs with uncertain probability intensities.

Example 2. Consider the following system representing an inverted pendulum: for $x_0 = (1, -1, 0.5)$ and $\zeta_0 = 3$:

$$\begin{aligned} \dot{x}_1(t) &= x_2(t), \\ \dot{x}_2(t) &= \frac{g}{l}\sin x_1(t) + \frac{Nk_m}{ml^2}x_3(t), \\ L_a\dot{x}_3(t) &= k_bNx_2(t) - R(\zeta(t))x_3(t) + \mathbf{q}(u(t)), \end{aligned} \tag{67}$$

where $x_1(t)$ is the angle of the inverted pendulum, $x_2(t)$ is the angular velocity, $x_3(t)$ is the input current, $u(t)$ is the control input voltage, g is the acceleration due to gravity, m and l are the mass and length, respectively, k_b and k_m are the back emf constant and motor torque constant, respectively, L_a and $R(\zeta(t))$ are the inductance and resistance of the DC motor, respectively, and N is the gear ratio. Here, we set $L_a = 1$, $g = 9.8$, $l = 1$, $m = 1$, $N = 10$, $K_m = K_b = 0.1$, and

$$R_i = R(\zeta(t) = i) = \begin{cases} 2, & \text{for } \zeta(t) = 1 \\ 1, & \text{for } \zeta(t) = 2 \\ 0.5, & \text{for } \zeta(t) = 3. \end{cases} \tag{68}$$

Then, the linearized model of (67) is given by

$$\begin{aligned} A_i &= A(\zeta(t) = i) \begin{bmatrix} 0 & 1 & 0 \\ 9.8 & 0 & 1 \\ 0 & 1 & -R_i \end{bmatrix}, \\ B_1 &= B_2 = B_3 = \begin{bmatrix} 0 \\ 0 \\ 1 \end{bmatrix}, \end{aligned} \tag{69}$$

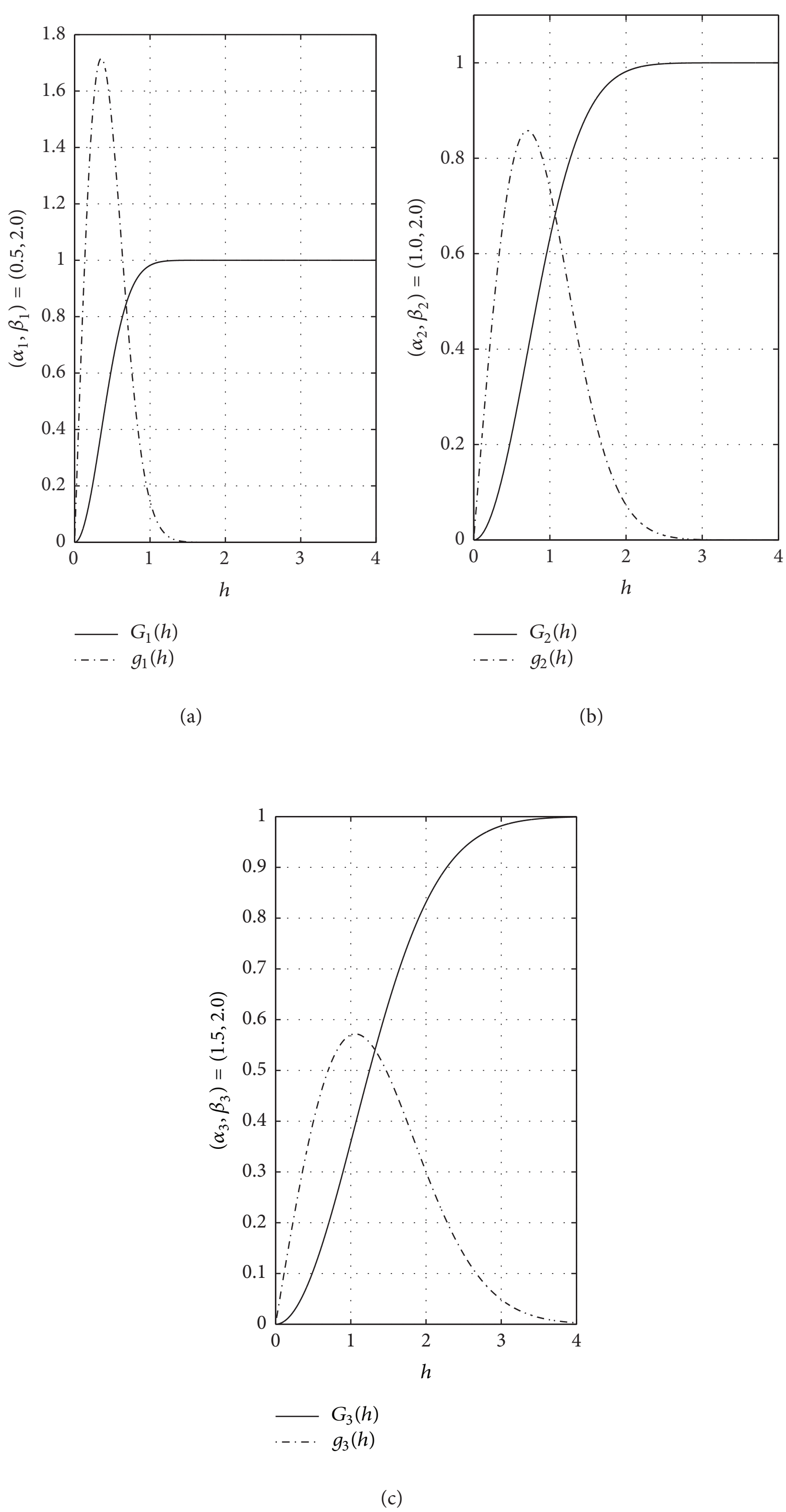

FIGURE 1: Cumulative distribution functions $G_i(h)$ (solid line) and probability distribution functions $g_i(h)$ (dash-dotted line).

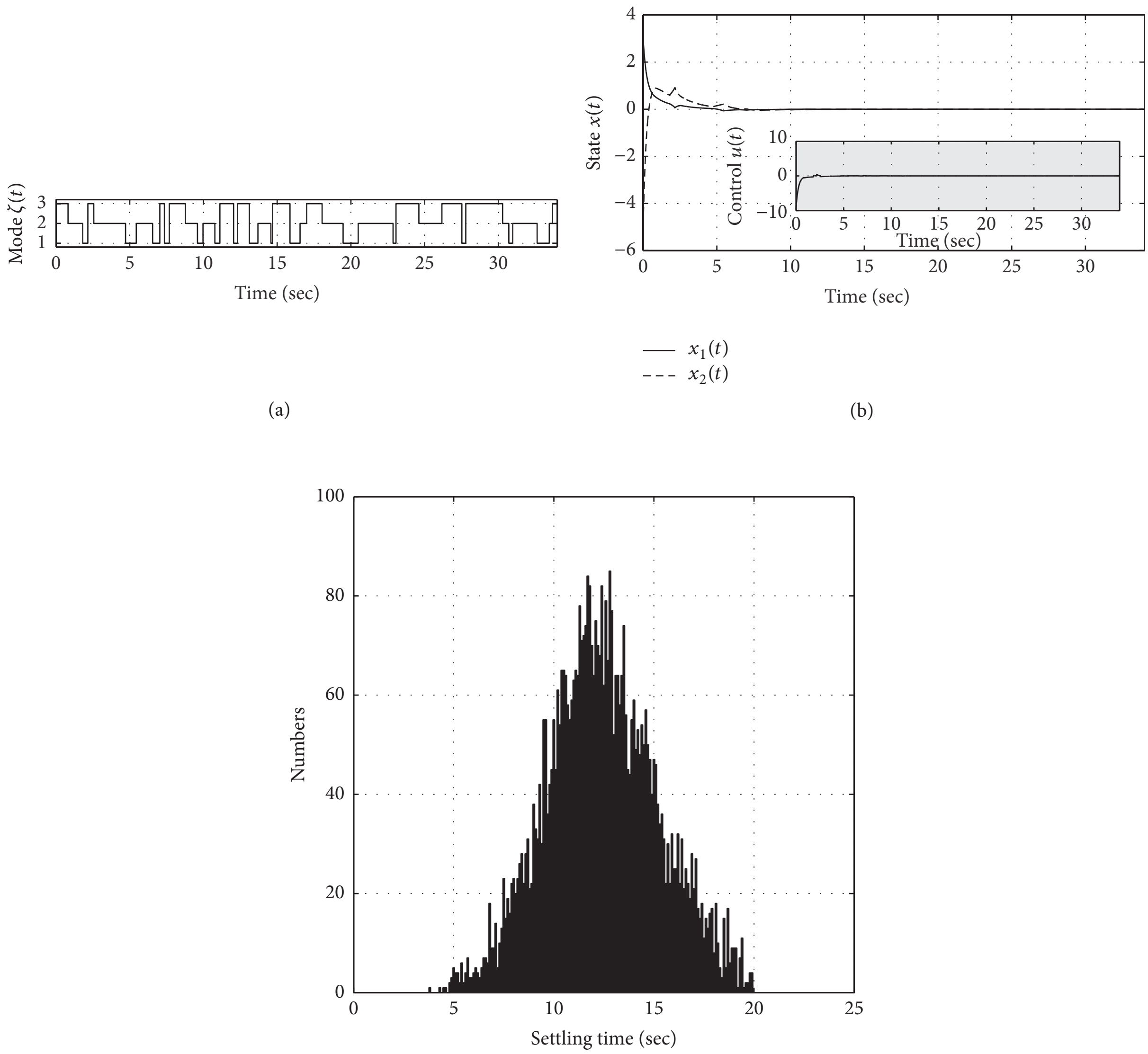

(c)

Figure 2: (a) Mode evolution, (b) state response and control input, and (c) Monte Carlo simulation results.

Besides, the matrices $[\pi_{ij,1}]_{ij\in\mathbb{N}_3^+}$ and $[\pi_{ij,2}]_{ij\in\mathbb{N}_3^+}$ such that $\pi_{ij}(h) \in [\pi_{ij,1}, \pi_{ij,2}]$ are taken to be the same as in Example 1. Thereupon, Theorem 7 provides the following control gains:

$$\begin{aligned} F_1 &= \left[-2.7348 \quad -3.1067 \quad 2.1744\right], \\ F_2 &= \left[-4.7643 \quad -3.6490 \quad 0.5326\right], \\ F_3 &= \left[-243.8434 \quad -79.7086 \quad -12.9784\right]. \end{aligned} \tag{70}$$

Figure 3 shows the behavior of the state response for the mode transition generated according to $(\alpha_1, \beta_1) = (0.5, 2.0)$, $(\alpha_2, \beta_2) = (1.0, 2.0)$, and $(\alpha_3, \beta_3) = (1.5, 2.0)$. Here, the control input $\nu_i(t)$ is designed in accordance with (56), and the quantization level is assumed to be $\delta = 0.1$. From Figure 3, it can be seen that the states converge from the initial-state condition $(1, -1, 0.5)$ to the origin as time increases. Consequently, Theorem 7 provides a suitable mode-dependent control for the S-MJSs with input quantization errors as well as uncertain probability intensities.

6. Concluding Remarks

The issue of stability analysis and control synthesis for S-MJSs with uncertain probability intensities has been addressed in this paper. Here, the boundary constraints of probability intensities have been totally reflected in the stabilization condition via a relaxation process established on the basis of time-varying transition rates. Furthermore, as an extension, the quantized control problem of S-MJSs has been addressed

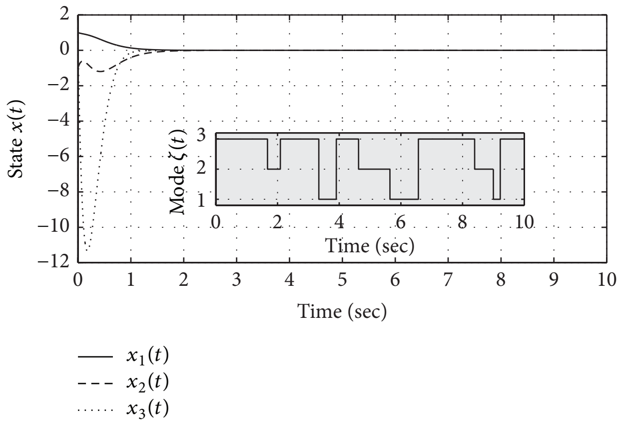

FIGURE 3: State response and mode evolution.

herein. Through simulation examples, the effectiveness of the proposed method has been shown.

Competing Interests

The authors declare that there is no conflict of interests regarding the publication of this paper.

Acknowledgments

This work was supported by the National Research Foundation of Korea Grant funded by the Korean Government (NRF-2015R1A1A1A05001131).

References

[1] E. K. Boukas, "Manufacturing systems: LMI approach," *IEEE Transactions on Automatic Control*, vol. 51, no. 6, pp. 1014–1018, 2006.

[2] F. Martinelli, "Optimality of a two-threshold feedback control for a manufacturing system with a production dependent failure rate," *IEEE Transactions on Automatic Control*, vol. 52, no. 10, pp. 1937–1942, 2007.

[3] H. Joo and S. H. Kim, "$\mathscr{H}_\infty$ LPV control with pole placement constraints for synchronous buck converters with piecewise-constant loads," *Mathematical Problems in Engineering*, vol. 2015, Article ID 686857, 8 pages, 2015.

[4] P. Seiler and R. Sengupta, "An H_∞ approach to networked control," *IEEE Transactions on Automatic Control*, vol. 50, no. 3, pp. 356–364, 2005.

[5] Y. Shi and B. Yu, "Output feedback stabilization of networked control systems with random delays modeled by Markov chains," *IEEE Transactions on Automatic Control*, vol. 54, no. 7, pp. 1668–1674, 2009.

[6] J. Wu and T. Chen, "Design of networked control systems with packet dropouts," *IEEE Transactions on Automatic Control*, vol. 52, no. 7, pp. 1314–1319, 2007.

[7] L. Zhang, Y. Shi, T. Chen, and B. Huang, "A new method for stabilization of networked control systems with random delays," *IEEE Transactions on Automatic Control*, vol. 50, no. 8, pp. 1177–1181, 2005.

[8] S. W. Yun and S. H. Kim, "Efficient approach to stability analysis of discrete-time systems with time-varying delay," *Mathematical Problems in Engineering*, vol. 2015, Article ID 813123, 9 pages, 2015.

[9] L. Li, V. A. Ugrinovskii, and R. Orsi, "Decentralized robust control of uncertain Markov jump parameter systems via output feedback," *Automatica*, vol. 43, no. 11, pp. 1932–1944, 2007.

[10] I. Matei and J. S. Baras, "A linear distributed filter inspired by the Markovian jump linear system filtering problem," *Automatica*, vol. 48, no. 8, pp. 1924–1928, 2012.

[11] J. Dong and G.-H. Yang, "Robust H_2 control of continuous-time Markov jump linear systems," *Automatica*, vol. 44, no. 5, pp. 1431–1436, 2008.

[12] H. Zhao, Q. Chen, and S. Xu, "H_∞ guaranteed cost control for uncertain Markovian jump systems with mode-dependent distributed delays and input delays," *Journal of the Franklin Institute-Engineering and Applied Mathematics*, vol. 346, pp. 945–957, 2009.

[13] H. Li, Q. Zhou, B. Chen, and H. Liu, "Parameter-dependent robust stability for uncertain Markovian jump systems with time delay," *Journal of the Franklin Institute-Engineering and Applied Mathematics*, vol. 348, no. 4, pp. 738–748, 2011.

[14] E. K. Boukas, "H_∞ control of discrete-time Markov jump systems with bounded transition probabilities," *Optimal Control Applications & Methods*, vol. 30, no. 5, pp. 477–494, 2009.

[15] M. Shen and G.-H. Yang, "H_2 state feedback controller design for continuous Markov jump linear systems with partly known information," *International Journal of Systems Science*, vol. 43, no. 4, pp. 786–796, 2012.

[16] J. Xiong and J. Lam, "Robust H_2 control of Markovian jump systems with uncertain switching probabilities," *International Journal of Systems Science*, vol. 40, no. 3, pp. 255–265, 2009.

[17] L. Zhang and E.-K. Boukas, "Stability and stabilization of Markovian jump linear systems with partly unknown transition probabilities," *Automatica*, vol. 45, no. 2, pp. 463–468, 2009.

[18] S. H. Kim, "Less conservative stabilization conditions for Markovian jump systems with partly unknown transition probabilities," *Journal of the Franklin Institute. Engineering and Applied Mathematics*, vol. 351, no. 5, pp. 3042–3052, 2014.

[19] S. H. Kim, "Control synthesis of Markovian jump fuzzy systems based on a relaxation scheme for incomplete transition probability descriptions," *Nonlinear Dynamics*, vol. 78, no. 1, pp. 691–701, 2014.

[20] S. H. kim, "Delay-dependent stability analysis for singular Markovian jump systems with incomplete transition probabilities," *Journal of the Franklin Institute-Engineering and Applied Mathematics*, vol. 352, no. 1, pp. 236–247, 2015.

[21] Z. Hou, J. Luo, and P. Shi, "Stochastic stability of linear systems with semi-Markovian jump parameters," *The ANZIAM Journal*, vol. 46, no. 3, pp. 331–340, 2005.

[22] Z. Hou, J. Luo, P. Shi, and S. K. Nguang, "Stochastic stability of Ito differential equations with semi-Markovian jump parameters," *IEEE Transactions on Automatic Control*, vol. 51, no. 8, pp. 1383–1387, 2006.

[23] L. Zhang, "H_∞ control of a class of piecewise homogeneous Markov jump linear systems," in *Proceedings of the 7th Asian Control Conference (ASCC '09)*, pp. 197–202, Hong Kong, August 2009.

[24] C. Schwartz, *Control of semi-Markov jump linear systems with application to the bunch-train cavity interaction [Ph.D. thesis]*, Northwestern University, 2003.

[25] J. Huang and Y. Shi, "Stochastic stability of semi-Markov jump linear systems: an LMI approach," in *Proceedings of the 50th IEEE Conference on Decision and Control and European Control Conference (CDC-ECC '11)*, pp. 4668–4673, Orlando, Fla, USA, December 2011.

[26] X. Liu, X. Yu, G. Ma, and H. Xi, "On sliding mode control for networked control systems with semi-Markovian switching and random sensor delays," *Information Sciences*, vol. 337-338, pp. 44–58, 2016.

[27] J. Huang and Y. Shi, "Stochastic stability and robust stabilization of semi-Markov jump linear systems," *International Journal of Robust and Nonlinear Control*, vol. 23, no. 18, pp. 2028–2043, 2013.

[28] J. Huang and Y. Shi, "H_∞ stability-feedback control for semi-Markovian jump linear systems with time-varying delays," *Journal of Dynamic Systems, Measurement, and Control*, vol. 135, no. 4, Article ID 041012, 2013.

[29] F. Li, L. Wu, P. Shi, and C.-C. Lim, "State estimation and sliding mode control for semi-Markovian jump systems with mismatched uncertainties," *Automatica*, vol. 51, pp. 385–393, 2015.

[30] H. Shen, Z.-G. Wu, and J. H. Park, "Reliable mixed passive and H_∞ filtering for semi-Markov jump systems with randomly occurring uncertainties and sensor failures," *International Journal of Robust and Nonlinear Control*, vol. 25, no. 17, pp. 3231–3251, 2015.

[31] S. H. Kim, "Multi-stage control strategy for quantised feedback control systems," *IET Control Theory & Applications*, vol. 7, no. 4, pp. 584–593, 2013.

[32] S. W. Yun, S. H. Kim, and J. Y. Park, "Asymptotic stabilization of continuous-time linear systems with input and state quantizations," *Mathematical Problems in Engineering*, vol. 2014, Article ID 947164, 6 pages, 2014.

[33] A. Svishchuk, *Random Evolutions and Their Applications: New Trends*, Kluwer Academic, Norwell, Mass, USA, 2000.

[34] S. Boyd, L. E. Chauoi, E. Feron, and V. Balakrishan, *Linear Matrix Inequalities in Systems and Control Theory*, SIAM, Philadelphia, Pa, USA, 1994.

Hindawi Publishing Corporation
Mathematical Problems in Engineering
Volume 2016, Article ID 3542898, 9 pages
http://dx.doi.org/10.1155/2016/3542898

Research Article

A New Approach for Chaotic Time Series Prediction Using Recurrent Neural Network

Qinghai Li and Rui-Chang Lin

Department of Electronic Engineering, Zhejiang Industry and Trade Vocational College, East Road 717, Wenzhou 325003, China

Correspondence should be addressed to Rui-Chang Lin; rc921.lin@qq.com

Received 4 July 2016; Accepted 31 October 2016

Academic Editor: Lijun Zhu

A self-constructing fuzzy neural network (SCFNN) has been successfully used for chaotic time series prediction in the literature. In this paper, we propose the strategy of adding a recurrent path in each node of the hidden layer of SCFNN, resulting in a self-constructing recurrent fuzzy neural network (SCRFNN). This novel network does not increase complexity in fuzzy inference or learning process. Specifically, the structure learning is based on partition of the input space, and the parameter learning is based on the supervised gradient descent method using a delta adaptation law. This novel network can also be applied for chaotic time series prediction including Logistic and Henon time series. More significantly, it features rapider convergence and higher prediction accuracy.

1. Introduction

A chaotic time series can be expressed as a deterministic dynamical system that however is usually unknown or incompletely understood. Therefore, it becomes important to make prediction from the experimental observation of a real system. The technology was widely studied in many science and engineering fields such as mathematical finance, weather forecasting, and intelligent transport and trajectory forecasting. The early research on nonlinear prediction of chaotic time series can be found in [1]. Most recent work mainly focuses on different methods for improving the prediction performance, such as fuzzy neural networks [2, 3], RBF [4, 5], recurrent neural networks [6, 7], back-propagation recurrent neural networks [8], predictive consensus networks [9, 10], and biologically inspired neuronal network [11, 12].

Both fuzzy logic and artificial neural networks are potentially suitable for nonlinear chaotic series prediction as they can perform complex mappings between their input and output spaces. In particular, the self-constructing fuzzy neural network (SCFNN) [13] is capable of constructing a simple network without the need of knowledge to the chaotic series. This capability is due to SCFNN's ability of self-adjusting the location of the input space fuzzy partition, so there is no need to estimate in advance the series states distribution. Moreover, carefully setting conditions on the increasing demand of fuzzy rules makes the architecture of the constructed SCFNN fairly simple. These advantages motivated researchers to build various chaotic series prediction algorithms by employing an SCFNN structure in, for example, [14, 15].

Neural network has wide applications in various areas; see, for example, [16–21]. In particular, recurrent neural network (RNN) has been proved successful in speech processing and adaptive channel equalization. One of the most important features of RNN is its feedback paths in the circuit that makes it have a sequential rather than a combinational behavior. RNNs were applied not only in the processing of time-varying patterns or data sequences but also in dealing with the dissonance of input pattern when the possibly different outputs are generated by the same set of input patterns due to the feedback paths. Since RNN is a highly nonlinear dynamical system that exhibits rich and complex behaviors, it is expected that RNN possesses better performance than traditional signal processing techniques in modeling and predicting chaotic time series. Some works on improving the performance of chaotic series prediction using RNNs can be found in, for example, [6, 7].

From the above observation, it is a novel idea to combine the SCFNN and RNN techniques for chaotic series prediction, which results in a new architecture called self-constructing recurrent fuzzy neural network (SCRFNN) in this paper. The structure learning and parameter learning algorithms in SCRFNN are inherited from those in SCFNN, which maintains the simplicity in implementation. Nevertheless, the recurrent path in SCRFNN makes it more complex in function deviation and exhibit richer behaviors. Extensive numerical simulation shows that both SCFNN and SCRFNN are effective in predicting chaotic time series including Logistic series and Henon series. But the latter has superior performance in convergence rate and prediction accuracy at the cost of slightly heavier structure (number of hidden nodes) and fuzzy logic rules.

It is noted that a similar neural network structure has been used for nonlinear channel equalizers in [20]. The purpose of an equalizer in, for example, wireless communication systems, is to recover the transmitted sequence or its delayed version using a trained neural network. But the chaotic time series prediction studied in this paper has a completely different mechanism. Chaotic time series prediction is the problem of developing a dynamic model by the observed time series for a nonlinear chaotic system that exhibits deterministic behavior with a known initial condition. A neural network is used to build chaotic time series predication after the so-called phase space reconstruction that is not touched in channel equalizers.

The rest of this paper is organized as follows. In Section 2, the problem of chaotic series prediction is formulated. The structure, the inference output, and the learning algorithms of SCRFNN are described in Section 3. Numerical simulation results on two classes of Logistic and Henon chaotic series predictions are presented in Section 4. Finally, the paper is concluded in Section 5.

2. Background and Preliminaries

The phase space reconstruction theory is commonly used for chaotic time series prediction; see, for example, [22, 23]. The main idea is to find a way for phase space reconstruction from time series and then conduct prediction in phase space. The theory is briefly revisited in this section followed by a general neural network prediction model.

Delay embedding is the main technique for phase space reconstruction. Assume a chaotic time series is represented as $x_1, x_2, \ldots, x_n$ and the phase space vector

$$X_i = \left(x_i, x_{i+\tau}, \ldots, x_{i+(m-1)\tau}\right)^T, \quad i = 1, 2, \ldots, M. \tag{1}$$

The parameter τ is the delay, m the embedding dimension, and $M = n - (m-1)\tau$ the number of phase vectors. A prediction model contains an attractor that warps the observed data, in the phase space, and provides precise information about the dynamics involved. Therefore, it can be used to predict X_{i+1} from X_i in phase space and hence synthesize x_{i+1} using time series reconstruction. The procedure can be summarized as a model with input X_i and output x_{i+1}.

Takens' theorem provides the conditions under which a smooth attractor can be reconstructed from the observations made with a generic function. The theorem states that, if the embedding dimension $m \geq 2d + 1$, where d is the dimension of the system dynamics, then the phase space constituted by the original system state variable and the dynamic behaviors in the one-dimensional sequence of observations are equivalent. It is equivalent because the chaotic attractor differential in the two spaces is homeomorphism. The reconstructed system that includes the evolution information of all state variables is capable of calculating the future state of the system based on its current state, which provides a basic mechanism for chaotic time series prediction.

As explained before, the prediction model with input X_i and output x_{i+1} provides precise information of the nonlinear dynamics under consideration. Neural network (NN) is an appropriate structure to build a nonlinear model of chaotic time series predication. Specifically, a typical three-layer NN is discussed below.

When we apply a three-layer NN to predict a chaotic time series, better prediction performance can be achieved if the number of neurons of the input layer is equal to the embedding dimension of the phase space reconstructed by the chaotic time series. Specifically, let the number of neurons of the input layer be m, that of the hidden layer be p, and that of output layer be 1. Then, the NN describes a mapping $f : \mathbb{R}^m \to \mathbb{R}^1$.

The input for the nodes of the hidden layer is

$$S_j = \sum_{i=1}^{m} \omega_{ij} x_i - \theta_j, \quad j = 1, 2, \ldots, p, \tag{2}$$

where ω_{ij} is the link weight from the input layer to the hidden layer and θ_j is the threshold. Assume the Sigmoid transfer function $f(s) = 1/(1+e^{-s})$ is used for the NN. Then the output of the hidden layer nodes is

$$b_j = \frac{1}{1 + \exp\left(-\sum_{i=1}^{m} \omega_{ij} x_i + \theta_j\right)}, \quad j = 1, 2, \ldots, p. \tag{3}$$

Similarly, the input and the output of the output layer nodes are

$$\begin{aligned} L &= \sum_{j=1}^{p} V_j b_j - \gamma, \\ x_{i+1} &= \frac{1}{1 + \exp\left(-\sum_{j=1}^{p} V_j b_j + \gamma\right)}, \end{aligned} \tag{4}$$

respectively. Here V_j is the link weight from the hidden layer to the output layer and γ is the threshold.

In general, the aforementioned link weights (ω_{ij}, V_j) and the thresholds (θ_j, γ) of the NN can be randomly initialized, for example, within $[0, 1]$. Then, they can be properly trained such that the resulting NN has the capability of precise prediction. The specific training strategy depends on the specific architecture of the NN, which is the main scope of this research line and will be elaborated in the next section.

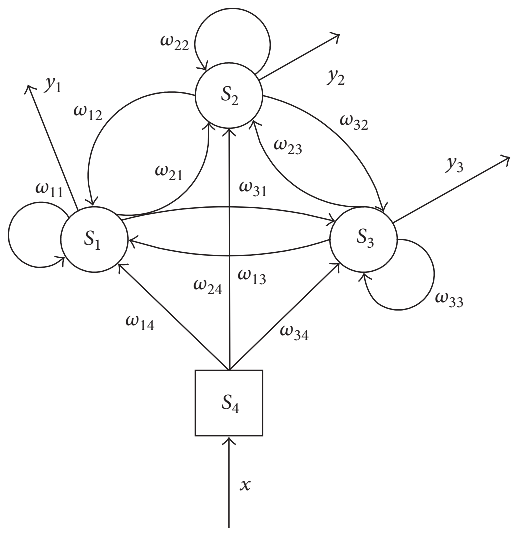

Figure 1: Structure of a recurrent neural network.

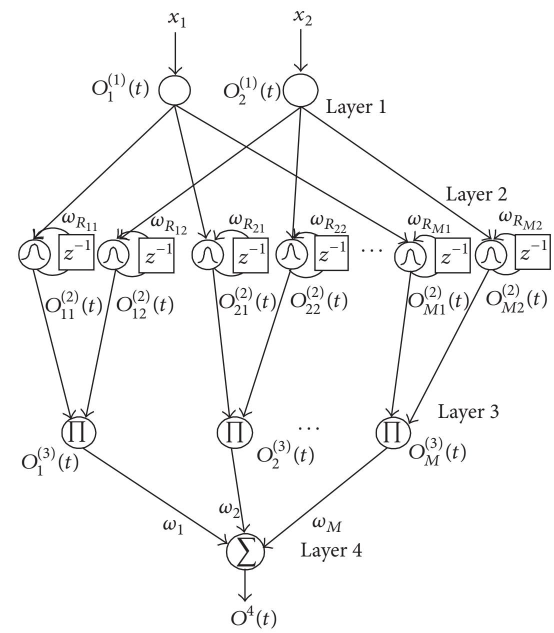

Figure 2: Schematic diagram of SCRFNN.

3. Self-Constructing Recurrent Fuzzy Neural Network

Following the general description of the NN prediction model introduced in the previous section, we aim to propose a specific architecture with the features of fuzzy logic, recurrent path, and self-constructing ability, called a self-constructing recurrent fuzzy neural network (SCRFNN). With these features, the SCRFNN is able to exhibit rapid convergence and high prediction accuracy.

3.1. Background of SCRFNN. The network structure of a traditional fuzzy neural network (FNN) is determined in advance. During the learning process, the structure is fixed and a supervised back-propagation algorithm is applied to adjust the membership function parameters and the weighting coefficients. Such an FNN with a fixed structure usually needs a large number of hidden layer nodes for acceptable performance, which significantly increases the system complexity [24, 25].

To overcome the aforementioned drawback of a fixed structure, the SCRFNN used in this paper exploits a two-phase learning algorithm that includes both structure learning and parameter learning. Specifically, the structure of fuzzy rules is determined in the first phase and the coefficients of each rule are tuned in the second one. It is conceptually easy to sequentially carry out the two phases. However, it is suitable only for offline operations with a large amount of representative data collected in advance [26]. Moreover, independent realization of structure and parameter learning is time-consuming. These disadvantages can be eliminated in SCRFNN as the two phases of structure learning and parameter learning are conducted concurrently [27].

The main feature of the proposed SCRFNN is the novel recurrent path in the circuit. The schematic diagram of a recurrent neural network (RNN) is shown in Figure 1 [28], where, for example, x and y_k, $k = 1, 2, 3$, denote the external input and the unit outputs, respectively. The dynamics of such a structure can be described by, for $k = 1, 2, 3$,

$$\begin{aligned} s_k[t+1] &= \sum_{l=1}^{n} \omega_{kl}[t]\, y_l[t] + \sum_{l=1}^{m} \omega_{k,l+n}[t]\, x_l^{\text{net}}[t], \\ y_k[t+1] &= f\left(s_k[t+1]\right), \end{aligned} \tag{5}$$

where m and n denote the numbers of external inputs and hidden layer units, respectively, $\omega_{ij}[t]$ is the connection weight from the jth unit to the ith unit at the time instant t, and the activation function $f(\cdot)$ can be any real differentiable function. Clearly, the output of each unit depends on the previous external inputs to the network as well as the previous outputs of all units. The training algorithms for the recurrent parameters of RNNs have been well studied, for example, the real-time recurrent learning (RTRL) algorithm [29].

3.2. Structure and Inference Output of SCRFNN. The schematic diagram of SCRFNN is shown in Figure 2. The fuzzy logic rule and the functions in each layer are briefly described as follows.

The fuzzy logic rule adopted in the SCRFNN has the following form:

$$\begin{aligned} R_j:\quad & \text{If } \left(x_1 + \omega_{R_{j1}} O_{j1}^{(2)}(t-1)\right) \text{ is } A_{j1}, \\ & \text{and } \left(x_2 + \omega_{R_{j2}} O_{j2}^{(2)}(t-1)\right) \text{ is } A_{j2}, \ldots, \\ & \text{and } \left(x_n + \omega_{R_{jn}} O_{jn}^{(2)}(t-1)\right) \text{ is } A_{jn}. \\ & \text{Then } y(t) = \omega_j \end{aligned} \tag{6}$$

with n input variables and a constant consequence ω_j. In (6), A_{ji} is the linguistic term of the precondition part with membership function $\mu_{A_{ji}}$, x_i's and y denote the input and output variables, respectively, and $\omega_{R_{ji}}$ and $O_{ji}^{(2)}(t-1)$ represent the recurrent coefficient and the last state output of the jth term associated with the ith input variable.

The nodes in Layer 1, called the input nodes, simply pass the input signals to the next layer. There are two input variables x_1 and x_2 and two corresponding outputs $O_1^{(1)}(t) = x_1$ and $O_2^{(1)}(t) = x_2$ for the problem considered in this paper.

Each node in Layer 2 acts as a linguistic label for the input variables from Layer 1. Let $O_{ji}^{(2)}(t)$ be the output of the jth rule associated with the ith input node in status t and $\omega_{R_{ji}}$'s the recurrent coefficients. Then, the Gaussian membership function is determined in this layer as follows:

$$O_{ji}^{(2)}(t) = \exp\left(-\frac{\left(O_i^{(1)}(t) + \omega_{R_{ji}} O_{ji}^{(2)}(t-1) - m_{ji}\right)^2}{\sigma_{ji}^2}\right) \tag{7}$$

with the mean m_{ji} and the standard deviation σ_{ji}.

Each node in Layer 3, represented by the product symbol Π, works as the precondition part of the fuzzy logic rule. Specifically, the output of the jth rule node in status t is thus expressed as

$$O_j^{(3)}(t) = \prod_i O_{ji}^{(2)}(t). \tag{8}$$

The single node in Layer 4, called the output node, acts as a defuzzifier. As a result, the final output of the SCRFNN is

$$O^{(4)}(t) = \sum_j \omega_j O_j^{(3)}(t), \tag{9}$$

where the link weight ω_j is the output action strength associated with the jth rule.

3.3. Online Learning Algorithm for SCRFNN. As discussed in Section 3.1, a two-phase learning algorithm for structure learning and parameter learning is used for SCRFNN. The initial SCRFNN is composed of the input and output nodes only. The membership and the rule nodes are dynamically generated and adjusted according to the online data by performing the structure and parameter learning processes. These two phases are explained below.

The structure learning algorithm aims to find the proper input space fuzzy partitions and fuzzy logic rules with minimal fuzzy sets and rules. As the initial SCRFNN contains no membership or rule node, the main work in structure learning is to decide whether it is necessary to add a new membership function node in Layer 2 and the associated fuzzy logic rule in Layer 3. The criterion for generating a new fuzzy rule for new incoming data is based on the firing strengths $O_j^{(3)}(t) = \prod_i O_{ji}^{(2)}(t)$, $j = 1, \ldots, M$, where M is the number of existing rules.

Specifically, if the maximum degree $\mu_{\max} = \max_{1\le j\le M} O_j^{(3)}(t)$ is not larger than a prespecified threshold parameter $\mu_{\min}$, a new membership function needs to be generated. Also, the mean value and the standard deviation of the new membership function are, respectively, assigned as $m_i^{\text{new}} = x_i$ and $\sigma_i^{\text{new}} = \sigma_i$, where x_i is the new incoming data and σ_i is an empirical prespecified constant. The value $\mu_{\min}$ is initially chosen between 0 and 1 and then keeps decaying in order to limit the growing size of the SCRFNN structure.

The parameter learning algorithm aims to minimize a predefined energy function by adaptively adjusting the vector of network parameters based on a given set of input-output pairs. The particular energy function used in the SCRFNN is as follows:

$$E = \frac{1}{2}\left(O^d - O^{(4)}(t)\right)^2, \tag{10}$$

where O^d is the desired output associated with the input pattern and $O^{(4)}(t)$ is the inferred output. The vector is adjusted along the negative gradient of the energy function with respect to the vector. In the four-layer SCRFNN, a back-propagation learning rule is adopted as the gradient vector is calculated in the direction opposite to the data flow, as described below.

First, the link weight ω_j for the output node in Layer 4 is updated along the negative gradient of the energy function; that is,

$$\Delta\omega_j = \frac{\partial E}{\partial \omega_j} = -\left(O^d - O^{(4)}(t)\right) O_j^{(3)}(t). \tag{11}$$

In particular, it is updated according to

$$\omega_j(k+1) = \omega_j(k) - \eta_\omega \Delta\omega_j, \tag{12}$$

where k is the pattern number of the jth link and the factor η_ω is the learning-rate parameter.

Next, in Layer 3, the mean m_{ji} and the standard deviation σ_{ji} of the membership functions are updated by

$$\begin{aligned} m_{ji}(k+1) &= m_{ji}(k) - \eta_m \Delta m_{ji}, \\ \sigma_{ji}(k+1) &= \sigma_{ji}(k) - \eta_\sigma \Delta\sigma_{ji}, \end{aligned} \tag{13}$$

with the learning-rate parameters η_m and η_σ. The terms Δm_{ji} and $\Delta\sigma_{ji}$ are also calculated as the gradient of the energy function as follows:

$$\Delta m_{ji} = \frac{\partial E}{\partial m_{ji}} = -\left(O^d - O^{(4)}(t)\right)\omega_j O_j^{(3)}(t) \cdot \frac{2\left(O_i^{(1)}(t) + \omega_{R_{ji}} O_{ji}^{(2)}(t-1) - m_{ji}\right)}{\sigma_{ji}^2},$$
$$\Delta\sigma_{ji} = \frac{\partial E}{\partial \sigma_{ji}} = -\left(O^d - O^{(4)}(t)\right)\omega_j O_j^{(3)}(t) \cdot \frac{2\left(O_i^{(1)}(t) + \omega_{R_{ji}} O_{ji}^{(2)}(t-1) - m_{ji}\right)^2}{\sigma_{ji}^3}. \tag{14}$$

Finally, the variation of recurrent coefficient $\Delta\omega_{R_{ji}}$ in Layer 2 is updated by

$$\omega_{R_{ji}}(k+1) = \omega_{R_{ji}}(k) - \eta_R \Delta\omega_{R_{ji}}, \tag{15}$$

where

$$\Delta\omega_{R_{ji}} = \frac{\partial E}{\partial \omega_{R_{ji}}} = \left(O^d - O^{(4)}(t)\right)\omega_j \left(\prod_{i,i\neq j} O_{ji}^{(2)}(t)\right) \cdot \frac{2\left(O_i^{(1)}(t) + \omega_{R_{ji}} O_{ji}^{(2)}(t-1) - m_{ji}\right)^2}{\sigma_{ji}^3} O_{ji}^{(2)}(t-1) \tag{16}$$

is again the gradient of the energy function.

4. Simulation Results

In order to evaluate the effectiveness of the proposed SCRFNN, we apply it on two benchmark chaotic time series data sets: Logistic series and Henon series. The number of data used for each benchmark problem is 2000. In particular, we use the first 1000 data for training and the remaining 1000 for validation. It will be shown that both SCFNN and SCRFNN are effective in predicting Logistic series and Henon series. But the latter has superior performance in convergence rate and prediction accuracy at the cost of slightly heavier structure (number of hidden nodes) and rules.

4.1. Logistic Chaotic Series. A Logistic chaotic series is generated by the following equation:

$$x_{k+1} = \mu x_k\left(1 - x_k\right), \quad x_k \in [0,1], \ \mu \in [0,4]. \tag{17}$$

In particular, the parameter μ is restricted within the range of $3.57 < \mu \le 4$ for chaotic behavior.

The training performance for both SCFNN and SCRFNN is demonstrated in Figure 3, where the profiles with 5, 20, and 50 learning cycles are compared in three graphs, respectively. It is observed that the proposed learning algorithm is effective in terms of fast convergence. In all the three cases, the convergence rate for the SCRFNN is faster than that for the SCFNN.

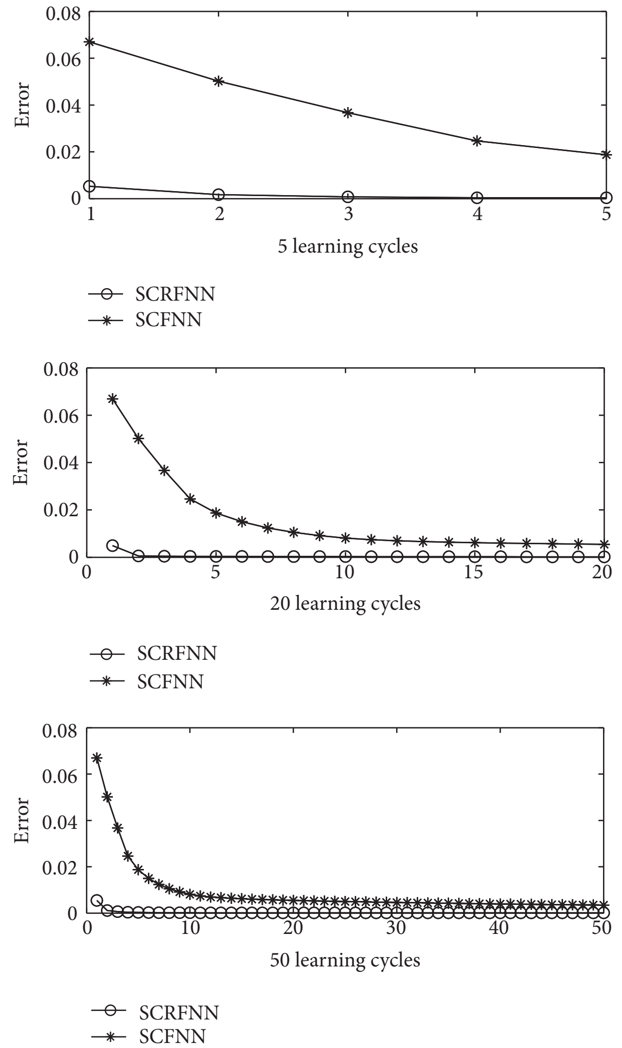

Figure 3: Comparison of convergence for 5, 20, and 50 learning cycles.

Root mean squared error (RMSE) is the main error metrics for describing the training errors. It is explicitly defined as follows:

$$\text{RMSE} = \left(\frac{1}{S-1}\sum_{i=1}^{S}\left[P_i - Q_i\right]^2\right)^{1/2}, \tag{18}$$

where S is the number of trained patterns and P_i and Q_i are the FNN derived values and the actual chaotic time series data, respectively. Table 1 shows that the RMSEs of SCFNN and SCRFNN completed 5, 20, and 50 learning cycles. In all the three cases, SCRFNN results in smaller RMSEs than SCFNN.

For the well-trained SCFNN and SCRFNN, the prediction performance is compared and shown in Figures 4 and 5. It is observed in Figure 4 that the predicted outputs from the SCFNN and the SCRFNN well match the real data. More

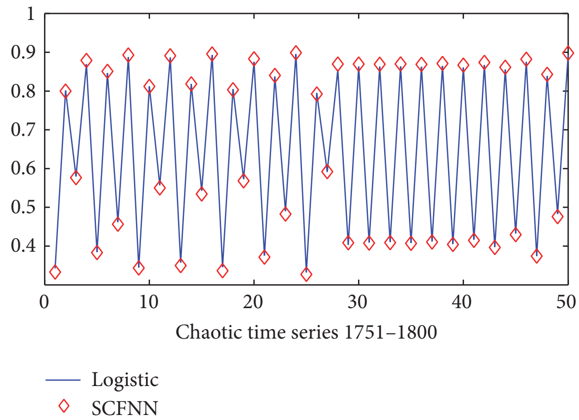

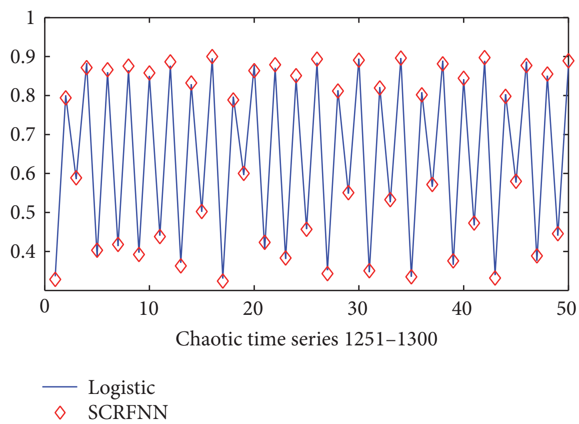

FIGURE 4: Logistic series and the predictions with SCFNN and SCRFNN.

TABLE 1: RMSE for SCFNN and SCRFNN completed 5, 20, and 50 cycles.

FNN (learning cycles)	Logistic	Henon
SCFNN (5)	7.65499*e* – 004	0.0015
SCRFNN (5)	4.51469*e* – 004	0.0014
SCFNN (20)	5.0209*e* – 004	0.0011
SCRFNN (20)	4.2344*e* – 004	6.3094*e* – 004
SCFNN (50)	4.7764*e* – 004	7.8083*e* – 004
SCRFNN (50)	4.189*e* – 004	4.4918*e* – 004

TABLE 2: Number of hidden nodes in SCFNN and SCRFNN completed 5, 20, and 50 cycles.

FNN (learning cycles)	Logistic	Henon
SCFNN (5)	4	7
SCRFNN (5)	5	7
SCFNN (20)	4	7
SCRFNN (20)	6	8
SCFNN (50)	4	7
SCRFNN (50)	5	10

specifically, the prediction errors are less significant in the SCRFNN than those in the SCFNN, as shown in Figure 5.

Finally, Table 2 shows that the numbers of hidden nodes in SCFNN and SCRFNN completed 5, 20, and 50 learning cycles. The SCRFNN has slightly more hidden nodes in all the three cases. This heavier structure of SCRFNN, together with the extra rules for recurrent path, is the cost for the aforementioned performance improvement.

4.2. Henon Chaotic Series. Henon mapping was proposed by the French astronomer Michel Henon for studying globular clusters [30]. It is one of the most famous simple dynamical systems with wide applications. In recent years, Henon mapping has been well studied in chaos theory. Its dynamics are given as follows:

$$\begin{aligned} x(k+1) &= 1 + y_k - a x^2(k), \\ y(k+1) &= b x(k). \end{aligned} \tag{19}$$

For example, chaos is produced with $a = 1.4$ and $b = 0.3$.

Similar simulation is conducted for Henon series with the corresponding results shown in Figure 6 for the comparison of convergence rates in 5, 20, and 50 learning cycles, in Figure 7 for the comparison of prediction performance, and in Figure 8 for the prediction errors. RMSEs and the numbers of hidden nodes for SCFNN and SCRFNN are also listed in Tables 1 and 2, respectively.

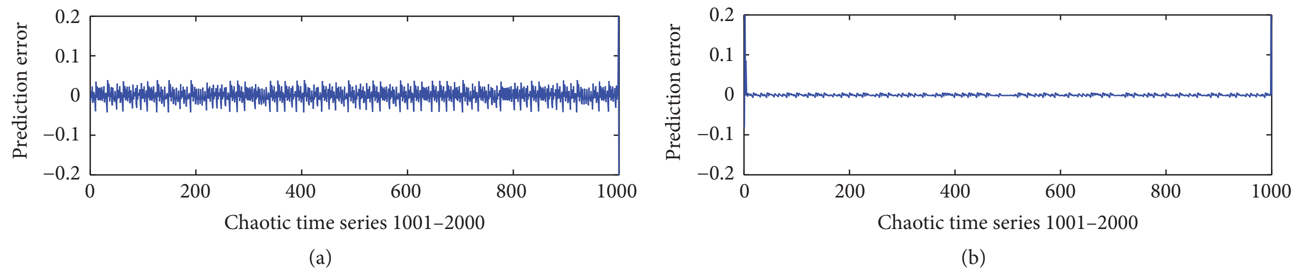

FIGURE 5: The prediction errors for well-trained SCFNN (a) and SCRFNN (b).

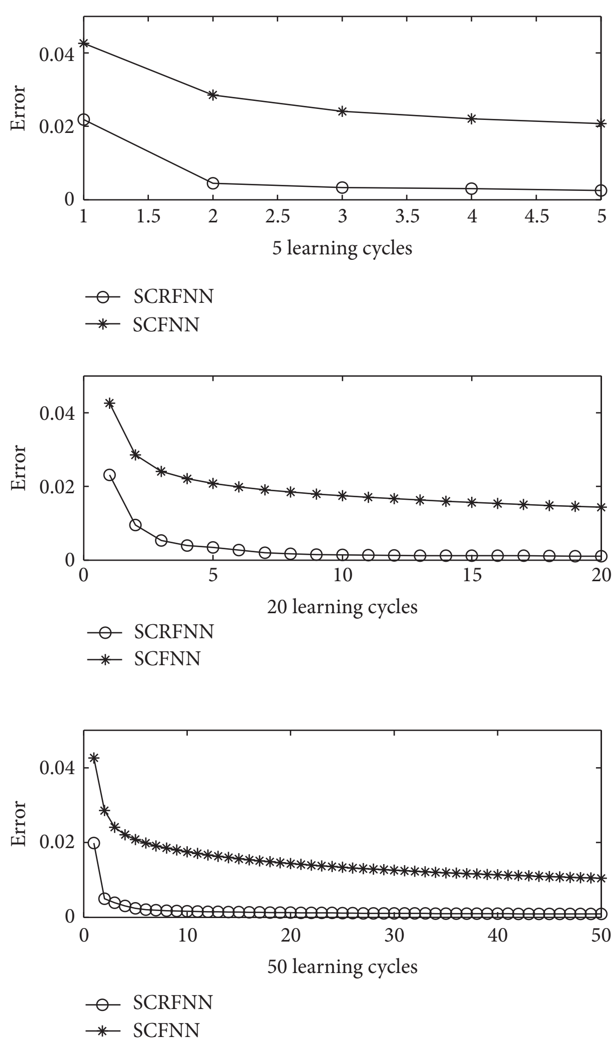

FIGURE 6: Comparison of convergence for 5, 20, and 50 learning cycles.

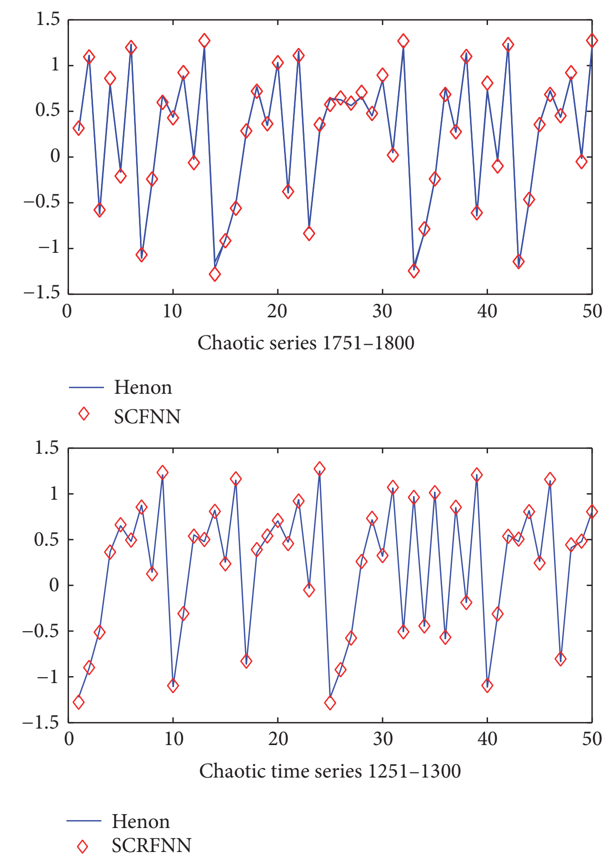

FIGURE 7: Henon series and the predictions with SCFNN and SCRFNN.

5. Conclusions

A novel type of network architecture called SCRFNN has been proposed in this paper for chaotic time series prediction. It inherits the practically implementable algorithms, the self-constructing ability, and the fuzzy logic rule from the existing SCFNN. Also, it brings new recurrent path in each node of the hidden layer of SCFNN. Two numerical studies have demonstrated that SCRFNN has superior performance in convergence rate and prediction accuracy than the existing SCFNN, at the cost of slightly heavier structure (number of hidden nodes) and extra rules for recurrent path. Hardware implementation of the proposed SCRFNN will be interesting for future research.

Competing Interests

The authors declare that they have no competing interests.

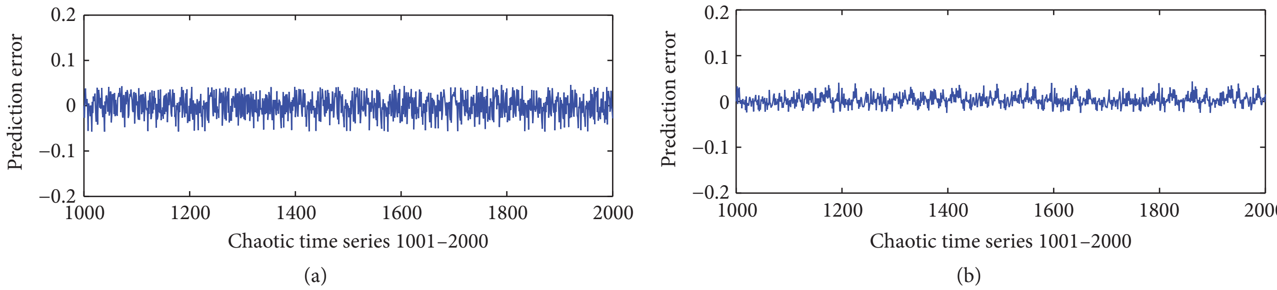

Figure 8: The prediction errors for well-trained SCFNN (a) and SCRFNN (b).

References

[1] M. Casdagli, "Nonlinear prediction of chaotic time series," *Physica D: Nonlinear Phenomena*, vol. 35, no. 3, pp. 335–356, 1989.

[2] J. Zhang, H. S.-H. Chung, and W.-L. Lo, "Chaotic time series prediction using a neuro-fuzzy system with time-delay coordinates," *IEEE Transactions on Knowledge and Data Engineering*, vol. 20, no. 7, pp. 956–964, 2008.

[3] Z. Chen, C. Lu, W. Zhang, and X. Du, "A chaotic time series prediction method based on fuzzy neural network and its application," in *Proceedings of the 3rd International Workshop on Chaos-Fractals Theories and Applications (IWCFTA '10)*, pp. 355–359, October 2010.

[4] K. Wu and T. Wang, "Prediction of chaotic time series based on RBF neural network optimization," *Computer Engineering*, vol. 39, pp. 208–216, 2013.

[5] J. Xi and H. Wang, "Modeling and prediction of multivariate series based on an improved RBF network," *Information and Control*, vol. 41, no. 2, pp. 159–164, 2012.

[6] Q.-L. Ma, Q.-L. Zheng, H. Peng, T.-W. Zhong, and L.-Q. Xu, "Chaotic time series prediction based on evolving recurrent neural networks," in *Proceedings of the 6th International Conference on Machine Learning and Cybernetics (ICMLC '07)*, vol. 6, pp. 3496–3500, IEEE, Hong Kong, August 2007.

[7] R. Chandra and M. Zhang, "Cooperative coevolution of Elman recurrent neural networks for chaotic time series prediction," *Neurocomputing*, vol. 86, pp. 116–123, 2012.

[8] Y. Zuo and T. Wang, "Prediction for chaotic time series of BP neural network based on differential evolution," *Computer Engineering and Applications*, vol. 49, pp. 160–163, 2013.

[9] H.-T. Zhang and Z. Chen, "Consensus acceleration in a class of predictive networks," *IEEE Transactions on Neural Networks and Learning Systems*, vol. 25, no. 10, pp. 1921–1927, 2014.

[10] Z. Peng, D. Wang, Z. Chen, X. Hu, and W. Lan, "Adaptive dynamic surface control for formations of autonomous surface vehicles with uncertain dynamics," *IEEE Transactions on Control Systems Technology*, vol. 21, no. 2, pp. 513–520, 2013.

[11] Z. Chen and T. Iwasaki, "Circulant synthesis of central pattern generators with application to control of rectifier systems," *IEEE Transactions on Automatic Control*, vol. 53, no. 1, pp. 273–286, 2008.

[12] L. Zhu, Z. Chen, and T. Iwasaki, "Oscillation, orientation, and locomotion of underactuated multilink mechanical systems," *IEEE Transactions on Control Systems Technology*, vol. 21, no. 5, pp. 1537–1548, 2013.

[13] F.-J. Lin, C.-H. Lin, and P.-H. Shen, "Self-constructing fuzzy neural network speed controller for permanent-magnet synchronous motor drive," *IEEE Transactions on Fuzzy Systems*, vol. 9, no. 5, pp. 751–759, 2001.

[14] W.-D. Weng, R.-C. Lin, and C.-T. A. Hsueh, "The design of an SCFNN based nonlinear channel equalizer," *Journal of Information Science and Engineering*, vol. 21, no. 4, pp. 695–709, 2005.

[15] Y. Li, Q. Peng, and B. Hu, "Remote controller design of networked control systems based on self-constructing fuzzy neural network," in *Proceedings of the 2nd International Symposium on Neural Networks: Advances in Neural Networks (ISNN '05)*, pp. 143–149, Chongqing, China, June 2005.

[16] Z. Chen and T. Iwasaki, "Matrix perturbation analysis for weakly coupled oscillators," *Systems and Control Letters*, vol. 58, no. 2, pp. 148–154, 2009.

[17] Z. Chen, T. Iwasaki, and L. Zhu, "Neural control for coordinated natural oscillation patterns," *Systems and Control Letters*, vol. 62, no. 8, pp. 693–698, 2013.

[18] A. Waibel, T. Hanazawa, G. Hinton, K. Shikano, and K. J. Lang, "Phoneme recognition using time-delay neural networks," *IEEE Transactions on Acoustics, Speech, and Signal Processing*, vol. 37, no. 3, pp. 328–339, 1989.

[19] G. Kechriotis, E. Zervas, and E. Manolakos, "Using recurrent neural networks for blind equalization of linear and nonlinear communications channels," in *Proceedings of the Military Communications Conference (MILCOM '92) Conference Record. Communications-Fusing Command, Control and Intelligence*, pp. 784–788, IEEE, 1992.

[20] R.-C. Lin, W.-D. Weng, and C.-T. Hsueh, "Design of an SCRFNN-based nonlinear channel equaliser," *IEE Proceedings—Communications*, vol. 152, no. 6, p. 771, 2005.

[21] G. Kechriotis and E. S. Manolakos, "Using recurrent neural network for nonlinear and chaotic signal processing," in *Proceedings of the International Conference on Acoustics, Speech, and Signal Processing (ICASSP '93)*, pp. 465–469, Minneapolis, Minn, USA, April 1993.

[22] H. Kantz and T. Schreiber, *Nonlinear Time Series Analysis*, Cambridge University Press, New York, NY, USA, 1997.

[23] A. Basharat and M. Shah, "Time series prediction by chaotic modeling of nonlinear dynamical systems," in *Proceedings of the IEEE 12th International Conference on Computer Vision*, pp. 1941–1948, September 2009.

[24] F.-J. Lin, R.-F. Fung, and R.-J. Wai, "Comparison of sliding-mode and fuzzy neural network control for motor-toggle servomechanism," *IEEE/ASME Transactions on Mechatronics*, vol. 3, no. 4, pp. 302–318, 1998.

[25] F.-J. Lin, W.-J. Hwang, and R.-J. Wai, "A supervisory fuzzy neural network control system for tracking periodic inputs," *IEEE Transactions on Fuzzy Systems*, vol. 7, no. 1, pp. 41–52, 1999.

[26] C.-T. Lin, "A neural fuzzy control system with structure and parameter learning," *Fuzzy Sets and Systems*, vol. 70, no. 2-3, pp. 183–212, 1995.

[27] F.-J. Lin, R.-J. Wai, and C.-C. Lee, "Fuzzy neural network position controller for ultrasonic motor drive using push-pull DC-DC converter," *IEE Proceedings: Control Theory and Applications*, vol. 146, no. 1, pp. 99–107, 1999.

[28] G. Kechriotis, E. Zervas, and E. S. Manolakos, "Using recurrent neural networks for adaptive communication channel equalization," *IEEE Transactions on Neural Networks*, vol. 5, no. 2, pp. 267–278, 1994.

[29] R. J. Williams and D. Zipser, "A learning algorithm for continually running fully recurrent neural networks," *Neural Computation*, vol. 1, no. 2, pp. 270–280, 1989.

[30] M. Hénon, "A two-dimensional mapping with a strange attractor," *Communications in Mathematical Physics*, vol. 50, no. 1, pp. 69–77, 1976.

Hindawi Publishing Corporation
Mathematical Problems in Engineering
Volume 2016, Article ID 7324508, 14 pages
http://dx.doi.org/10.1155/2016/7324508

Research Article

Design and Experimental Verification of Robust Motion Synchronization Control with Integral Action

Chen Peng,[1] Bo Zhu,[1] and Keqi Wei[2]

[1] *School of Aeronautics and Astronautics, University of Electronic Science and Technology of China, Chengdu, Sichuan 611731, China*
[2] *Department of Electrical and Computer Engineering, McMaster University, Hamilton, ON, Canada L8S 4K1*

Correspondence should be addressed to Chen Peng; penson@buaa.edu.cn

Received 24 June 2016; Accepted 19 September 2016

Academic Editor: Steffi Knorn

A robust attitude motion synchronization problem is investigated for multiple 3-degrees-of-freedom (3-DOF) helicopters with input disturbances. The communication topology among the helicopters is modeled by a directed graph, and each helicopter can only access the angular position measurements of itself and its neighbors. The desired trajectories are generated online and not accessible to all helicopters. The problem is solved by embedding in each helicopter some finite-time convergent (FTC) estimators and a distributed controller with integral action. The FTC estimators generate the estimates of desired angular acceleration and the derivative of the local neighborhood synchronization errors. The distributed controller stabilizes the tracking errors and attenuates the effects of input disturbances. The conditions under which the tracking error of each helicopter converges asymptotically to zero are identified, and, for the cases with nonzero tracking errors, some inequalities are derived to show the relationship between the ultimate bounds of tracking errors and the design parameters. Simulation and experimental results are presented to demonstrate the performance of the controllers.

1. Introduction

In the field of multivehicle cooperative control, robust consensus tracking under model uncertainties and exogenous disturbances has received increasing attention in recent years, where the output (or state) of each vehicle is required to robustly track a common, desired trajectory. For instance, switching controllers or sliding-mode controllers were designed in works [1–3] to reject input disturbances; a sliding-mode disturbance observer is combined with a consensus tracking algorithm in recent work [4] to improve the robustness and control accuracy of a multimotor system. Alternative robust control approaches include the ones based on uncertainty and disturbance estimators as in works [5–7], adaptive control approach [8], and the output-regulation approach [9].

In practice, integral control (IC) is widely used to attenuate disturbances in various (single) vehicle systems. This mainly owes to its structural simplicity and the well-known performance property that IC can asymptotically reject constant input disturbances. Noting these facts, many researchers begin to study IC-based robust control schemes for multivehicle systems (MVSs) as in [10–12]. In particular, the recent work [10] shows that PI controllers successfully attenuate constant disturbances in the network of multiple single-integrator dynamics or the network of multiple double-integrator dynamics.

Another practical issue encountered in many control systems is the lack of sensors. As a result, state observers are often needed to generate the estimates of some necessary states. State observers can be roughly classified into two types: model-dependent ones and model-independent ones. As two representative model-dependent observers, Luenberger observer and Kalman filter suffer from the limitation that the estimation accuracy cannot be guaranteed when the system model suffers from severe uncertainties. To deal with this problem, many model-independent observers are proposed. For instance, some higher-order sliding modes (HOSM) observers (differentiators) were designed in work [13, 14] to ensure finite-time convergence even in the presence of input disturbances.

The main objective of this paper is to use integral control to improve the robustness of a distributed control algorithm for consensus tracking without velocity measurements. The effectiveness of the approach is proved by showing that (a) the resulting tracking errors are ultimately bounded for any input disturbances satisfying a simple Lipschitz-constant condition, and (b) zero-error asymptotic tracking is achieved for a constant input disturbance. The key technical differences between this paper and work [10] are summarized as follows:

(1) The paper [10] considers the consensus problem without a common reference. In contrast, this paper considers a consensus tracking problem, where a common desired trajectory exists (and is supposed to be accessible only to partial vehicles in the group). In [10], velocity signals were used in the control design for second-order systems. We here assume that neither the velocity of leader nor the velocity of neighboring vehicles is accessible for control design.

(2) Concerning the robustness improvement owing to integral control, the discussion in work [10] is restricted to the rather special case with constant input disturbances. This is not the case in this paper. Actually, we will use the concepts of input-to-state stability to study the general cases where the disturbances are nonconstants and are not completely rejected.

(3) In work [10], the controller performance is verified by numerical simulation. In this paper, both numerical simulation results and experimental results on three 3-DOF helicopters are presented, to demonstrate the performance improvement owing to the use of integral control.

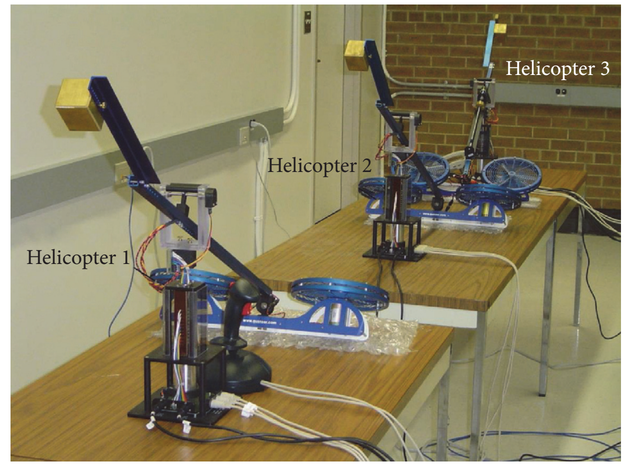

Figure 1: Experimental platform of "three 3-DOF helicopters" (see [15]).

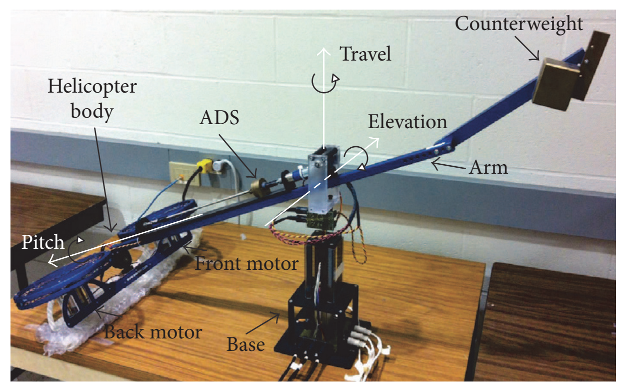

Figure 2: 3-DOF helicopter with ADS (see [5]).

The experimental platform of "three 3-DOF helicopters" used in this paper is shown in Figure 1. The single laboratory 3-DOF helicopter with a so-called active disturbance system (ADS) is the same as that in [5] and is shown in Figure 2. This experimental apparatus was developed by Quanser Consulting Inc. for the purpose of control education and research [15–21].

The rest of this paper is organized as follows. In Section 2, some preliminary knowledge is described and the problem is formulated. The robust distributed consensus tracking controllers are designed in Section 3. Numerical simulation and experimental results are presented in Section 4. Some concluding remarks are drawn in Section 5.

2. Preliminaries

2.1. Notation and Graph Theory. For matrix M, M^{-1} denotes its inversion and rank(M) denotes its rank. $I_n \in R^{n\times n}$ refers to the identity matrix. For vector $X \in R^{n\times 1}$ and matrix $M = [m_{ij}] \in R^{m\times n}$, $\|X\|_2 = (\sum_{i=1}^{n} |x_i|^2)^{1/2}$, $\|X\|_\infty = \max_{1\le i\le n}|x_i|$, $\|M\|_\infty = \max_{1\le i\le m}\sum_{j=1}^{n}|m_{ij}|$, and $\|M\|_2 = (\lambda_{\max}(M^TM))^{1/2}$, where $\lambda_{\max}(\cdot) = \max_i|\lambda_i|$ with λ_i being eigenvalues. $\mathbf{0}_n$ refers to n-dimensional column vector with all elements being 0. $|a|$ denotes absolute value (modulus) of real number a.

The notations related to ith 3-DOF helicopter (see Figure 2), $i \in \mathcal{I} = \{1,\ldots,n\}$, are listed in Notations.

The communication networks of n helicopters can be modeled by directed graph $\mathcal{G}(\mathcal{V},\mathcal{E},\mathcal{A})$, where $\mathcal{V} = \{v_1, v_2, \ldots, v_n\}$, $\mathcal{E} \subset \mathcal{V}\times\mathcal{V}$, and nonnegative matrix $\mathcal{A} = [a_{ij}] \in R^{n\times n}$ denote the set of nodes, the set of edges, and the weighted adjacency matrix of $\mathcal{G}$, respectively. Node v_i $(i = 1,\ldots,n)$ represents ith helicopter, and an edge $(v_j, v_i) \in \mathcal{E}$ denotes that ith helicopter can obtain information from jth helicopter; that is, v_j is a neighbor of v_i. Use N_i to denote all the neighbors of v_i, and $N_i \subset \mathcal{V}$. A directed path from v_i to v_j is a sequence of ordered edges of form $(v_i, v_{i_1}), (v_{i_1}, v_{i_2}), \ldots, (v_{i_l}, v_j)$, with distinct nodes v_{i_k}, $k = 1,2,\ldots,l$, and v_j is said to be reachable from v_i. A node is called the root node and $\mathcal{G}$ is said to have a directed spanning tree, if all the other nodes are reachable from this node.

The elements of the weighted adjacency matrix $\mathcal{A}$ satisfy $a_{ii} = 0$ and $a_{ij} > 0$ $(i, j = 1,\ldots,n$ and $j \ne i)$ if and only if $(v_j, v_i) \in \mathcal{E}$. The Laplacian matrix of $\mathcal{G}$ is denoted by $L = [l_{ij}] \in R^{n\times n}$, where $l_{ij} = -a_{ij}$, if $i \ne j$, and $l_{ii} = \sum_{j\in N_i} a_{ij}$. Note that the desired trajectory information is not accessible to all helicopters in this paper. Use constant matrix

$\overline{B} = \text{diag}(b_1, \ldots, b_n) \in R^{n\times n}$, which is defined as $b_i > 0$ if ith helicopter can access the desired trajectory information and otherwise $b_i = 0$, to describe this fact by allowing $b_i = 0$ for some $i \in \mathcal{I}$.

2.2. Problem Formulation. The elevation and pitch motions of ith helicopter can be modeled as follows (see [5] or [21]):

$$\begin{aligned} J_{ei}\ddot{\alpha}_i(t) &= K_{fi}l_{ai}\cos(\beta_i(t))V_{si}(t) - m_i g l_{ai}\cos(\alpha_i(t)) \\ &\quad + f_{\alpha i}(t), \quad i \in \mathcal{I}, \\ J_{pi}\ddot{\beta}_i(t) &= K_{fi}l_{hi}V_{di}(t) + f_{\beta i}(t), \quad i \in \mathcal{I}, \end{aligned} \tag{1}$$

where

$$\begin{aligned} V_{si}(t) &= V_{fi}(t) + V_{bi}(t), \quad i \in \mathcal{I}, \\ V_{di}(t) &= V_{fi}(t) - V_{bi}(t), \quad i \in \mathcal{I}. \end{aligned} \tag{2}$$

The pitch angle is limited to within $(-\pi/2, \pi/2)$ mechanically.

We made the following assumption on $f_{\alpha i}(t)$ and $f_{\beta i}(t)$.

Assumption 1. For each $i \in \mathcal{I}$, the first-order derivatives of $f_{\alpha i}(t)$ and $f_{\beta i}(t)$ with respect to t exist and are piecewise continuous and bounded for all $t \geq 0$.

As shown in recent work [5], by applying the standard normalization and feedback linearization technique, the above nonlinear helicopter model can be reduced to the following 2-dimensional, disturbed double integrators:

$$\ddot{y}_i = u_i + d_i, \quad i \in \mathcal{I}, \tag{3}$$

where $y_i = (\alpha_i(t), \beta_i(t))^T \in R^2$, $u_i = [u_{\alpha i}, u_{\beta i}]^T \in R^2$, and the new disturbances $d_i = [d_{\alpha i}, d_{\beta i}]^T \in R^2$.

Under Assumption 1, $\dot{d}_i = (\dot{d}_{\alpha i}, \dot{d}_{\beta i})^T$ also exist and are bounded. Define

$$\begin{aligned} \overline{d}_d &= (\overline{d}_{d\alpha}, \overline{d}_{d\beta})^T \\ &= \left(\max_{1\leq i\leq n}\left(\sup_{t\geq 0}\left|\dot{d}_{\alpha i}(t)\right|\right), \max_{1\leq i\leq n}\left(\sup_{t\geq 0}\left|\dot{d}_{\beta i}(t)\right|\right)\right)^T, \end{aligned} \tag{4}$$

where $\overline{d}_{d\alpha}$ and $\overline{d}_{d\beta}$ are positive scalars.

For each $i \in \mathcal{I}$, we define $y_i = (\alpha_i, \beta_i)^T \in R^2$ and use $y_d = (\alpha_d, \beta_d)^T \in R^2$ to denote the desired attitude trajectory for y_i, which may be time-varying but are second-order differentiable with respect to t. Then, the objective of this paper is to design u_i for (3) to achieve robust attitude synchronization; that is, $y_i(t) \to y_d(t)$ for each $i \in \mathcal{I}$ as $t \to +\infty$.

3. Design of Distributed Controllers without Velocity Measurements

3.1. Controller Design. Noting that $u_{\alpha i}$ and $u_{\beta i}$ for (3) can be designed in the same way, we thus introduce new unified variable $\rho \in \{\alpha, \beta\}$ and define

$$\widetilde{\rho}_i = \rho_i - \rho_d, \quad i \in \mathcal{I}, \tag{5a}$$

$$\widetilde{\boldsymbol{\rho}} = [\widetilde{\rho}_1, \ldots, \widetilde{\rho}_n]^T \in R^n, \tag{5b}$$

$$\widetilde{\rho}_{ij} = \rho_i - \rho_j, \quad i, j \in \mathcal{I}, \tag{5c}$$

$$e_{\rho i} = b_i\widetilde{\rho}_i + \sum_{j\in N_i} a_{ij}\widetilde{\rho}_{ij}. \tag{5d}$$

In [8, 22], error $e_{\rho i}$ is called local neighborhood synchronization error (LNSE).

For the considered helicopter, only angular position sensors (encoders) are equipped. Besides, we assume that the desired velocity is not accessible to any helicopter. To deal with this problem, we consider the following distributed controllers:

$$\begin{aligned} u_{\rho i}(t) = \frac{1}{k_i}\Bigg(&\sum_{j\in N_i} a_{ij}u_{\rho j}(t) + b_i\hat{\ddot{\rho}}_d(t) - k^P_{\rho i}e_{\rho i}(t) \\ &- k^D_{\rho i}\hat{\dot{e}}_{\rho i}(t) - k^I_{\rho i}\int_0^t e_{\rho i}(\tau)\,d\tau\Bigg), \end{aligned} \tag{6}$$

where $k^P_{\rho i}$, $k^I_{\rho i}$, and $k^D_{\rho i}$ are positive control gains, $k_i = b_i + \sum_{j\in N_i} a_{ij}$, $\hat{\ddot{\rho}}_d(t)$, and $\hat{\dot{e}}_{\rho i}(t)$ denote the estimates of $\ddot{\rho}_d(t)$ and $\dot{e}_{\rho i}(t)$, respectively. We construct the following systems to generate $\hat{\ddot{\rho}}_d(t)$ and $\hat{\dot{e}}_{\rho i}(t)$. Specifically, the third-order FTC estimators

$$\begin{aligned} \dot{\hat{\rho}}_d &= -\lambda_2\overline{L}^{1/3}_{\rho d}\left|\hat{\rho}_d - \rho_d\right|^{2/3}\text{sign}(\hat{\rho}_d - \rho_d) \\ &\quad - \mu_2(\hat{\rho}_d - \rho_d) + \hat{\dot{\rho}}_d, \\ \dot{\hat{\dot{\rho}}}_d &= -\lambda_1\overline{L}^{1/2}_{\rho d}\left|\hat{\dot{\rho}}_d - \dot{\hat{\rho}}_d\right|^{1/2}\text{sign}\left(\hat{\dot{\rho}}_d - \dot{\hat{\rho}}_d\right) \\ &\quad - \mu_1\left(\hat{\dot{\rho}}_d - \dot{\hat{\rho}}_d\right) + \hat{\ddot{\rho}}_d, \\ \dot{\hat{\ddot{\rho}}}_d &= -\lambda_0\overline{L}_{\rho d}\,\text{sign}\left(\hat{\ddot{\rho}}_d - \dot{\hat{\dot{\rho}}}_d\right) - \mu_0\left(\hat{\ddot{\rho}}_d - \dot{\hat{\dot{\rho}}}_d\right), \end{aligned} \tag{7}$$

are for $\hat{\ddot{\rho}}_d(t)$, and the following second-order FTC estimators are for $\hat{\dot{e}}(t)$:

$$\begin{aligned} \dot{\hat{e}}_{\rho i} &= -\lambda_1\overline{L}^{1/2}_e\left|\hat{e}_{\rho i} - e_{\rho i}\right|^{1/2}\text{sign}\left(\hat{e}_{\rho i} - e_{\rho i}\right) \\ &\quad - \mu_1\left(\hat{e}_{\rho i} - e_{\rho i}\right) + \hat{\dot{e}}_{\rho i}, \\ \dot{\hat{\dot{e}}}_{\rho i} &= -\lambda_0\overline{L}_e\,\text{sign}\left(\hat{\dot{e}}_{\rho i} - \dot{\hat{e}}_{\rho i}\right) - \mu_0\left(\hat{\dot{e}}_{\rho i} - \dot{\hat{e}}_{\rho i}\right), \quad i \in \mathcal{I}, \end{aligned} \tag{8}$$

where $\hat{\rho}_d$, $\hat{\dot{\rho}}_d$, and $\hat{e}_{\rho i}$ are the estimates of ρ_d, $\dot{\rho}_d$, and $e_{\rho i}$, respectively; ρ_d and $e_{\rho i}$ are consisting of a locally bounded

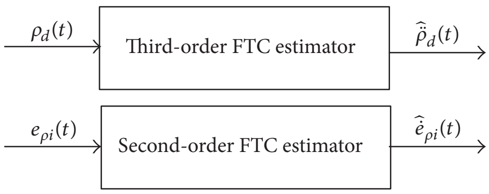

Figure 3: The way to obtain $\hat{\dot{\rho}}_d(t)$ and $\hat{\dot{e}}(t)$.

Lebesgue-measurable noise with unknown features and an unknown base signal $\rho_{d0}(t)$ and $e_{\rho i0}$ whose second and first derivative have an known Lipschitz constant $\overline{L}_{\rho d} > 0$ and $\overline{L}_e > 0$, respectively; λ_i and $\mu_i > 0$, $i = 0, 1, 2$, are the design parameters of the FTC estimators.

This estimation scheme is illustrated in Figure 3.

We have the following result for the above two FTC estimators [14, Theorem 1].

Lemma 2. *Let $\{\lambda_i\}$ and $\{\mu_i\}$ in (7) and (8) be recursively chosen as in Theorem 1 of [13, 14]. Then, the estimation errors achieve zero in the absence of input noises after finite time t_c of transient process. The convergence of the estimation errors is uniform in the sense that the convergence time is uniformly bounded by finite time t_c which is a locally bounded function of initial estimation errors.*

Remark 3. According to Lemma 2, in the absence of input noises, after finite time t_{ci} $(i \in \mathcal{I})$, the following equalities hold:

$$\begin{aligned} &\hat{\dot{\rho}}_d - \dot{\rho}_d = 0, \\ &\hat{\ddot{\rho}}_d - \ddot{\rho}_d = 0, \\ &\dot{e}_{\rho i} - \hat{\dot{e}}_{\rho i} = 0, \quad i \in \mathcal{I}. \end{aligned} \tag{9}$$

Remark 4. Note that the neighbors' control signals $u_{\rho j}(t)$ $(j \in N_i)$ are used in (6) and then a possible implementation loop issue arises in practical applications. As discussed in work [5], if the sample frequency is high enough, this problem can be resolved with using the neighbors' control signals obtained during the previous sampling period, that is, $u_{\rho j}(t-\tau)$, where τ denotes the fixed sampling step and $\tau = 0.001$ sec in the following numerical simulations and experiments.

3.2. Analysis of the Closed-Loop Stability. Before the closed-loop stability analysis, we need to establish and analyse the relationship between tracking errors $\tilde{\rho}_i$ and LNSEs $e_{\rho i}$, $i \in \mathcal{I}$. Define

$$\mathbf{E}_\rho = \left[e_{\rho 1}, \ldots, e_{\rho n}\right]^T \in R^n, \quad \rho \in \{\alpha, \beta\}. \tag{10}$$

From (5c), $\tilde{\rho}_{ij} = \rho_i - \rho_j = \tilde{\rho}_i - \tilde{\rho}_j$; then from (5d), $e_{\rho i} = b_i\tilde{\rho}_i + \sum_{j\in N_i} a_{ij}(\tilde{\rho}_i - \tilde{\rho}_j)$ for each $\rho \in \{\alpha, \beta\}$. Then, with L and $\overline{B}$ as defined in Section 2.1, the following relationship equation between the tracking errors and LNSEs is derived:

$$\mathbf{E}_\rho(t) = \left(L + \overline{B}\right)\tilde{\boldsymbol{\rho}}(t), \quad \rho \in \{\alpha, \beta\}, \tag{11}$$

where $\operatorname{rank}(L + \overline{B})$ is determined by the communication topology which satisfies the following condition in this paper.

Assumption 5. The desired trajectory information ρ_d, $\rho \in \{\alpha, \beta\}$, has directed paths to all helicopters.

According to [23, Lemma 1.6], all eigenvalues of $L+\overline{B}$ have positive real parts under Assumption 5. Then, the following lemma is obtained directly.

Lemma 6 (see [23, Lemma 1.6]). *Under Assumption 5, matrix $L + \overline{B}$ is full rank, that is,* $\operatorname{rank}(L + \overline{B}) = n$.

Thus, the relationship equation (11) implies that, under Assumption 5, the objective $\tilde{\boldsymbol{\rho}}(t) \to \mathbf{0}_n$ and $\dot{\tilde{\boldsymbol{\rho}}}(t) \to \mathbf{0}_n$ as $t \to +\infty$, $\rho \in \{\alpha, \beta\}$, can be achieved by driving $\mathbf{E}_\rho(t)$ and $\dot{\mathbf{E}}_\rho(t)$ to zero as $t \to +\infty$, respectively.

Applying (6) to (3) gives

$$\begin{aligned} k_i\ddot{\rho}_i(t) = &\sum_{j\in N_i} a_{ij}\left(\ddot{\rho}_j(t) - d_{\rho j}(t)\right)(t) + b_i\hat{\ddot{\rho}}_d(t) \\ &- k^P_{\rho i}e_{\rho i}(t) - k^D_{\rho i}\hat{\dot{e}}_{\rho i}(t) - k^I_{\rho i}\int_0^t e_{\rho i}(\tau)\,d\tau \\ &+ k_i d_{\rho i}. \end{aligned} \tag{12}$$

With (5d) and (12), we can further get

$$\dddot{e}_{\rho i} + k^D_{\rho i}\ddot{e}_{\rho i} + k^P_{\rho i}\dot{e}_{\rho i} + k^I_{\rho i}e_{\rho i} = \dot{\delta}_{\rho i}, \quad \rho \in \{\alpha, \beta\}, \ i \in \mathcal{I}, \tag{13}$$

where $\delta_{\rho i} = b_i(\hat{\ddot{\rho}}_d - \ddot{\rho}_d) + k^D_{\rho i}(\dot{e}_{\rho i} - \hat{\dot{e}}_{\rho i}) + \Delta_{\rho i}$ and $\Delta_{\rho i}$ is defined as

$$\Delta_{\rho i} = k_i d_{\rho i} - \sum_{j\in N_i} a_{ij}d_{\rho j}. \tag{14}$$

Define

$$\boldsymbol{\delta}_\rho = \left[\delta_{\rho 1}, \ldots, \delta_{\rho n}\right]^T \in R^n, \quad \rho \in \{\alpha, \beta\}, \tag{15}$$

$$\boldsymbol{\Delta}_\rho = \left[\Delta_{\rho 1}, \ldots, \Delta_{\rho n}\right]^T \in R^n, \quad \rho \in \{\alpha, \beta\}, \tag{16}$$

$$\mathbf{d}_\rho = \left[d_{\rho 1}, \ldots, d_{\rho n}\right]^T \in R^n, \quad \rho \in \{\alpha, \beta\}, \tag{17}$$

$$\bar{\mathbf{t}}_c = \left[t_{c1}, \ldots, t_{cn}\right]^T \in R^n. \tag{18}$$

Then, the following result is clear based on Lemma 2.

Lemma 7. *There exists $\bar{t}_{c\,max} = \|\bar{\mathbf{t}}_c\|_\infty$ such that, in the absence of input noises,*

$$\boldsymbol{\delta}_\rho = \boldsymbol{\Delta}_\rho, \quad \forall t \geq \bar{t}_{c\,max}, \ \rho \in \{\alpha, \beta\}. \tag{19}$$

Therefore, after finite time $\bar{t}_{c\max}$, (13) is the same as follows:

$$\dddot{e}_{\rho i} + k^D_{\rho i}\ddot{e}_{\rho i} + k^P_{\rho i}\dot{e}_{\rho i} + k^I_{\rho i}e_{\rho i} = \dot{\Delta}_{\rho i}, \quad \rho \in \{\alpha, \beta\}, \ i \in \mathcal{I}. \tag{20}$$

Define

$$A_{\rho i} = \begin{bmatrix} 0 & 1 & 0 \\ 0 & 0 & 1 \\ -k^I_{\rho i} & -k^P_{\rho i} & -k^D_{\rho i} \end{bmatrix} \in R^{3\times 3}, \quad \rho \in \alpha, \beta, \ i \in \mathcal{I}, \tag{21}$$

$$B_{\rho i} = \begin{bmatrix} 0 & 0 & 1 \end{bmatrix}^T \in R^{3\times 1}, \quad \rho \in \alpha, \beta, \ i \in \mathcal{I}. \tag{22}$$

Then, (20) can be written as

$$\left[\dot{e}_{\rho i}, \ddot{e}_{\rho i}, \dddot{e}_{\rho i}\right]^T = A_{\rho i}\left[e_{\rho i}, \dot{e}_{\rho i}, \ddot{e}_{\rho i}\right]^T + B_{\rho i}\dot{\Delta}_{\rho i}, \quad \rho \in \alpha, \beta, \ i \in \mathcal{I}. \tag{23}$$

Furthermore, based on Lemma 7, by applying Routh-Hurwitz stability criterion and Lemma A.1 in Appendix to forced systems (13) with $\dot{\delta}_{\rho i}$ as inputs, the following theorem is obtained.

Theorem 8. *Consider systems (13) under Assumptions 1 and 5 and the following parameter condition:*

$$k^D_{\rho i}, k^P_{\rho i}, k^I_{\rho i} > 0, \qquad k^D_{\rho i} k^P_{\rho i} > k^I_{\rho i}. \tag{24}$$

Then, for each $\rho \in \{\alpha, \beta\}$, in the absence of noise,

(1) *the system trajectories $\mathbf{E}_\rho$, $\dot{\mathbf{E}}_\rho$, $\widetilde{\boldsymbol{\rho}}$, and $\dot{\widetilde{\boldsymbol{\rho}}}$ are globally bounded;*

(2) $\mathbf{E}_\rho \to 0$, $\dot{\mathbf{E}}_\rho \to 0$, $\widetilde{\boldsymbol{\rho}} \to 0$, *and* $\dot{\widetilde{\boldsymbol{\rho}}} \to 0$ *as* $t \to +\infty$ *if* $\dot{\mathbf{d}}_\rho(t) \to 0$ *as* $t \to +\infty$*;*

(3) *for the general cases with nonvanishing $\dot{\mathbf{d}}_\rho(t)$, there exists $\bar{t}_\rho > \bar{t}_{c\,max}$ such that, under any initial condition,*

$$\left\|\mathbf{E}_\rho(t)\right\|_2 \le b_\rho, \quad \forall t \ge \bar{t}_\rho, \tag{25}$$

$$\left\|\widetilde{\boldsymbol{\rho}}(t)\right\|_2 \le \left\|\left(L + \overline{B}\right)^{-1}\right\|_2 b_\rho, \quad \forall t \ge \bar{t}_\rho, \tag{26}$$

where

$$b_\rho = \frac{2\sqrt{n}\left\|L + \overline{B}\right\|_\infty \bar{d}_{d\rho}}{\theta} \cdot \max_{1\le i\le n}\left(\lambda_{max}\left(P_{\rho i}\right)\sqrt{\frac{\lambda_{max}\left(P_{\rho i}\right)}{\lambda_{min}\left(P_{\rho i}\right)}}\right), \tag{27}$$

and $0 < \theta < 1$, $P_{\rho i}$ are the solutions of the Lyapunov equations

$$P_{\rho i}A_{\rho i} + A^T_{\rho i}P_{\rho i} = -I_3, \quad \rho \in \{\alpha, \beta\}, \tag{28}$$

with $A_{\rho i}$ defined by (21).

Proof. Using (14), (16), and (17), the relationships between $\dot{\Delta}_{\rho i}$ and $\dot{d}_{\rho i}$ can be written in a compact form as

$$\dot{\boldsymbol{\Delta}}_\rho = \left(L + \overline{B}\right)\dot{\mathbf{d}}_\rho, \quad \rho \in \{\alpha, \beta\}. \tag{29}$$

Then, with (4), it follows that

$$\left\|\dot{\boldsymbol{\Delta}}_\rho(t)\right\|_\infty \le \left\|L + \overline{B}\right\|_\infty \left\|\dot{\mathbf{d}}_\rho(t)\right\|_\infty \le \left\|L + \overline{B}\right\|_\infty \bar{d}_{d\rho}, \quad \forall t \ge 0, \ \rho \in \{\alpha, \beta\}. \tag{30}$$

Moreover, for $\rho \in \{\alpha, \beta\}$, based on Lemma 6, under Assumption 5, $\dot{\boldsymbol{\Delta}}_\rho \to \mathbf{0}_n$ as $t \to +\infty$ if and only if $\dot{\mathbf{d}}_\rho \to \mathbf{0}_n$ as $t \to +\infty$. Thus, under Assumptions 1 and 5 and parameter conditions (24), it is straightforward to derive the points (1)-(2) with these results and Lemmas 6 and 7.

The detailed proof of point (3) is the same as [5, Theorem 2] and hence omitted. □

Remark 9. As shown in Theorem 8, by FTC differentiators (7) and (8) in the absence of input noises, for the case without angular velocity measurements, if condition $\lim_{t\to+\infty}\dot{d}_{\rho i}(t) = 0$ is satisfied, the distributed controllers (6) are capable of achieving zero-error attitude-trajectory tracking for each helicopter in the group of helicopters. Thus, the distributed consensus attitude-trajectory zero-error tracking for the group of helicopters is achieved under this condition ($\lim_{t\to+\infty}\dot{d}_{\rho i}(t) = 0$). If this condition is not satisfied, the ultimate bounds of attitude-trajectory tracking errors $\widetilde{\rho}_i$ resulting from controllers (6) are globally bounded for $i \in \mathcal{I}$ and ultimately bounded with ultimate bounds depending on parameters $k^P_{\rho i}, k^D_{\rho i}, k^I_{\rho i}$ which can make the term $\max_{1\le i\le n}(\lambda_{\max}(P_{\rho i})\sqrt{\lambda_{\max}(P_{\rho i})/\lambda_{\min}(P_{\rho i})})$ small enough. Future efforts will be devoted to the optimization problem of the three parameters such that the term is minimized.

Remark 10. If delay τ in neighbors' control inputs $u_{\rho j}(t-\tau)$ is systematically considered, the obtained error equations (13) are disturbed neutral delay systems as in [24]. For these kinds of delayed systems, [25, Lemma 1] can be used to examine the stability of the associated nominal delayed systems, where three easily testable conditions are included. We also note that these conditions ensure that the considered systems are delay-independent stable. However, the delay-independent stability is not the general case. Despite this fact, since the case with $\tau = 0$ is exponentially stable, we readily derive that the system with an enough small time-delay is also exponentially stable, which ensure that the correspondingly disturbed equations are input-to-state stable provided that the delay is sufficiently small. In our future work, we will investigate these problems and systematically assess the effect of the introduced delay on the system stability as well as the convergence speed of tracking errors (as in the work [26]).

4. Numerical Simulation and Experimental Results

In this section, to demonstrate the effectiveness of the proposed scheme for robust motion synchronization, the numerical simulation results and experimental results of the attitude-trajectory consensus tracking of three 3-DOF helicopters which are labeled as H1 to H3 are presented.

Table 1: Nominal parameters of the helicopters ($i = 0, 1, 2, 3$).

Parameter	Value
K_{fi}	0.1188 N/V
l_{ai}	0.660 m
l_{hi}	0.178 m
m_i	0.094 kg
J_{ei}	1.034 kg·m^2
J_{pi}	0.045 kg·m^2
g	9.81 m/s^2

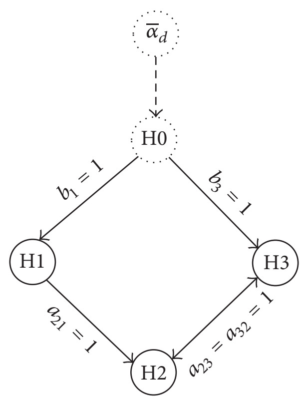

Figure 4: The considered communication topology.

Note that we focus on the analysis of the results of elevation-trajectory consensus tracking hereafter. The results of pitch channel are similar to that of elevation channel and hence omitted.

The nominal parameters of the four helicopters (including virtual helicopter H0) are the same, which are presented in Table 1. Their initial states are specified as follows:

$$\begin{aligned}(\alpha_0(0), \dot{\alpha}_0(0)) &= (-20.0\,\text{deg}, 0\,\text{deg/s}),\\ (\alpha_1(0), \dot{\alpha}_1(0)) &= (-21.5\,\text{deg}, 0\,\text{deg/s}),\\ (\alpha_2(0), \dot{\alpha}_2(0)) &= (-27.0\,\text{deg}, 0\,\text{deg/s}),\\ (\alpha_3(0), \dot{\alpha}_3(0)) &= (-16.9\,\text{deg}, 0\,\text{deg/s}).\end{aligned} \tag{31}$$

All the results are obtained on the directed communication graph shown in Figure 4. In this graph, helicopters 1 and 3 have access to desired trajectories $\alpha_d(t)$ which are the responses of H0 to desired signal $\overline{\alpha}_d(t)$, and Assumption 5 holds with $b_1 = b_3 = a_{21} = a_{23} = a_{32} = 1$ and all other entries of $\overline{B}$ and A_n being 0. Then,

$$L = \begin{bmatrix} 0 & 0 & 0 \\ -1 & 2 & -1 \\ 0 & -1 & 1 \end{bmatrix},$$

Table 2: Design parameters of the FTC estimators.

Parameter	Equation (7)	Equation (8)
λ_0	1.1	5
λ_1	1.5	8
λ_2	2	N/A
μ_0	3	8
μ_1	6	12
μ_2	8	N/A
$\overline{L}_{\rho d}$	1	N/A
$\overline{L}_e$	N/A	1

$$\overline{B} = \begin{bmatrix} 1 & 0 & 0 \\ 0 & 0 & 0 \\ 0 & 0 & 1 \end{bmatrix},$$
$$L + \overline{B} = \begin{bmatrix} 1 & 0 & 0 \\ -1 & 2 & -1 \\ 0 & -1 & 2 \end{bmatrix}. \tag{32}$$

Without loss of generality, the following nonstep desired trajectories provided to H0 are adopted for numerical simulations and experiments:

$$\begin{aligned}\overline{\alpha}_d(t) &= 10\sin(0.04\pi t) - 5,\\ \dot{\overline{\alpha}}_d(t) &= 0.4\pi\cos(0.04\pi t),\\ \ddot{\overline{\alpha}}_d(t) &= -0.016\pi^2\sin(0.04\pi t),\end{aligned} \tag{33}$$

where all the angles are given in degrees. For the parameters of control signal $u_{\alpha 0}$ which is determined by (6) with $b_0 = 1$, $a_{0j} = 0$, $j \in \mathcal{I}$, $\hat{\ddot{\alpha}}_d(t) = \ddot{\overline{\alpha}}_d(t)$, and $\hat{\dot{e}}_{\alpha 0}(t) = \dot{e}_{\alpha 0}(t)$, choose

$$\begin{aligned} k_{\alpha 0}^P &= 1.5,\\ k_{\beta 0}^D &= 2,\\ k_{\alpha 0}^I &= 0,\end{aligned} \tag{34}$$

where H0 is a virtual helicopter without the acting of LUDs; hence the integral term in the control law (6) is not adopted by H0 (i.e., $k_{\alpha 0}^I = 0$) for simplicity.

The design parameters chosen for the FTC estimators (7) and (8) are shown in Table 2. The initial state values of the differentiators in (7) and (8) are set to zero; that is, $\hat{\rho}_d(0) = \hat{\dot{\rho}}_d(0) = \hat{\ddot{\rho}}_d(0) = 0$ and $\hat{e}_{\rho i}(0) = \hat{\dot{e}}_{\rho i}(0) = 0$, $i \in \mathcal{I}$.

In the following, for comparison purposes, six cases (Cases 1–6) are considered. In each case, $u_{\alpha i}$ are determined by (6). In order to theoretically verify the results of Theorem 8, Cases 1–3 are designed for the numerical simulations. Specifically, to demonstrate that both tracking and synchronization performance without IC are not acceptable, IC is not adopted in Case 1; points (1)-(2) of Theorem 8 are verified by Case 2, where the helicopters with IC are subject to different constant disturbances; the helicopters with IC are subject to different time-varying disturbances in Case 3 to show the validity of points (1) and (3) of Theorem 8. The results of Theorem 8 are experimentally verified by Cases 4–6 on the experiment platform shown in Figure 1. IC is adopted in Cases 5-6 while, in Case 4, it is not. The ADSs of helicopters 2 and 3 are activated in Case 6 while in Cases 4-5 are not. Note that, since the disturbances are unknown in the experiments, the control parameters of $u_{\alpha i}$ in experiments are not the same as those in numerical simulations, where the disturbances are specified and used to choose the control parameters.

The detailed differences among Cases 1–6 are as follows:

(1) For Case 1, the numerical example with constant disturbance ($d_{\alpha 1} = 5\,\text{deg/s}^2$, $d_{\alpha 2} = 10\,\text{deg/s}^2$, $d_{\alpha 3} = 15\,\text{deg/s}^2$, $\dot{d}_{\alpha i} = 0$, $i = 1, 2, 3$) is simulated. The parameters of $u_{\alpha i}$ are chosen as $k_{\alpha i}^P = 3.2$, $k_{\alpha i}^D = 1.3$, $k_{\alpha i}^I = 0$ $(i = 1, 2, 3)$, which corresponds to the situation without IC.

(2) Case 2 is the same as Case 1, except for $k_{\alpha i}^I = 1$ $(i = 1, 2, 3)$. That is, IC is applied for the numerical example with constant disturbance.

(3) Case 3 is the same as Case 2, except for time-varying $d_{\alpha i}$ that are given as follows:

$$d_{\alpha i} = 5\sin(0.05 i\pi t) + 5i\left(\text{deg/s}^2\right), \quad i = 1, 2, 3. \tag{35}$$

Note the three points: (a) as shown in (35), the three helicopters are subject to different disturbances; (b) initial disturbances $d_{\alpha i}(0) = 5i\,\text{deg/s}^2$, $i = 1, 2, 3$; (c) to verify the results of Theorem 8, the disturbances used in Case 2 satisfy conditions $\lim_{t\to+\infty}\dot{d}_{\alpha i} = 0$ for each $i = 1, 2, 3$, while those used in Case 3 do not.

(4) For Case 4, $u_{\alpha i}$ without IC are applied to the experiment platform shown in Figure 1. The parameters of $u_{\alpha i}$ are chosen as $k_{\alpha i}^P = 5$, $k_{\alpha i}^D = 8$, $k_{\alpha i}^I = 0$ $(i = 1, 2, 3)$.

(5) Case 5 is the same as Case 4, except for $k_{\alpha i}^I = 3$ $(i = 1, 2, 3)$. That is, IC is applied to the experiment platform.

(6) For Case 6, in the experiments, the ADSs of helicopters 2 and 3 are activated and the same control laws as for Case 5 are applied.

It is worthwhile noting that ADS has a dramatic effect on the motion of helicopter body, whether it is static or moving. This point is easily seen from the mechanical structure of helicopter as shown in Figure 2 and is also verified by the following experiments.

4.1. Case 1: Numerical Simulation without Using IC. The numerical simulation results for this case are presented in Figure 5. As shown in subfigures (a) and (b) therein, because IC is not adopted in control design to attenuate constant disturbances, neither tracking error nor synchronization error converges to a small neighborhood of zero. More specifically,

(1) for the elevation axis, the magnitude of tracking error (of each helicopter) is greater than 5.5 deg when $t \geq 20$ sec and is steady as t increases. The synchronization error between any pair of the three helicopters is of a magnitude greater than 1 deg when $t \geq 20$ sec and is steady as t increases. The reason is that the constant disturbance of the helicopter is different from each other and is not attenuated by IC.

(2) as shown in subfigures (c) and (d) of Figure 5, the voltage applied to either front motor or back motor, with a value equal to the maximum acceptable voltage 24 V at the beginning ($t \leq 0.8$ sec), has a magnitude smaller than 24 V for all $t > 0.8$ sec (smaller than 3 V for all $t > 2$ sec).

(3) as shown in subfigures (e) and (f), the attained accuracies of the FTC estimators are $|\ddot{\alpha}_d - \hat{\ddot{\alpha}}_d| \leq 0.0074\,\text{deg/s}^2$ and $\max_{1\leq i\leq 3}|\dot{e}_{\alpha i} - \hat{\dot{e}}_{\alpha i}| \leq 0.003\,\text{deg/s}$ that corresponds to Lemma 2 for FTC estimators (7) and (8) with finite time t_c (in this case, $t_c \leq 7$ sec and $\max_{1\leq i\leq 3}t_{ci} \leq 2.5$ sec for (7) and (8), resp.).

4.2. Case 2: Numerical Simulation with Using IC for Constant Disturbances. In this case, IC is adopted in control design to attenuate constant disturbances. The corresponding simulation results are presented in Figure 6, demonstrating that both tracking and synchronization performance are dramatically improved, compared with that achieved in Case 1. A detailed analysis of the results is given as follows:

(1) For the elevation axis, when $t \geq 20$ sec, the magnitude of tracking error (of each helicopter) is smaller than 0.03 deg and the synchronization error between any two helicopters has a magnitude smaller than 0.01 deg. Points (1) and (2) of Theorem 8 are verified by these results.

(2) The voltage applied to either front motor or back motor, with a value equal to the maximum acceptable voltage 24 V at the beginning ($t \leq 0.8$ sec), is of a magnitude less than 3 V for all $t > 2$ sec.

(3) The result of FTC estimator (7) is the same as that in Case 1 and hence omitted. The attained accuracies of FTC estimator (8) are $\max_{1\leq i\leq 3}|\dot{e}_{\alpha i} - \hat{\dot{e}}_{\alpha i}| \leq 0.009\,\text{deg/s}$ and the finite convergence time satisfies $\max_{1\leq i\leq 3}t_{ci} \leq 15$ sec.

4.3. Case 3: Numerical Simulation with Using IC for Time-Varying Disturbances. In this case, IC is adopted in control design to attenuate time-varying disturbances. The corresponding simulation results are presented in Figure 7. Although subject to the time-varying disturbances shown in (35), both tracking and synchronization performance are improved compared with that achieved in Case 1, where the disturbances are constants. However, compared with that achieved in Case 2, where the disturbances are constants and also attenuated by IC, both tracking and synchronization performance are degraded observably. A detailed analysis of the results is given as follows:

(1) For the elevation axis, when $t \geq 20$ sec, the magnitude of tracking error (of each helicopter) is smaller than 1.0 deg; that is,

$$\left|\tilde{\alpha}_i(t)\right| < 1.0\,\text{deg}, \quad \forall t > 20\,\text{sec}, \; i = 1, 2, 3, \tag{36}$$

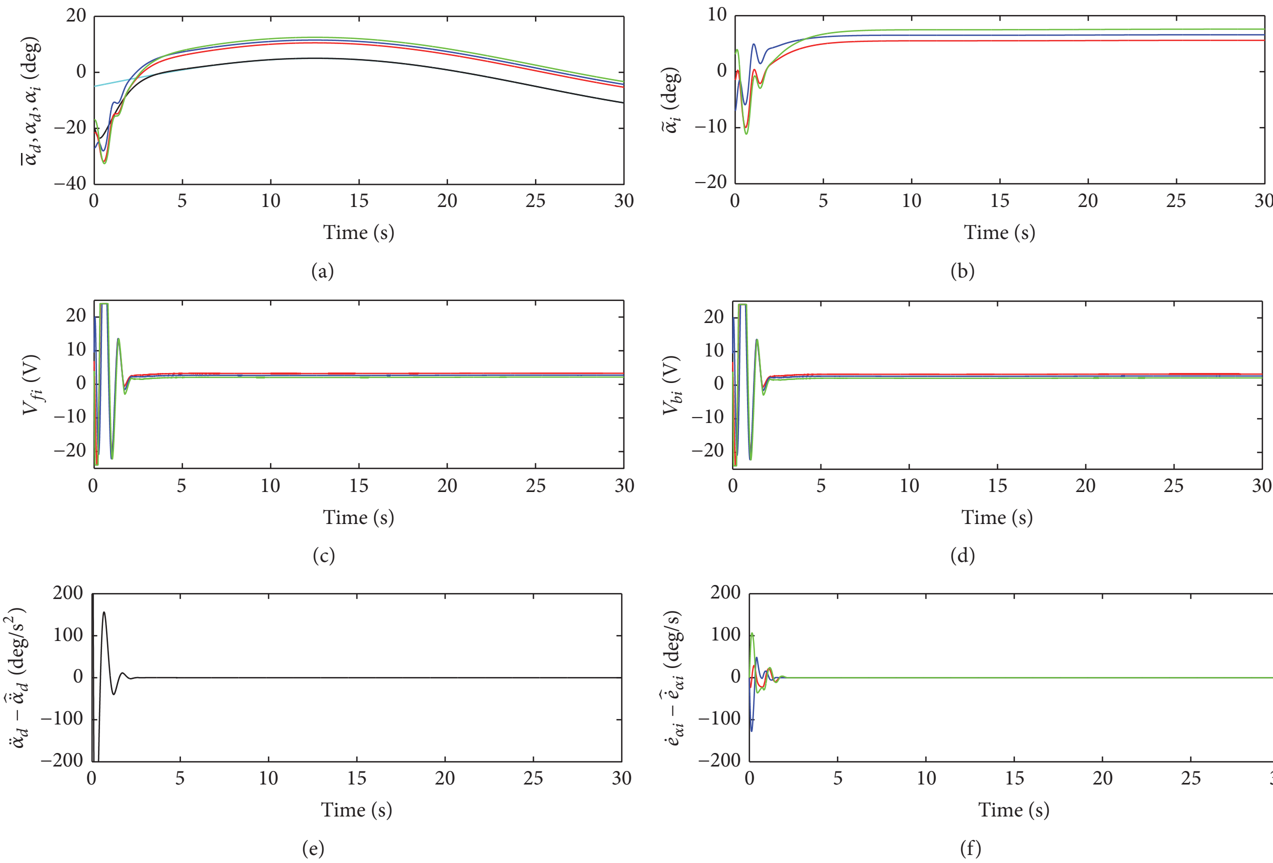

FIGURE 5: Numerical simulations results for Case 1 ($\overline{\alpha}_d$-cyan, H0-black, H1-red, H2-blue, and H3-green): (a) elevation angular position trajectory, (b) elevation angle tracking error, (c) voltage of the front motor, (d) voltage of the back motor, (e) estimation error of the elevation angular acceleration of H0, and (f) estimation errors of the first-order derivative of LNSE of H1–H3.

and the synchronization error between any two helicopters has a magnitude smaller than 1.51 deg.

With parameters $k^P_{\alpha i} = 3.2$, $k^D_{\alpha i} = 1.3$, $k^I_{\alpha i} = 1$ ($i = 1, 2, 3$) and (21), the following matrix $P_{\alpha i}$ can be obtained by resolving the Lyapunov equations (28):

$$P_{\alpha i} = \begin{bmatrix} 2.23 & 1.52 & 0.50 \\ 1.52 & 3.10 & 0.63 \\ 0.50 & 0.63 & 0.87 \end{bmatrix},$$
$$\lambda_{\max}(P_{\alpha i}) = 4.43,$$
$$\lambda_{\min}(P_{\alpha i}) = 0.68. \tag{37}$$

With (4) and (35), we have $\overline{d}_{d\alpha} = 0.041\ \mathrm{deg/s^3}$; then, along with (32) and (37), we get b_α in (27) that satisfies $b_\alpha \le 6.41$ deg and the ultimate bound of the tracking errors in (26) satisfies $\|\tilde{\boldsymbol{\alpha}}(t)\|_2 \le 9.16$ deg. Then, points (1) and (3) of Theorem 8 are verified by (36).

(2) The voltage applied to either front motor or back motor, with a value equal to the maximum acceptable voltage 24 V at the beginning ($t \le 0.8$ sec), is of a magnitude less than 3.8 V for all $t > 2$ sec.

(3) The result of the FTC estimators is the same as that in Case 2 and hence omitted here.

4.4. Case 4: Experiment without Using IC. The experimental results for this case are presented in Figure 8. It is seen that the tracking error (of each helicopter) does not converge to a small neighborhood of zero and the synchronization performance is better than tracking performance. A detailed analysis of the results is given as follows:

(1) For the elevation axis, the magnitude of tracking error (of each helicopter) is greater than 3 deg for all $t > 10$ sec; the synchronization error (between any two helicopters) is $|\alpha_1 - \alpha_2| \le 1.11$ deg, $|\alpha_1 - \alpha_3| \le 0.76$ deg, and $|\alpha_2 - \alpha_3| \le 0.69$ deg for all $t > 10$ sec; the synchronization error between H2 and H3 has a smaller magnitude than that between H1 and H2 (or H1 and H3), which is an immediate consequence of the fact that H2 and H3 can obtain information from each other and both of them are equipped with ADSs, whereas H1 is not.

(2) The voltage applied to either the front or back motor, with a value equal to the maximum acceptable voltage 24 V at the beginning ($t \le 6$ sec), has a magnitude smaller than 21 V for all $t > 6$ sec.

4.5. Case 5: Experiment with Using IC. The experimental results for this case are presented in Figure 9. It is observed

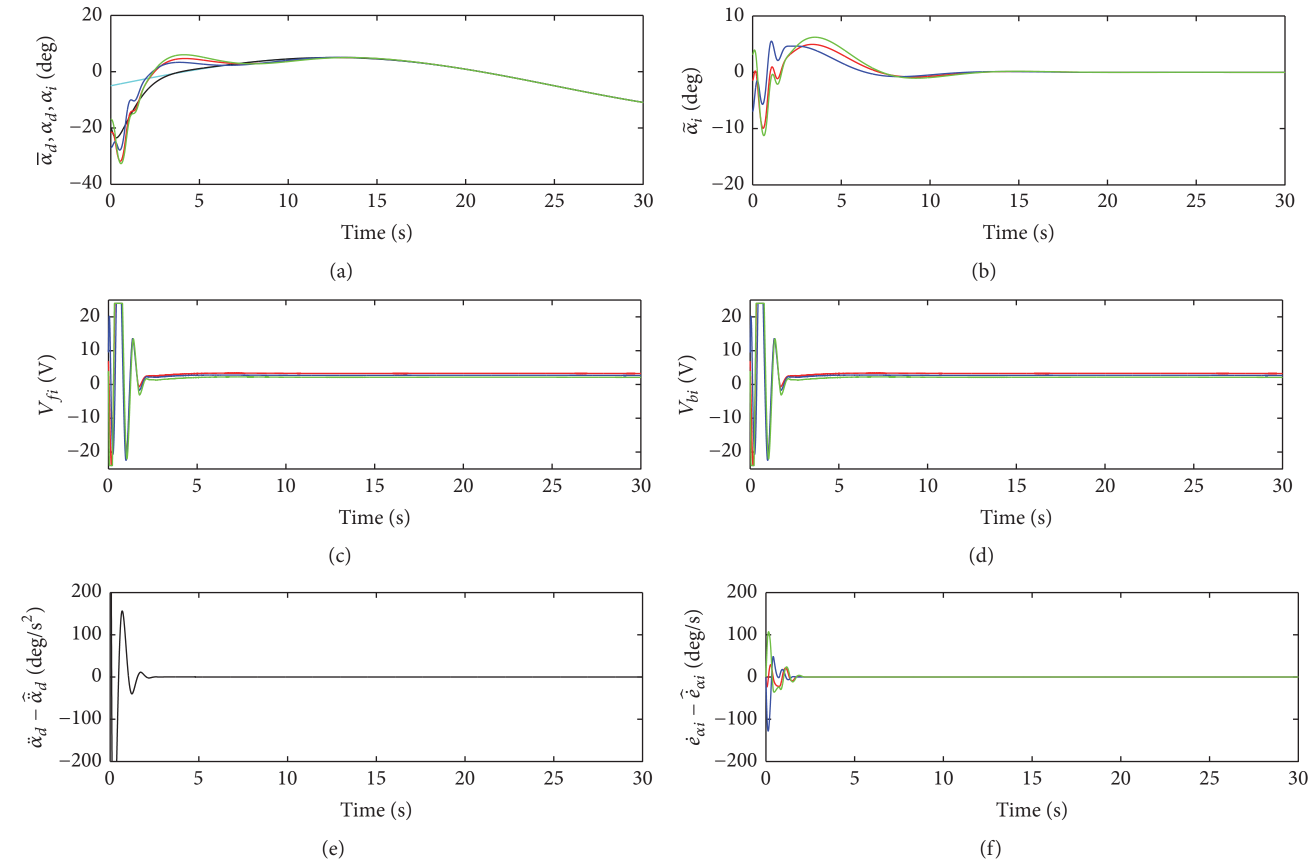

Figure 6: Numerical simulation results for Case 2 ($\overline{\alpha}_d$-cyan, H0-black, H1-red, H2-blue, and H3-green): (a) elevation angular position trajectory, (b) elevation angle tracking error, (c) voltage of the front motor, (d) voltage of the back motor, (e) estimation error of the elevation angular acceleration of H0, and (f) estimation errors of the first-order derivative of LNSE of H1–H3.

that, compared with Case 4, both tracking and synchronization performance are improved because the disturbances are attenuated by IC in this case. More specifically,

(1) for the elevation axis, the magnitude of tracking error (of each helicopter) is smaller than 1.02 deg for all $t > 10$ sec ($\tilde{\alpha}_1 = 1.01$ deg, $\tilde{\alpha}_2 = 0.78$ deg, and $\tilde{\alpha}_3 = 0.66$ deg); the synchronization error (between any two helicopters) is $|\alpha_1 - \alpha_2| \le 0.58$ deg, $|\alpha_1 - \alpha_3| \le 0.67$ deg, and $|\alpha_2 - \alpha_3| \le 0.45$ deg for all $t > 10$ sec;

(2) the voltage applied to either the front or back motor, with a value equal to the maximum acceptable voltage 24 V at the beginning ($t \le 5$ sec), has a magnitude smaller than 22 V for all $t > 5$ sec.

4.6. Case 6: With Activated ADS and the Same Controller as for Case 5. The ADSs equipped on helicopters 2 and 3 are activated in this case, whose dynamic positions along the arms of helicopters are shown in Figure 10, with the same initial position −0.14 m (−0.14 m is the farthest possible position from propellers). This is different from the previous Case 4 and Case 5 where they are both fixed at −0.14 m. The experimental results for this case are presented in Figure 11. It is seen that motion of ADSs does not lead to dramatic performance degradation in the steady state of tracking and synchronization errors, compared with the performance achieved in Case 5. A detailed comparative analysis of the results is given as follows:

(1) For the elevation axis, the ultimate bound of either tracking error or synchronization error is nearly the same with that achieved in Case 5; the transient performance is degraded a little (this degradation is relatively obvious for helicopter 2 because the effect of the moving ADS on helicopter 4 is delivered to helicopter 2 which has no access to the desired trajectory as shown in Figure 4).

(2) The voltage applied to either the front or back motor, with a value equal to the maximum acceptable voltage 24 V at the beginning ($t \le 6$ sec), has a magnitude smaller than 23.5 V for all $t > 5$ sec.

To demonstrate the different steady-state tracking performance clearly, the maximum magnitudes of tracking errors that appeared in each case during time interval $t \in [20, 30]$ are shown in Table 3 (Cases 1–3) and Table 4 (Cases 4–6). As shown in these tables, the tracking accuracy is improved in numerical simulations and experiments by IC.

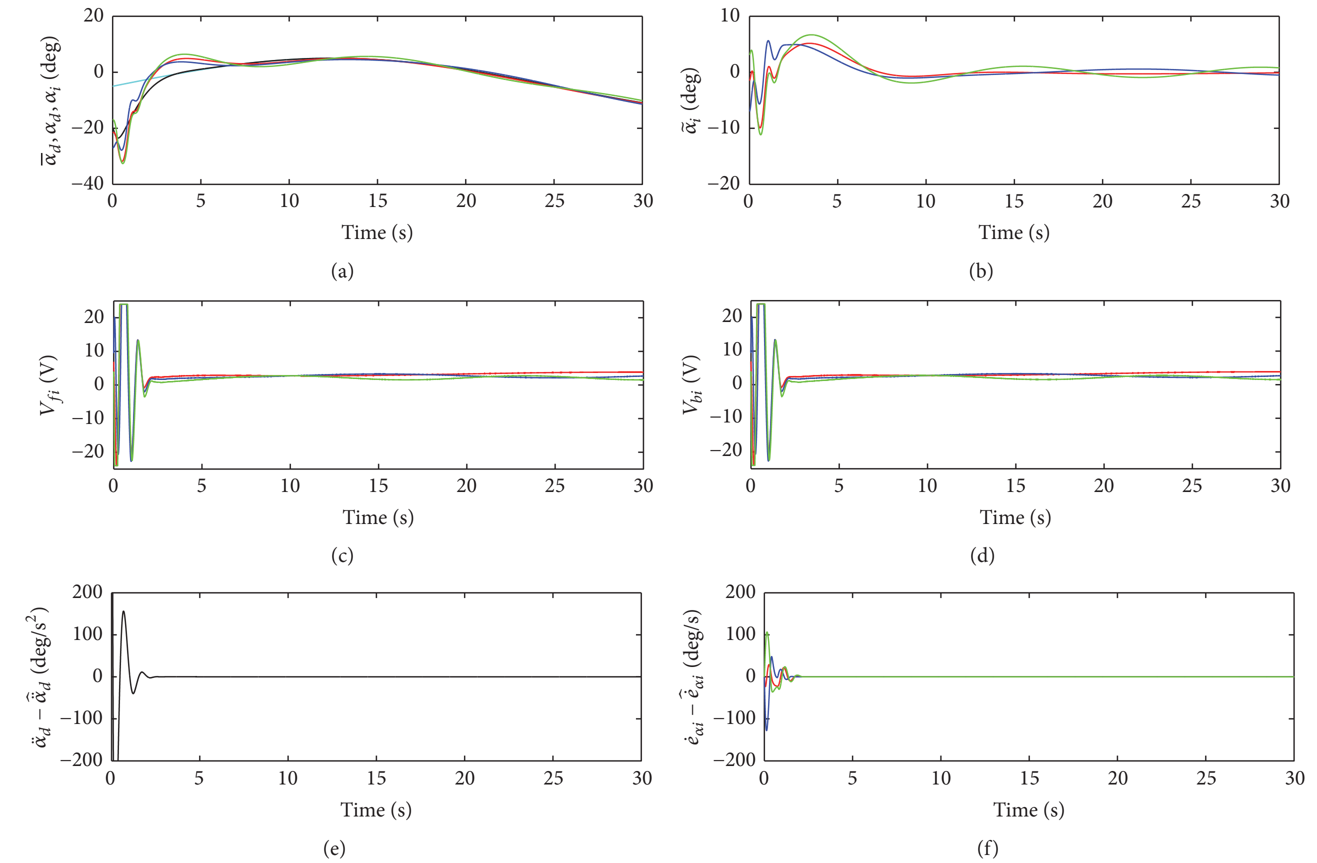

FIGURE 7: Numerical simulation results for Case 3 ($\overline{\alpha}_d$-cyan, H0-black, H1-red, H2-blue, and H3-green): (a) elevation angular position trajectory, (b) elevation angle tracking error, (c) voltage of the front motor, (d) voltage of the back motor, (e) estimation error of the elevation angular acceleration of H0, and (f) estimation errors of the first-order derivative of LNSE of H1–H3.

TABLE 3: Maximum magnitudes of $\tilde{\alpha}_i$, $i = 1, 2, 3$, in simulations for $t > 20$ s (deg).

Case	H1	H2	H3
1	5.58	6.59	7.59
2	0.027	0.027	0.027
3	0.28	0.62	0.95

TABLE 4: Maximum magnitudes of $\tilde{\alpha}_i$, $i = 1, 2, 3$, in experiments for $t > 20$ s (deg).

Case	H1	H2	H3
4	2.99	3.40	3.12
5	1.0	0.78	0.66
6	0.89	0.69	0.94

5. Concluding Remarks

The robust distributed consensus tracking controllers with integral action for multiple 3-DOF experimental helicopters without velocity measurements have been studied under the condition that only the desired angular position measurements are accessible to a small subset of the helicopters. Motivated by the effectiveness of the tracking controller with integral action in disturbances rejection for the single vehicle, the distributed controllers have been proposed by combining FTC estimators with distributed integral controllers. With using the FTC estimators, great accuracy and finite-time convergence have been achieved for the estimation of the lacking information. Meanwhile, the distributed controllers with integral action stabilized the tracking errors and rejected the input disturbances. Through analysing the closed-loop stability, the conditions ensuring zero-error tracking and the ultimate bound of errors for the general cases with nonzero error have been derived. It has been verified through the results of numerical simulations and experiments on platform of "three 3-DOF helicopters" that the tracking and synchronization accuracy have been improved by the proposed controllers with proper parameters.

Future work will focus on the design and experimental verification of bounded distributed controller for the platform under the directed communication graph with time-delay. The control parameters in (6) also need to be optimized to get the minimized ultimate bound of tracking errors.

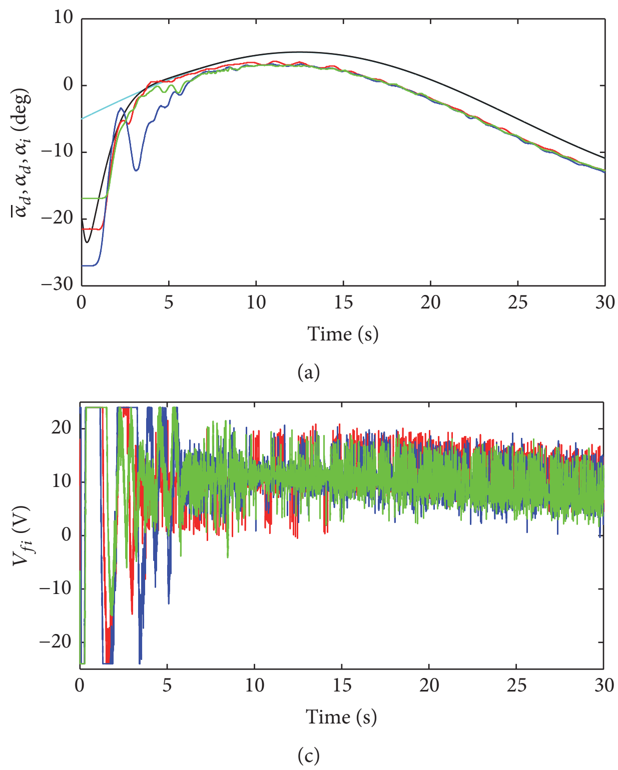

FIGURE 8: Experimental results for Case 4 ($\bar{\alpha}_d$-cyan, H0-black, H1-red, H2-blue, and H3-green): (a) elevation angular position trajectory, (b) elevation angle tracking error, (c) voltage of the front motor, and (d) voltage of the back motor.

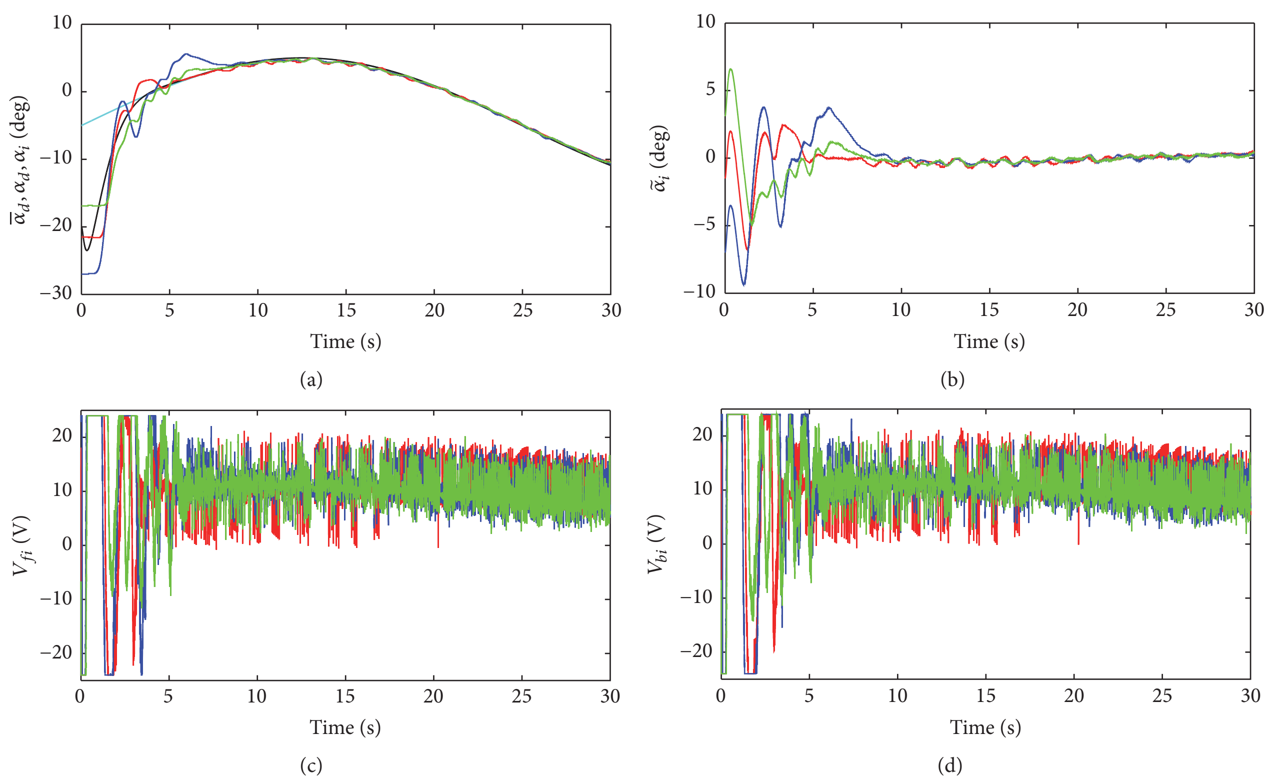

FIGURE 9: Experimental results for Case 5 ($\bar{\alpha}_d$-cyan, H0-black, H1-red, H2-blue, and H3-green): (a) elevation angular position trajectory, (b) elevation angle tracking error, (c) voltage of the front motor, and (d) voltage of the back motor.

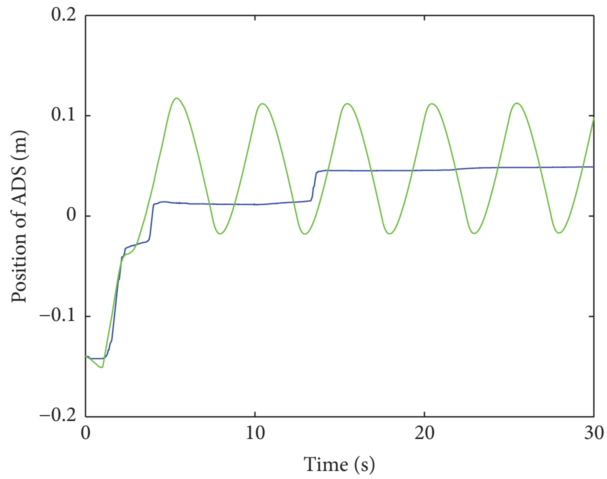

Figure 10: Positions of ADSs on helicopters 2 and 3: helicopter 2 (blue) and helicopter 3 (green).

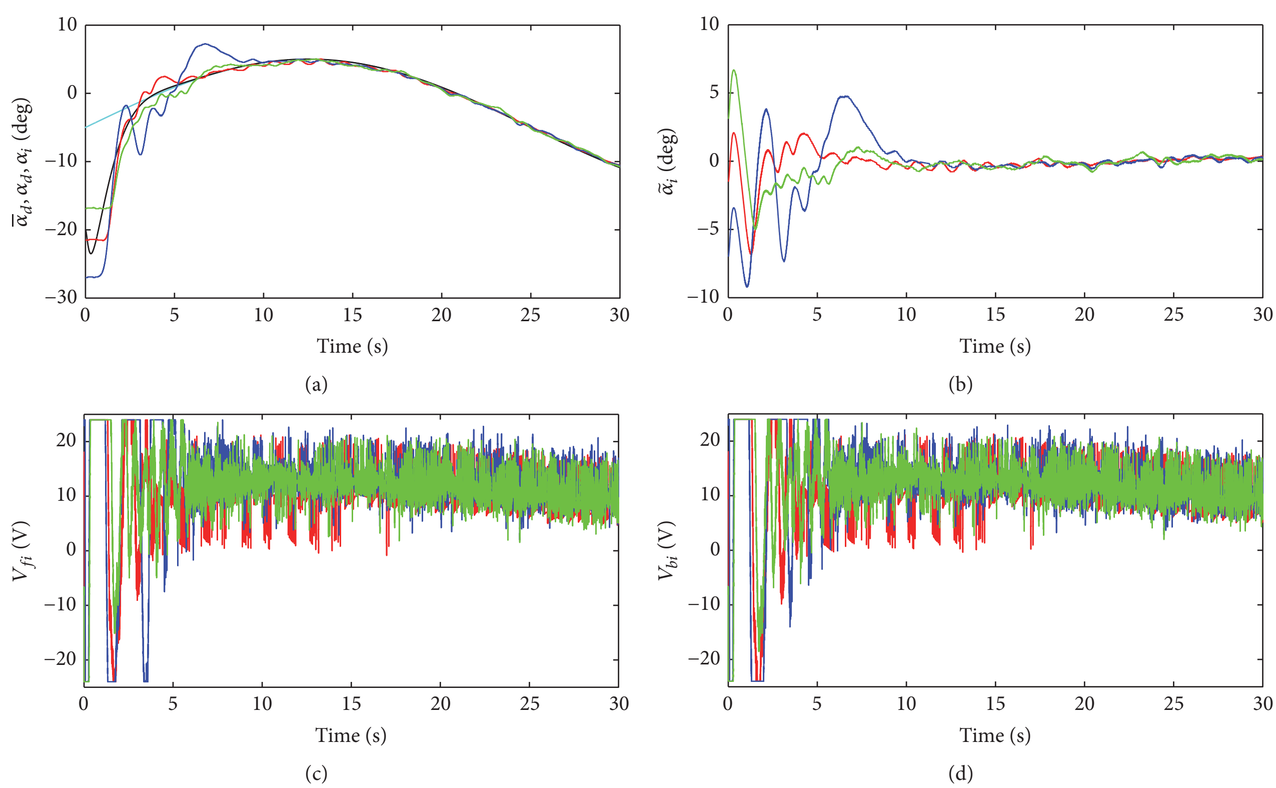

Figure 11: Experimental results for Case 6 ($\overline{\alpha}_d$-cyan, H0-black, H1-red, H2-blue, and H3-green): (a) elevation angular position trajectory, (b) elevation angle tracking error, (c) voltage of the front motor, and (d) voltage of the back motor.

Appendix

A useful lemma used to show boundedness and ultimate bound of the solutions of some disturbed state equations is given as follows.

Lemma A.1 (see [5, Lemma 2]). *Consider state solution $x(t)$ of the linear time-invariant equation:*

$$\dot{x} = Ax + Bu, \tag{A.1}$$

where $x \in R^m$ is the state, $u \in R$ is the continuously differentiable input, and matrices $A \in R^{m\times m}$ and $B \in R^{m\times 1}$. If A is Hurwitz, then

(1) *system (A.1) is globally input-to-state stable (GISS); that is, if u is bounded for all t, then $x(t)$ with any initial state $x(t_0)$ is also bounded for all t;*

(2) *there exist class $\mathscr{K}\mathscr{I}$ function γ and time $T \geq 0$ (dependent on $x(t_0)$ and $\|u\|_{\mathscr{L}_\infty} =: \sup_{t\geq 0}|u(t)| < \infty$) such that $x(t)$ with any $x(t_0)$ satisfies*

$$\|x(t)\|_2 \leq \gamma\left(\|x(0)\|_2, t\right), \quad \forall t_0 \leq t \leq t_0 + T,$$
$$\|x(t)\|_2 \leq \frac{2\lambda_{max}(P)\|B\|_2\|u\|_{\mathscr{L}_\infty}}{\theta}\sqrt{\frac{\lambda_{max}(P)}{\lambda_{min}(P)}}, \quad \forall t \geq t_0 + T, \tag{A.2}$$

where $0 < \theta < 1$, $\lambda_{max}(P)$, and $\lambda_{min}(P)$ are the maximum and minimum eigenvalues of the symmetric positive-definite matrix $P \in R^{m\times m}$ which is the solution of the Lyapunov equation:

$$PA + A^T P = -I_m. \tag{A.3}$$

Notations

α_i, β_i: The elevation angle and pitch angle, respectively (rad)

$\dot{\alpha}_i$, $\dot{\beta}_i$: The elevation angle rate and pitch angle rate, respectively (rad/s)

J_{ei}, J_{pi}: The moments of inertia about elevation axis and pitch axis, respectively (kg·m^2)

K_{fi}: The force constant of motor-propeller combination (N/V)

l_{ai}: The distance from travel axis and elevation axis to the center of helicopter body (m)

l_{hi}: The distance from pitch axis to either motor (m)

m_i: The effective mass of helicopter body (kg)

g: The gravitational acceleration constant, (9.81 m/s^2)

$f_{\alpha i}$, $f_{\beta i}$: The lumped uncertainties and disturbances (LUDs) acting on elevation and pitch channels, respectively (N·m)

V_{fi}, V_{bi}: The voltages applied to the front motor and back motor, respectively; the voltage limit for the motors is 24 V (i.e., $|V_{fi}| \leq 24$ V, $|V_{bi}| \leq 24$ V) (V)

V_{si}, V_{di}: The sum and the difference of V_{fi} and V_{bi}, respectively (V).

Competing Interests

The authors declare that they have no competing interests.

Acknowledgments

This work is supported by the National Natural Science Foundation of China under Grants nos. 61304016 and 61305132, the Fundamental Research Funds for the Central Universities under Grant no. ZYGX2016KYQD102. The authors would like to thank Professor Hugh. T. Liu at UTIAS for generously providing the 3-DOF helicopter platform at FSC lab to verify the controllers developed in this paper.

References

[1] S. Khoo, L. Xie, and Z. Man, "Robust finite-time consensus tracking algorithm for multirobot systems," *IEEE/ASME Transactions on Mechatronics*, vol. 14, no. 2, pp. 219–228, 2009.

[2] W. Zhang, Z. Wang, and Y. Guo, "Robust consensus for uncertain multi-agent systems on directed communication topologies," in *Proceedings of the 49th IEEE Conference on Decision and Control (CDC '10)*, pp. 6317–6322, Atlanta, Ga, USA, December 2010.

[3] G. Hu, "Robust consensus tracking of a class of second-order multi-agent dynamic systems," *Systems & Control Letters*, vol. 61, no. 1, pp. 134–142, 2012.

[4] C. Zhang, H. Wu, J. He, and C. Xu, "Consensus tracking for multi-motor system via observer based variable structure approach," *Journal of the Franklin Institute. Engineering and Applied Mathematics*, vol. 352, no. 8, pp. 3366–3377, 2015.

[5] B. Zhu, H. H.-T. Liu, and Z. Li, "Robust distributed attitude synchronization of multiple three-DOF experimental helicopters," *Control Engineering Practice*, vol. 36, pp. 87–99, 2015.

[6] B. Zhu, Z. Li, H. H.-T. Liu, and H. Gao, "Robust second-order tracking of multi-vehicle systems without velocity measurements on directed communication topologies," in *Proceedings of the American Control Conference (ACC '14)*, pp. 5414–5419, IEEE, Portland, Ore, USA, June 2014.

[7] B. Zhu, C. Meng, and G. Hu, "Robust consensus tracking of double-integrator dynamics by bounded distributed control," *International Journal of Robust and Nonlinear Control*, vol. 26, no. 7, pp. 1489–1511, 2016.

[8] A. Das and F. L. Lewis, "Distributed adaptive control for synchronization of unknown nonlinear networked systems," *Automatica*, vol. 46, no. 12, pp. 2014–2021, 2010.

[9] Y. Su and J. Huang, "Cooperative output regulation with application to multi-agent consensus under switching network," *IEEE Transactions on Systems, Man, and Cybernetics Part B: Cybernetics*, vol. 42, no. 3, pp. 864–875, 2012.

[10] M. Andreasson, D. V. Dimarogonas, H. Sandberg, and K. H. Johansson, "Distributed control of networked dynamical systems: static feedback, integral action and consensus," *IEEE Transactions on Automatic Control*, vol. 59, no. 7, pp. 1750–1764, 2014.

[11] B. Zhu, "On overshoot and integrators," *IET Control Theory & Applications*, vol. 8, no. 8, pp. 633–640, 2014.

[12] A. N. Gündeş and E. C. Wai, "Low order integral-action controller synthesis," *Systems & Control Letters*, vol. 60, no. 11, pp. 885–891, 2011.

[13] A. Levant, "Higher-order sliding modes, differentiation and output-feedback control," *International Journal of Control*, vol. 76, no. 9-10, pp. 924–941, 2003.

[14] A. Levant, "Non-homogeneous finite-time-convergent differentiator," in *Proceedings of the 48th IEEE Conference on Decision and Control*, pp. 8399–8404, Shanghai, China, December 2009.

[15] J. Shan, H.-T. Liu, and S. Nowotny, "Synchronised trajectory-tracking control of multiple 3-DOF experimental helicopters,"

IEE Proceedings—Control Theory and Applications, vol. 152, no. 6, pp. 683–692, 2005.

[16] *3DOF Helicopter System, Product Information*, Quanser Inc., Markham, Canada, 2002, http://www.quanser.com.

[17] A. T. Kutay, A. J. Calise, M. Idan, and N. Hovakimyan, "Experimental results on adaptive output feedback control using a laboratory model helicopter," *IEEE Transactions on Control Systems Technology*, vol. 13, no. 2, pp. 196–202, 2005.

[18] T. Kiefer, K. Graichen, and A. Kugi, "Trajectory tracking of a 3DOF laboratory helicopter under input and state constraints," *IEEE Transactions on Control Systems Technology*, vol. 18, no. 4, pp. 944–952, 2010.

[19] H. Ríos, A. Rosales, A. Ferreira, and A. Dávila, "Robust regulation for a 3-DOF helicopter via sliding-modes control and observation techniques," in *Proceedings of the American Control Conference (ACC '10)*, pp. 4427–4432, Baltimore, Md, USA, July 2010.

[20] A. F. de Loza, H. Ríos, and A. Rosales, "Robust regulation for a 3-DOF helicopter via sliding-mode observation and identification," *Journal of the Franklin Institute*, vol. 349, no. 2, pp. 700–718, 2012.

[21] H. Liu, G. Lu, and Y. Zhong, "Robust LQR attitude control of a 3-DOF laboratory helicopter for aggressive maneuvers," *IEEE Transactions on Industrial Electronics*, vol. 60, no. 10, pp. 4627–4636, 2013.

[22] Z. Li, Z. Duan, G. Chen, and L. Huang, "Consensus of multiagent systems and synchronization of complex networks: a unified viewpoint," *IEEE Transactions on Circuits and Systems I: Regular Papers*, vol. 57, no. 1, pp. 213–224, 2010.

[23] W. Ren and Y. Cao, "Distributed coordination of multi-agent networks," in *Communications and Control Engineering: Emergent Problems, Models, and Issues*, Springer, Berlin, Germany, 2011.

[24] P. Pepe and I. Karafyllis, "Converse Lyapunov-Krasovskii theorems for systems described by neutral functional differential equations in Hale's form," *International Journal of Control*, vol. 86, no. 2, pp. 232–243, 2013.

[25] P. Wei, Q. Guan, W. Yu, and L. Wang, "Easily testable necessary and sufficient algebraic criteria for delay-independent stability of a class of neutral differential systems," *Systems and Control Letters*, vol. 57, no. 2, pp. 165–174, 2008.

[26] S. Liu, L. Xie, and F. L. Lewis, "Synchronization of multiagent systems with delayed control input information from neighbors," *Automatica*, vol. 47, no. 10, pp. 2152–2164, 2011.

Hindawi Publishing Corporation
Mathematical Problems in Engineering
Volume 2016, Article ID 2630790, 11 pages
http://dx.doi.org/10.1155/2016/2630790

Research Article

Combat Network Synchronization of UCAV Formation Based on RTBA Model

Chengwei Ruan, Haiyan Yang, Lei Yu, and Yingxin Kou

Aeronautics and Astronautics Engineering College, Air Force Engineering University, Xi'an 710038, China

Correspondence should be addressed to Haiyan Yang; yanghy07@yeah.net

Received 16 July 2016; Accepted 5 September 2016

Academic Editor: Zhao Cheng

The paper aims at developing an efficient method to acquire a proper UCAV formation structure with robust and synchronized features. Here we introduce the RTBA (Route Temporary Blindness Avoidance) model to keep the structure stable and the HPSO (hybrid particle swarm optimization) method is given to find an optimal synchronized formation. The major contributions include the following: (1) setting up the dynamic hierarchy topologic structure of UCAV formation; (2) the RTB phenomenon is described and the RTBA model is put forward; (3) the node choosing rules are used to keep the invulnerability of the formation and the detective information quantifying method is given to measure the effectiveness of the connected nodes; and (4) the hybrid particle swarm optimization method is given to find an optimal synchronized topologic structure. According to the related principles and models, the simulations are given in the end, and the results show that the simplification of the model is available in engineering, and the RTBA model is useful to solve the real problems in combat in some degree.

1. Introduction

Since the control theory and intelligent technology have acquired significant advances, research on multiple unmanned combat aerial vehicles (UCAVs) has attracted more and more attentions in recent years. The cooperative problems [1], control command problems [2–4], mission assignment problems [5–7], and route planning problems [8, 9] have become the focus among researchers. The structure of UCAV formation has also been focused on in recent years. The frequent exchanging information among different UCAVs during the mission process needs a robust and efficient structure to keep the systems up. A robust status needs an adaptive structure both in physical level and in functional level and an efficient job among UCAVs needs a consistent recognition towards the same combat situation.

Many researches concerned about the UCAV formation have assumed that all the UCAV units had their information completely shared, and the communication interruptions from both the enemies and the measurement errors are neglected, such as [10, 11]. But, in real combat, the UCAV units can only get limited information about the situation due to the limitations of current communicating abilities. Just a few references have described the UCAV model with a local knowledge mastered by the combat units. Reference [12] has designed a new distributed auction algorithm based on the neighbor knowledge. Reference [13] puts forward a cooperative missile guiding rule based on the local communication and the features of heterogeneous structure. Reference [14] gives a new distributed auction algorithm with a limited communication ability. Though these researches have brought us many valuable results which may be useful to solve some problems in real society, the researches on topology structure and the dynamic model still need to be analyzed.

Route Temporary Blindness (RTB) problem [15] which may lead to communication interruption may also be very important to have an effect on the robustness of the UCAV formation. The communication among UCAVs during the continuous mission executing process may lead to RTB problem, and the RTB problem may force the formation to upgrade its structure. In order to get an optimal UCAV formation, we put forward a method in this study to solve the RTB problem and get an optimal structure with efficient synchronized features.

The paper is organized as follows: Section 1 is introduction. Section 2 presents the dynamic topology model of

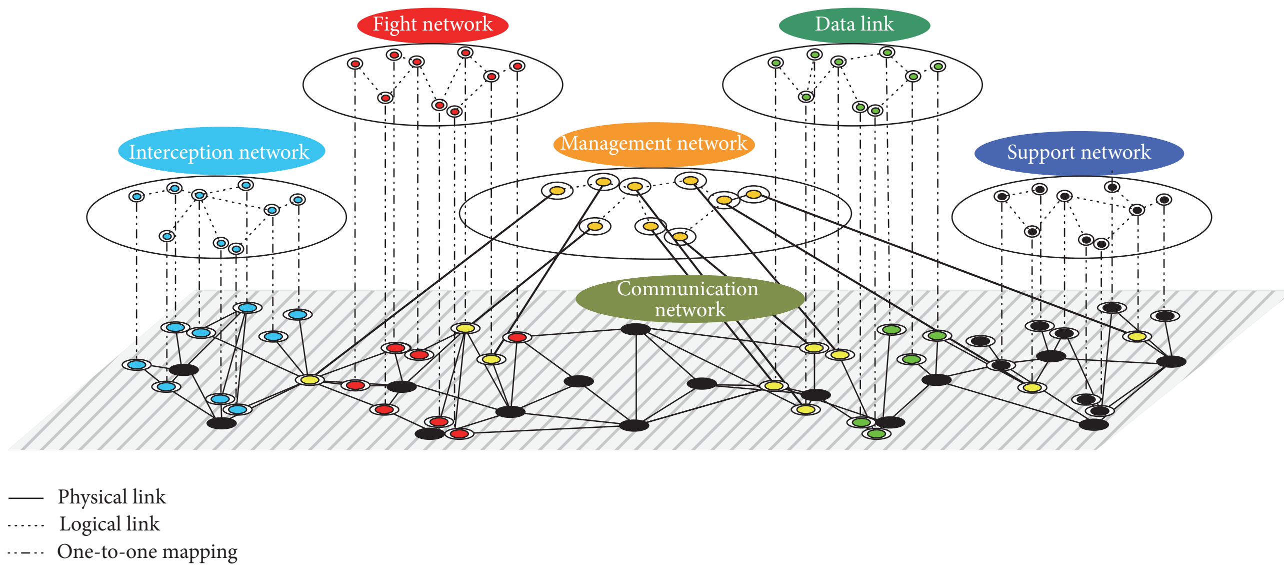

FIGURE 1: Relationships between physical and functional nodes in UCAV formation.

UCAV formation and its node survival model. Section 3 describes the rout blindness problem and its solution. Section 4 puts forward an optimal algorithm aiming at finding a better structure with a more stable and synchronized features. Section 5 gives the simulation results and Section 6 is conclusion.

2. Dynamic Topology Modeling of UCAV Net Constructing

In order to solve the cooperative problems in UCAV cooperation, we need to better understand the structure of the UCAV formation both in physical and in functional levels. The structure of UCAV formation can be described as $\mathbf{G} = (\mathbf{P}, \mathbf{F})$, $\mathbf{P}$ is the variable set of physical structure which can be described as $\mathbf{P} = (\mathbf{V}, \mathbf{E}, \mathbf{C})$, $\mathbf{V}$ is the set of UCAV nodes, and $\mathbf{E}$ means the connections between different nodes. Each edge $e_i \in \mathbf{E}$ can find two relative nodes (v_j, v_k) in $\mathbf{V}$. $\mathbf{C}$ is the feature set of UCAV formation, $C_n(k) \in \mathbf{C}$ $(n = 1, 2, \ldots, n_{\max};\ k = 1, 2, \ldots, k_{\max})$, $n_{\max}$ is the maximum number of UCAVs, and $k_{\max}$ is the maximum number of the kinds of UCAV features. $\mathbf{F}$ is the variable set of functional structures which is constructed as $\mathbf{F} = (\mathbf{M}, \mathbf{R})$, $\mathbf{M}$ is the number of kinds of different missions, and $\mathbf{R}$ represents a set of logic relationships between different functional nodes.

2.1. Physical and Functional Networks. The fast developed technologies have greatly expanded the functions of UCAVs, and different cooperative relationships may bring various functional UCAV formations to satisfy the continuously changing missions. In order to efficiently complete the given missions, we need to analyze the relationships of the net constructing structures between physical and functional levels in UCAV formations.

From Figure 1, we can see that one SoS (system of systems) of UCAV can be divided into several parts according to the needs of missions, such as fight network, interception network, support network, management network, and communication network. The latter one is communication network which can be regarded as the physical network and other networks are functional networks which are in close relationships with the physical network. For most real UCAV systems, their functional connections and physical connections are not equivalent.

2.1.1. Heterogeneity of UCAVs. For UCAV formation, each single UCAV has its own special features which match different kinds of functional networks, we suppose that there are N kinds of UCAVs, and the number of UCAVs k is $|R_k|$, the state space is S_k, and the relative action state is A_k. Then the mapping formula can be described as

$$\prod_{k=1}^{N} {S_k}^{|R_k|} \longrightarrow \prod_{k=1}^{N} {A_k}^{|R_k|}. \tag{1}$$

The transforming description can be seen in Figure 2.

In Figure 2, $\mathbf{E}$ means the environment, and the other variables can be found in Section 2. Figure 2 is a typical OODA ring which can also reflect the transforming process of constructing the physical net to complete the task of functional net. A stable and static physical net can be useful to keep the high efficiency of UCAV formation. But, in real combat, the dynamic environment and other continuous changing factors may need a dynamic structure to support UCAV formation.

2.1.2. Time-Varying Features of UCAV Structure. According to the analysis in Section 1, it is easy to understand the importance of a dynamic structure of UCAV formation. The description of the dynamic model can be seen in Figure 3.

Figure 3 shows the dynamic process of the transformation in the net constructing structure. During different time areas,

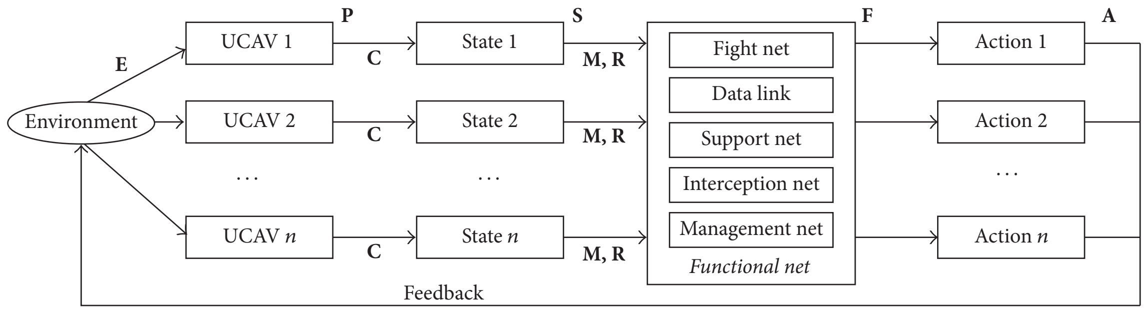

Figure 2: State transformation description of UCAV formation.

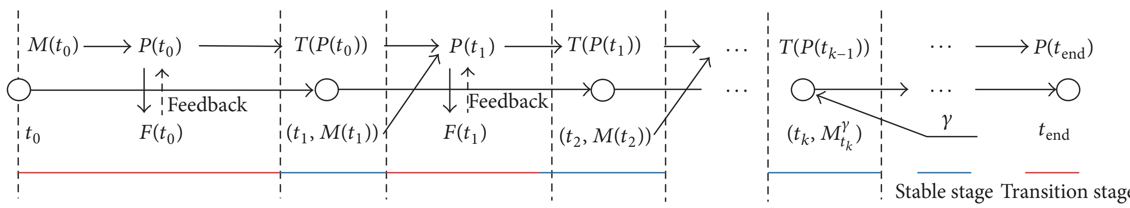

Figure 3: Dynamic process description of formation.

the physical structure is different due to the needs of the missions and the features of each UCAV. $P(t)$ is the time-varying function of physical structure which is driven by the missions. Different missions may stimulate different physical structure which can affect the style of functional structure $F(t)$ greatly. The results coming from functional structure may also reaffect the physical construction. The physical structure will change at time t_n $(n = 1, 2, \dots, N)$, and γ in Figure 3 means the unexpected missions which may cause the changes of the physical structure. In particular, time between t_k and t_{k+1} is not a constant, and it depends on the needs of the relative missions.

Formula (2) can describe the dynamic process:

$$\begin{gathered} P(t) = P(t) + \Delta P, \quad t \in (t_k, t_{k+1}), \ k = 1, 2, \dots, N \\ P(t_{k+1}) = T(P(t_k)), \quad k = 1, 2, \dots, N \\ P(t_0) = (V_0, E_0, C_0). \end{gathered} \tag{2}$$

From formula (2), we can see that, during the stable stage, the physical structure keeps a stable status without considering the error ΔP, which can be described as $\Delta P = f(\Delta V, \Delta X, \Delta Y, \Delta Z)$, $\Delta V, \Delta X, \Delta Y$, and ΔZ are the velocity and position errors of each UCAV. At time t_k, $k = 1, 2, \dots, N$, the physical structure may change due to the new coming missions. T is the transforming function which can help the system to complete the update. $P(t_0)$ is the initial description of the structure which is decided by the given mission.

2.2. Node Survival Model of Multi-UCAV Formation. According to [16–18], we can conclude some obvious features of complex system. They are as follows:

(i) The component systems achieve well-substantiated purposes independently even if detached from the overall system.

(ii) The whole function of a complex system cannot be easily composed of every single subsystem $(1+1 > 2)$.

(iii) It has some intelligent features in some degree which can complete a special mission by predicting the situation using the current information.

From the features we mentioned above, we can regard the UCAV formation as a complex system. Then the vulnerability feature should be analyzed in order to keep the system stable.

The failure probability function can be described as [19]

$$W_\alpha(k_i) = \frac{k_i^\alpha}{\sum_{i=1}^{N} k_i^\alpha}, \quad (-\infty < \alpha < \infty), \tag{3}$$

where k_i denotes the degree of the node i and α can be regarded as the measure of the knowledge on the network structure. There are four kinds of conditions:

(i) $\alpha < 0$, which means that the attacker masters more information about the nodes with low degree. Node with low degree may be more vulnerable and the attacker may use the low-node-first attack strategy.

(ii) $\alpha > 0$, which means that the attacker masters more information about the nodes with high degree. Node with high degree may be more vulnerable and the attacker may use the high-node-first attack strategy.

(iii) $\alpha = 0$, which means the random attack.

(iv) $\alpha = \infty$, which means the deliberate attack.

3. Description of Route Temporary Blindness Problem in UCAV

In Figure 1, the importance of physical and functional structure of UCAV formation has been described. We can

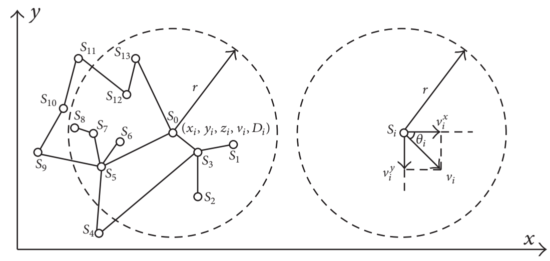

Figure 4: Description of RTB problem.

easily find that the physical network is the foundation of the whole mission. And a proper physical structure is the most important factor for the formation to complete the given mission. And, in this paper, we regard the communication network as the physical network. Thus, the Route Temporary Blindness problem comes.

3.1. Problem Statement. When cooperating with other UCAVs during a mission, a single UCAV needs the information from its neighbors. A stable and reliable neighbor may be of great importance to keep the stable status of the whole structure.

The Route Temporary Blindness problem may be caused in different stages:

(1) During relatively stable stage, the problem may be caused by ΔP. The accumulated errors in position may disturb the normal prediction of the single UCAV, and the deviated position within an information updated cycle may lead to the overranging of the communication radius. Then the chosen neighbor node may be unavailable and the communication in next cycle may be broken.

(2) At the mission transforming moment, the problem may be caused by the change of the dynamic physical structure. The vulnerability of the nodes in different mission processes may get different values which may cause the changes in position and connection among UCAVs. When a mission changes, the highest degree neighbor may change from the most vulnerable node to the least vulnerable node. So the neighbor needs to be changed in order to protect the formation from the future temporary blindness problem.

From Figure 4, S_i means the UCAV node in formation, S_0 is the node which has been researched on, and $(x_i, y_i, z_i, v_i, D_i)$ is the information communicated between S_0 and its neighbors. x_i, y_i, and z_i are the position information, v_i is the velocity, and D_i is the degree of its neighbors.

3.2. RTBA Model

3.2.1. Route Temporary Blindness Physical Avoidance (RTBPA) Model. In order to avoid the RTB phenomenon, we need to predict the future position of the UCAV. Assume $\Delta T = t_k - t_{k-1} = c\Delta t$, Δt is one of the intervals between t_k and t_{k-1}, and c means the number of the intervals. We regard the whole process as a combination of uniform motion and accelerated motion. If the information at time t_{k-1} is given, then the position in X direction at time t_k obeys Gauss distribution.

During kth interval in time $[t_{k-1}, t_k]$, the position, velocity, and acceleration of UCAV u_i in X direction can be described as x_k, v_k^x, and a_i^x, and they have the following relationships:

$$\begin{aligned} v_k^x &= v_0^x + \sum_{i=0}^{k-1} a_i^x \Delta t, \\ x_k &= x_0 + k v_0^x \Delta t + \frac{1}{2}\sum_{i=0}^{k-1} (2k - 2i - 1)\, a_i^x \Delta t^2. \end{aligned} \tag{4}$$

According to the definition of Gauss distribution, if the position of u_i at t_{k-1} in X direction is given, we can set the Gauss variables of position at t_k as: $\mu_x = E(x_k)$, and $\sigma_x^2 = D(x_k)$. And, after $\Delta T = t_k - t_{k-1} = m\Delta t$, we can get the probability

$$\begin{aligned} & p\{(x_k, y_k) \mid (x_{k-1}, y_{k-1})\} \\ & \quad = \frac{1}{2\pi\sigma_x\sigma_y} \exp\left\{\frac{-(x_k - \mu_k)^2}{2\sigma_x^2} + \frac{-(x_k - \mu_k)^2}{2\sigma_x^2}\right\}. \end{aligned} \tag{5}$$

Then, we can get the position at $t_k = t_{k-1} + m\Delta t$ as

$$\begin{aligned} x_k &= \text{predict\_pos\_}x\left(x_{k-1}, v_{k-1}^x, a_{k-1}^x, \Delta T\right), \\ y_k &= \text{predict\_pos\_}y\left(y_{k-1}, v_{k-1}^y, a_{k-1}^y, \Delta T\right). \end{aligned} \tag{6}$$

3.2.2. Rout Temporary Blindness Functional Avoidance (RTBFA) Model

(a) Analyze the Mission: Positive and Negative Missions. In order to simplify the combat conditions, the missions have been divided into two different types, namely, positive mission M_P and negative mission M_N.

Definition 1. One defines the positive mission as a preplanned mission which may be executed based on the possessed knowledge of the enemy. And the positive mission may have a hiding policy to reveal the information to the enemy as less as possible. In all, when executing a positive mission, the formation may have obtained the priority in combat.

According to Definition 1, one can see that when executing a positive mission, $\alpha = 0$ or $\alpha < 0$. The enemy may consider random attack policy or low degree node preferential policy. Neighbor node with low degree may become more vulnerable.

Definition 2. Negative mission is an unintentional or partial knowledge possessed mission; it happens when outer threats come out without prediction or inner malfunctions appear in some probability. During negative mission process, the enemy has occupied the combat situation and it has possessed more information of our formation.

Analyzed by Definition 2, when executing a negative mission, $\alpha \to \infty$ or $\alpha > 0$. The enemy may consider deliberate attack policy or high degree preferential policy. Neighbor node with high degree may become more vulnerable.

(b) Measurement of Possessed Information. The detective information is regarded as the possessed information about the enemies, and the detective problem is related to the hypothesis testing problem:

H_0: there is no object within the search range.

H_1: there exist (an) object(s) within the search range.

Suppose that the probabilities are $P_0 = P(H_0)$ and $P_1 = P(H_1)$ and the related variables of detective problem are as follows.

(i) Probability of False Alarm (PFA). It is the probability of a false decision which regards an event that did not happen as an event that happened. $P_F = \Pr(u = 1 \mid H_0)$, and the PFA of airborne pulsed Doppler radar is [20]

$$P_F = \int_{V_T}^{\infty} \frac{R}{\psi_0} \exp\left(-\frac{R^2}{2\psi_0}\right) dR = \exp\left(-\frac{V_T^2}{2\psi_0}\right), \quad (7)$$

where R is the amplitude of noise envelope from the detector, ψ_0 is the mean square value of noise voltage, and V_T is threshold voltage.

(ii) Probability of the Right Decision. It is the probability of a right recognition and decision which can be described as

$$P_L = \Pr(u = 0 \mid H_0) = 1 - P_F = 1 - \exp\left(-\frac{V_T^2}{2\psi_0}\right). \quad (8)$$

(iii) Probability of Detection. When an event happened and is correctly decided by the detective facility, the probability can be described as $P_D = \Pr(u = 1 \mid H_1)$. And the PD of airborne pulsed Doppler radar is

$$P_D = \int_{V_T}^{\infty} \frac{R}{\psi_0} \exp\left(-\frac{R^2 + A^2}{2\psi_0}\right) I_0\left(\frac{RA}{\psi_0}\right) dR. \quad (9)$$

(iv) Probability of Miss. It is the opposite meaning of PFA, that is, when an event did happen while the detective facility decides that it as an event that did not happen. $P_M = \Pr(u = 0 \mid H_1)$, and the PM of airborne pulsed Doppler radar is

$$\begin{aligned} P_M &= 1 - P_D \\ &= 1 - \int_{V_T}^{\infty} \frac{R}{\psi_0} \exp\left(-\frac{R^2 + A^2}{2\psi_0}\right) I_0\left(\frac{RA}{\psi_0}\right) dR. \end{aligned} \quad (10)$$

Under condition H_0, the information Shannon can be regarded as

$$I_0 = -\sum_{i=1}^{n} p_i \log_2(p_i) = -P_F \log_2(P_F) - P_L \log_2(P_L). \quad (11)$$

And, under condition H_1, the information Shannon can be regarded as

$$I_1 = -\sum_{i=1}^{n} p_i \log_2(p_i) = -P_F \log_2(P_M) - P_D \log_2(P_D). \quad (12)$$

The information Shannon [21] under detection condition is set as the sum of I_0 and I_1:

$$\begin{aligned} I_M &= P(H_0) \cdot I_0 + P(H_1) \cdot I_1 \\ &= P_0 \cdot [-P_F \log_2(P_F) - P_L \log_2(P_L)] + P_1 \\ &\quad \cdot [-P_M \log_2(P_M) - P_D \log_2(P_D)]. \end{aligned} \quad (13)$$

I_M reflects the detective information. The bigger I_M gets, the more the information is needed. Set an expected value I_E, and if $I_M > I_E$, the information is enough and the mission can be regarded as positive mission. If $I_M < I_E$, the mission can be regarded as a negative mission:

$$\alpha = I_E - I_M. \quad (14)$$

3.2.3. Avoidance Function

$$L_i = \begin{cases} 1, & \text{others} \\ 0, & \text{if } (r_i - r_0) \parallel (W_\alpha(k_i) - W_0) < 0. \end{cases} \quad (15)$$

L_i is a decision function that measures the effectiveness of the current chosen nodes.

3.3. RTBA Utility Indexes. In order to get a more reliable communicating partner, we set the following indexes.

(i) Continuously connecting feature: $\Delta T = \max_{j \in I_i} \Delta T_j$, I_i being the set of the neighbors of u_i.

According to the predicted position of UCAV u_0 and u_k, the relative position between the sender and receiver can be described as

$$\Delta d = \sqrt{(x_k - x_0)^2 + (y_k - y_0)^2}. \quad (16)$$

After ΔT, the positions of the sender and receiver are (x_0', y_0') and (x_k', y_k').

$$\Delta d' = \sqrt{(x_k' - x_0')^2 + (y_k' - y_0')^2}, \quad (17)$$

where $\Delta d'$ describes the connecting relationship between UCAV u_0 and u_k after ΔT and ΔT can be regarded as continuously connecting feature.

(ii) Nearer connecting distance: $D = \min_{j \in s_i^n} D_j$, $D_j = \sqrt{(x_j - x_d)^2 + (y_j - y_d)^2}$.

The complex index can be described as

$$\begin{aligned} Q &= \min_{j \in s_i^n} Q_j \\ &= \begin{cases} \left(D_j + \dfrac{\tau}{\Delta T_j}\right) \cdot L_i \cdot W_\alpha(k_j), & (D_j < D_i) \wedge (\Delta T \geq 1) \\ \text{MAX\_VALUE}, & \text{otherwise}, \end{cases} \end{aligned} \quad (18)$$

where τ is the reliability weight of neighbor nodes.

The connecting result of each node can be decided by the value of Q, and we can finally get a neighbor matrix m which decides the structure of the formation. According to the features of complex networks, if more than two nodes need to be replaced during the same mission period, then the new nodes choosing order may be very important to the net structure. Different nodes choosing order may lead to different neighbor matrix. $m_i \in M$ is the neighbor matrix set, and we need to get a proper matrix which can bring a more stable and effective result.

4. Dynamic Topology Optimizing Method Based on Synchrony Features

4.1. The Synchronization of UCAV Formation. Synchronization phenomenon exists widely in nature, such as the synchronization of fireflies glowing and the synchronization of large groups of neurons in human brains and the clapping frequency synchronization [22]. The synchronization phenomenon is also an important concept in UCAV formation and it reflects the recognizing abilities of each node and we give the definition of synchronization in formation.

Definition 3. Synchronization in UCAV formation can be regarded as the agreement on the combat situation by different UCAV nodes. And it can be described by the conformance degree towards the same combat situation.

As one mentioned in Section 3.1, each UCAV node can be regarded as a dynamic system, and there exists coupling effect between two connected nodes. Then the dynamic equation of each node can be given as below:

$$\dot{x}_i = F(x_i) - \sigma \sum_{j}^{N} l_{ij} \mathbf{H} x_j, \quad i = 1, 2, \ldots, N, \tag{19}$$

where $x_i \in \mathbf{R}^d$ is a d dimensional state vector and $F : \mathbf{R}^d \to \mathbf{R}^d$ is the dynamic equation which obeys Lipchitz condition [23].

σ is coupling efficient, $\mathbf{H}$ describes the different coupling styles among different vibrators, l_{ij} is the element with Laplace features, and $x_i(t)$ $(i = 1, 2, \ldots, N)$ is the state of each node.

If any solution to (20) satisfies the following condition, then we can say that the system is a completely synchronized system:

$$\lim_{t\to\infty} \left\| x_i(t) - x_j(t) \right\| = 0, \quad i, j = 1, 2, \ldots, N. \tag{20}$$

If there exists a real number ε which is greater than zero, it constructs the following relationship:

$$\lim_{t\to\infty} \left\| x_i(0) - x_j(0) \right\| < \varepsilon. \tag{21}$$

If any solution to the equation above satisfies the following condition, then we can say that the system is a local synchronized system:

$$\lim_{t\to\infty} \left\| x_i(t) - x_j(t) \right\| = 0, \quad i, j = 1, 2, \ldots, N. \tag{22}$$

The UCAV formation can be regarded as a local synchronization system in this research.

4.2. Indexes of Synchronization in UCAV Formation. The synchronization of UCAV formation is decided by the following three factors [24]:

(i) The dynamic features of each node.

(ii) The net structure, namely, matrix m.

(iii) The coupling effect between different dynamic systems.

According to [24], $K = \lambda_{\max}/\lambda_2$ can be used to describe the synchronization features. $\lambda_{\max}$ describes the robustness towards the communication delay and λ_2 means the second largest eigenvalue which can also be regarded as algebraic connectivity. The synchronization feature of the system is often improved by decreasing the value of K. λ_i in ascending sort order is the eigenvalue of matrix m. The evaluating function is set as

$$E(G) = \left(\frac{\lambda_2}{\lambda_{\max}}\right)_G \sum_R \left(w_r \sum_k e(k_i)\right), \tag{23}$$

where $(\lambda_2/\lambda_{\max})_G$ is used to evaluate the connectivity and delay robustness of UCAV formation, R is the number of kinds of functional nodes, w_r means the weight in relation to different kinds of functional nodes, $\sum_R w_r = 1$, and $\sum_k e(k_i)$ is the sum of all the nodes' efficiencies. From [25], we can get the node's efficiency model:

$$e(k_i) = \frac{e^{(\nu - \beta k_i)}}{1 + e^{(\nu - \beta k_i)}}, \tag{24}$$

where k_i is the degree of node i and ν and β are the modifying variables according to the situation. In order to get an optimal value, we need to get $\max(E(G))$. Then the optimal function can be set as

$$\begin{aligned} \max \quad & (E(G)) = \left(\frac{\lambda_2}{\lambda_{\max}}\right)_G \sum_R \left(w_r \sum_k e_r(k_i)\right) \\ \text{s.t.} \quad & \sum_R w_r = 1. \end{aligned} \tag{25}$$

4.3. Dynamic Topology Constructing Method Based on HPSO Method. According to the aforementioned contents, the optimal structure needs to be found in order to keep the stability and synchrony of the UCAV system. The new nodes choosing order has brought more than one kind of net constructing structure. Thus the problem has been simplified as finding a proper sequence.

4.3.1. Calculating Process. According to the problem simplification above, we have changed the complex model into a typical TSP model; thus we use hybrid particle swarm optimization method to solve this problem. The detailed steps can be acquired in Figure 5.

4.3.2. Encoding Method. The length of the code equals the number of nodes which need to find new partners. The codes can be described by natural numbers which

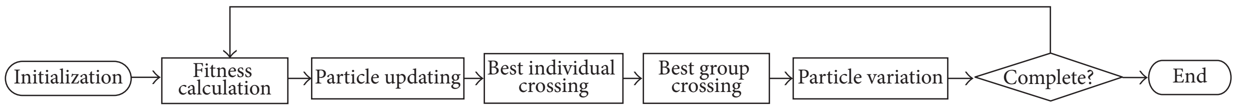

Figure 5: Calculating steps.

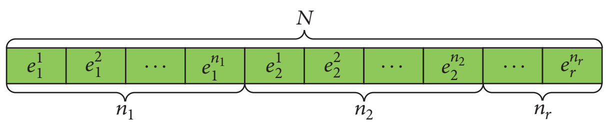

Figure 6: Encoding method.

should get repeated. If the new nodes choosing order is $\{1, 2, 5, 6, 9, 7, 8, 3, 4, \ldots, n\}$, then the code can be set as $\{1, 2, 5, 6, 9, 7, 8, 3, 4, \ldots, n\}$.

In Figure 6, $e_r^{n_r}$ is the sequence number which means the sequence of the node n_r in r kind of functional node. Different kinds of functional nodes may match different kinds of weights which are very important to the final result.

4.3.3. Code Crossing Rules. In order to accelerate the process of convergence, the crossing rules are brought into the algorithm. And the detailed rules are described in Figure 7.

From Figure 7, the crossing rules are as follows:

(i) Selecting two crossing points in the old code set randomly.

(ii) Exchanging the codes between the crossing points.

(iii) Executing the self-testing process to avoid the repeated codes.

(iv) Rebuilding the codes.

5. Simulation

5.1. Hardware Condition. Hardware condition is as follows: CPU: P4 2.8 GHz, RAM: 1.5 G, and Matlab 2010, NS2.

5.2. Software Settings

Variables	Values
Simulation range	100 km^2
UDP data	512 Bytes
Transportation fading model	Friis
UCAV communicating distance	1 km
Communication treaty	UDP
Simulation time	200 s
Simulation times	1000

5.3. Evaluation Indexes. In order to verify the effectiveness of RTBA model, we use Packet Delivery Ratio (PDR) and End-to-End Delay (EED) to complete the evaluating process.

5.3.1. Packet Delivery Ratio (PDR): Ratio of Information Received by All the Possible Receiving Nodes to Information Sent by an Exact Sending Node

$$\mathrm{PDR} = \frac{\sum_n D_r}{D_s}. \tag{26}$$

D_r is the information received by a chosen node, $\sum_n D_r$ describes the information received by n possible chosen nodes. D_s describes all the sent information.

5.3.2. Average End-to-End Delay (AEED): The Average Time of Information Transportation from Sender to Receivers

$$T_D = \frac{\sum_{i=1}^{n} \left(T_i^r - T_i^s\right)}{n}, \tag{27}$$

where T_i^r means the time when the i data package is received, T_i^s means the time when the i data package is sent, and n is the number of data packages.

5.4. Simulation and Analysis

5.4.1. RTBA Model Analysis. Three models are put forward to compare the PDR values. Here we used RTBA, RTBPA, and normal model to make a comparison while the normal model is the traditional communication model without any restoring strategies. We first assume that the mission has kept a stable status, and the UCAV nodes fly at an increasing velocity.

The initial number of UCAV nodes is 50 in Figure 8(a), and we can find that during a stable status, the RTBA model may have a better PDR value. With the increasing of the velocity of nodes, the robustness of UCAV formation may be influenced. The continuously increasing velocity may enlarge the error in RTB problem, so the PDR may decrease, but RTBA model still has a better performance than others. And, in this situation, RTBPA model has almost the same performance as RTBA. Figure 8(b) has the same simulating environment but an increasing UCAV number. We set 100 UCAV nodes in the right side. We can easily find that the increasing number of UCAVs may have an obvious superiority. At a relatively low velocity, the normal model may even have a better value than the others, but, with the increasing of the velocity, RTBA model will show its superiority.

In order to describe the performance of models in an unstable status, a sudden threat is designed at time 30 s, and then negative mission M_N appears. The velocity of UCAV formation is given as 100 m/s and the PDR values are shown in Figure 9.

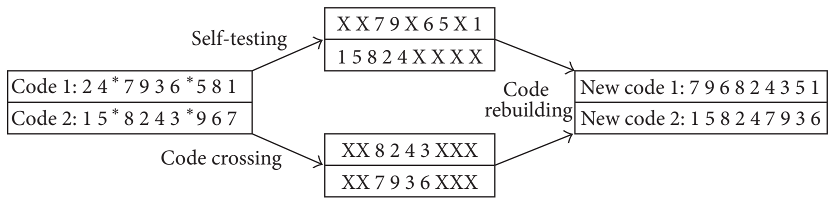

FIGURE 7: Crossing method.

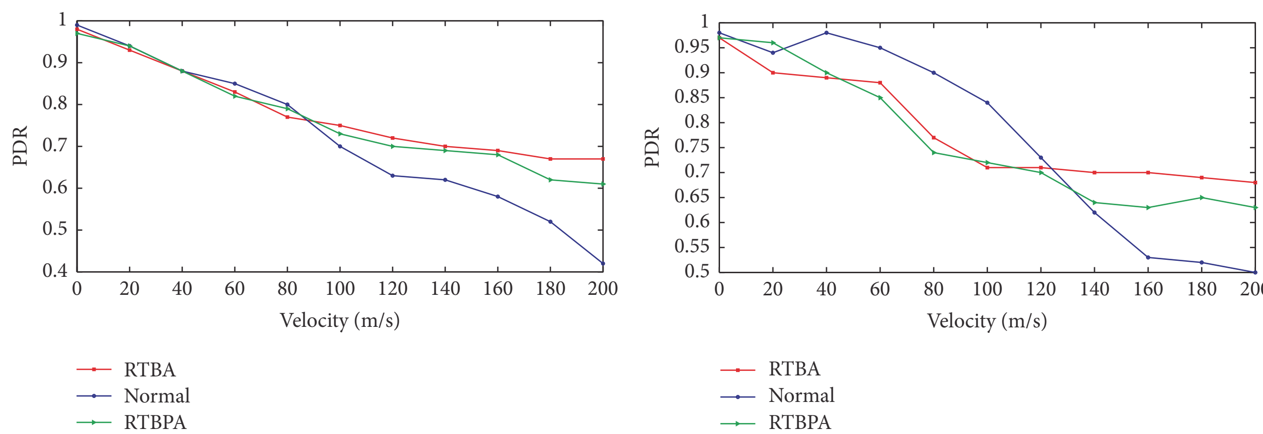

(a) (b)

FIGURE 8: PDR comparison among different models.

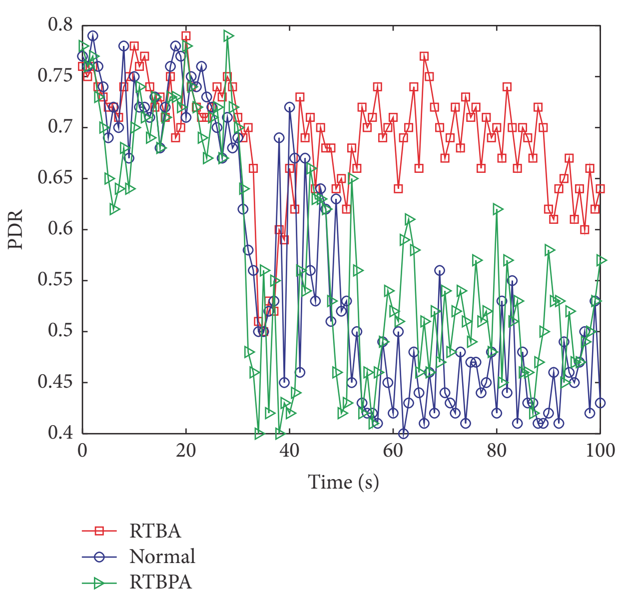

FIGURE 9: PDR comparison when sudden threat comes at time 30 s.

Figure 9 reflects the PDR comparison when executing M_N, and the unexpected threat has influenced the robustness of the formation. After 30 s, the threat has enlarged the potential risk of parts of the nodes, then PDR in all the models have descended. At about 45 s, PDR in RTBA model has bounced back and kept a stable value, while PDR in normal and RTBPA model has not bounced back. The threat has great influences on the functional feature of the nodes; RTB model may have a better self-testing and restoring ability which can be important to keep the robustness of UCAV formation.

AEED can also be used to evaluate the efficiency of a cooperative system. From Figure 10, RTBA model has a relatively low AEED value with the increasing of the velocity. Figure 10(a) has 50 nodes and Figure 10(b) has 100 nodes and Figure 10(a) has an obvious low average value compared to that in Figure 10(b). More nodes may offer more connecting choices, and more choices may shorten the node choosing time, so the average value of AEED is lower. The increasing velocity may enlarge the physical error and the formation in RTBA and RTBPA model has to test the connectivity of the system for many times, and then the value of AEED increases.

Figure 11 shows the average time delay probability in different models after 1000 times' simulations when the formation encounters a sudden threat (negative mission). For simplification, we make the time delay remain at one decimal. In RTBA model, the time delay focus on 0.2 to 0.4 seconds. In RTBPA model, the time delay focus on 0.4 to 0.8 seconds. In normal model, though the time delay shows its random features, it has a greater average value. And we can find the following: $\sum p_{\text{RTBA}} = 1$, $\sum p_{\text{RTBPA}} < 1$, and $\sum p_{\text{Normal}} < 1$. Among 1000 simulations, there exists communicating broken situation in RTBPA and normal models. If a communicating broken problem happens, value of AEED may trend to be infinite and the result may be totally different.

5.4.2. Optimal Synchronized Structure Seeking. The superiority has been analyzed in Section 5.4.1; then the optimal structure should be acquired in Section 5.4.2.

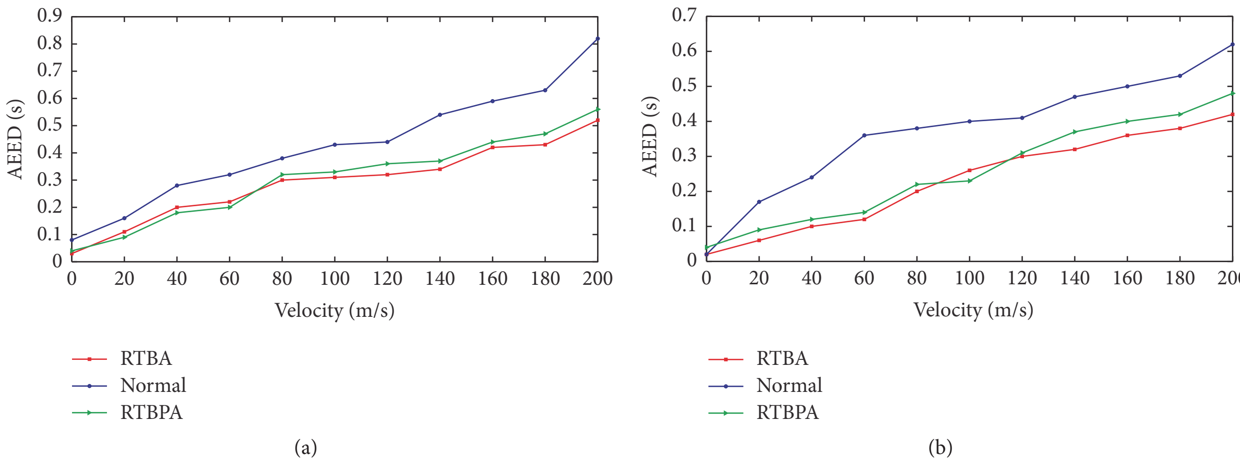

Figure 10: AEED comparison among different models.

Table 1: Initialization of UCAV structure.

UCAV number	21 (20 communication nodes in relative UCAV platform)	
Kinds of functional nodes	4 (1 center command node, 3 c2 nodes, 5 management nodes, 11 execution nodes)	
Mission stage	2 stable stages, 1 mission changing stage (sudden threat comes at 30 s)	
$\lambda_{max}/\lambda_2 = 21.221$	$1/\lambda_2 = 2.447$	$e = 38$ (edges)

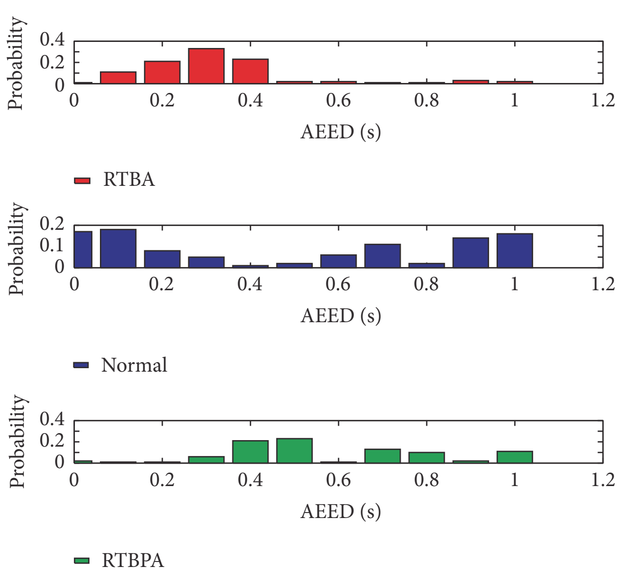

Figure 11: AEED probabilities of three models under sudden threats.

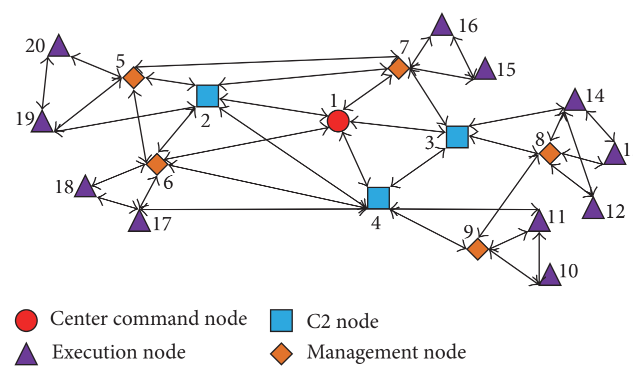

Figure 12: Description of initial net structure.

The initial structure can be found in Figure 12 and the values of features can be seen in Table 1.

We assume that, after the appearance of a sudden threat, nodes 2, 6, and 9 may get a higher probability of being attacked, and then a better node choosing order is needed so as to get a better constructing structure.

From Figure 13, HPSO has an obvious better result than PSO, the best node choosing order is as follows: bestSequence = (4 → 19 → 18 → 5 → 2 → 1 → 10 → 8 → 11 → 17), and the optimized structure can be found in Figure 14.

From Figure 14 we can see that the edges among different nodes have increased, and the edges around nodes 2, 6, and 9 have decreased. The whole formation has a flatter structure which contains more cross-grade connections. And the relative values of relative variables are as follows: $1/\lambda_2 = 1.718$, $\lambda_{max}/\lambda_2 = 16.702$, $e = 44$, and $E = 0.724$. The value of λ_{max}/λ_2 has decreased due to the interception of the negative mission. The result can also describe that a flat structure may be proper to improve the synchrony of UCAV formation.

6. Conclusions

Dynamic UCAV formation net constructing problem under RTB situation is solved in this paper. Robustness and synchronization are set as two important indexes to seek for an optimal UCAV formation structure. In order to analyze the influences caused by the combat missions, the mission kinds and mission stages are classified, and a dynamic structure

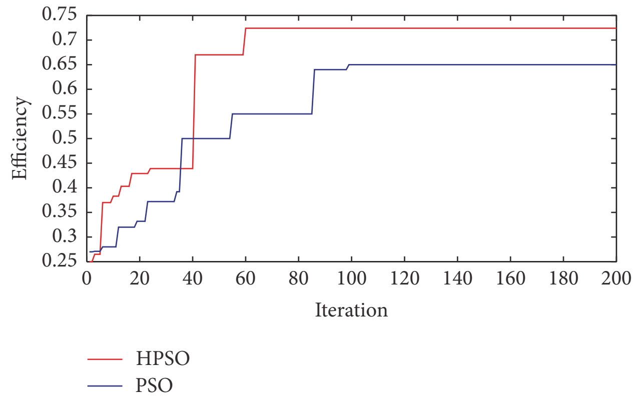

FIGURE 13: Comparison between PSO and HPSO algorithm.

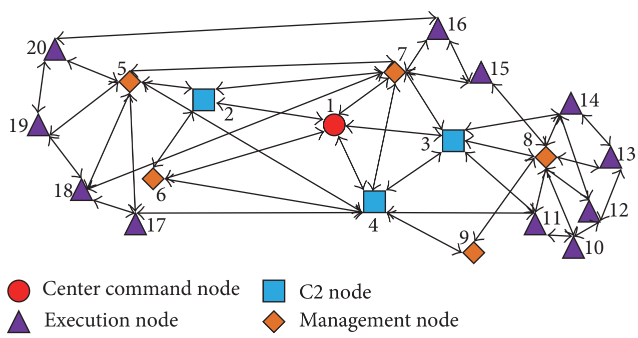

FIGURE 14: Optimized structure of UCAV formation.

changing mechanism is put forward. RTBA model is given to optimize the functional and physical nodes in order to keep the robustness of the formation. And HPSO method is used to find a proper structure to get an appropriately synchronized features. The dynamic structure constructing problem has been transferred to a node choosing sequence optimizing problem which can be regarded as a TSP problem. Finally, the efficiency of RTBA model has been given according to the comparison with other models and the optimal structure with better robustness and synchronization has been acquired using HPSO method.

From the perspective of net constructing consumption, the optimized formation structure is able to keep a synchronized feature with not many changes in edges. This will be very important to decrease the cost of keeping the connections among different UCAVs.

From the perspective of robustness, the high risky nodes have relatively low probability of being connected in the optimized structure which can be useful to keep the robustness of the formation.

From control and command perspective, edges in formation have increased obviously, and the cross-grade connections have taken a great ratio in the optimized structure. A flatter formation is useful to improve the comprehensive efficiency of UCAV formation.

Combat situation is very important because it can influence the state of UCAV and even the structure of UCAV formation. In this content, combat situation is simple and the scenario is regarded as an absolutely ideal space. A complex scenario may be more credible in real combat situation. Thus we need to pay more attention to this area in order to put the theory into practice.

Competing Interests

The authors declare that they have no competing interests.

References

[1] C. Pan, W. Ye, J. Chen, and J. Guo, “Cooperative control for UCAVs path planning,” in *Proceedings of the 8th World Congress on Intelligent Control and Automation (WCICA ’10)*, pp. 5259–5263, Jinan, China, July 2010.

[2] J. Chen and X. Gao, “Modeling and analysis of command and control system in cooperative air combat,” *Engineering and Applications*, vol. 45, no. 10, pp. 195–198, 2009.

[3] A. H. Levis, *Time Sensitive Control of Air Combat Operations*, Cebter of Excellence in Command, Control, Communication and Intelligence, George MASON University, 1998.

[4] F. D. J. Bowden, *Petri Nets and Their Application to Command and Control Systems*, Information Technology Division, Electronics and Surveillance Research Laboratory, Salisbury, Australia, 1996.

[5] S. Erkan, M. Kandemir, and G. Giger, “Advanced task assignment for unmanned combat aerial vehicles targeting cost efficiency and survivability,” in *Proceedings of the 46th AIAA Aerospace Sciences Meeting and Exhibit*, Reno, Nev, USA, January 2008.

[6] C. Schumacher, P. Chandler, P. Pachter, and L. Pachter, “Constrained optimization for UAV task assignment,” in *Proceedings of the AIAA Guidance, Navigation, and Control Conference and Exhibit, Guidance, Navigation, and Control and Co-located Conferences*, Providence, RI, USA, August 2004.

[7] D. Zhang, G. Xie, J. Yu, and L. Wang, “Adaptive task assignment for multiple mobile robots via swarm intelligence approach,” *Robotics and Autonomous Systems*, vol. 55, no. 7, pp. 572–588, 2007.

[8] T.-Q. Ni, J.-D. Wang, and Y.-A. Liu, “Application of particle swarm algorithm in route planning of UAV,” *Systems Engineering and Electronics*, vol. 33, no. 4, pp. 806–810, 2011.

[9] R. J. Szczerba, P. Galkowski, I. S. Glicktein, and N. Ternullo, “Robust algorithm for real-time route planning,” *IEEE Transactions on Aerospace and Electronic Systems*, vol. 36, no. 3, pp. 869–878, 2000.

[10] S.-Q. Tang, C.-Q. Huang, J. Hu, and W.-C. Wu, “Threat equivalent and improved PSO algorithm based real-time method of UCAV route planning,” *Systems Engineering and Electronics*, vol. 32, no. 8, pp. 1706–1710, 2010.

[11] J.-Y. Du, F.-M. Zhang, H.-B. Mao, H.-W. Liu, and J. Yang, “Game theory based multi-UAV cooperative searching model and fast solution approach,” *Journal of Shanghai Jiaotong University*, vol. 47, no. 4, pp. 667–678, 2013.

[12] B. Di, R. Zhou, and Q.-X. Ding, “Distributed coordinated heterogeneous task allocation for unmanned aerial vehicles,” *Control and Decision*, vol. 28, no. 2, pp. 274–278, 2013.

[13] X. K. Bao, *Modeling and Analyzing of Networked Operation Synchronization*, National University of Defense Technology, Changsha, China, 2009.

[14] M. M. Zavlanos, L. Spesivtsev, and G. J. Pappas, "A distributed auction algorithm for the assignment problem," in *Proceedings of the 47th IEEE Conference on Decision and Control (CDC '08)*, pp. 1212–1217, Cancun, Mexico, December 2008.

[15] D. Medina, F. Hoffmann, F. Rossetto, and C.-H. Rokitansky, "Routing in the airborne internet," in *Proceedings of the Integrated Communications, Navigation, and Surveillance Conference (ICNS '10)*, pp. 11–13, Herndon, Va, USA, May 2010.

[16] X. Huang, *Scientific Research on Complex Methodology*, Qsinghua University, Beijing, China, 2014.

[17] S. Boccaletti, V. Latora, Y. Moreno, M. Chavez, and D.-U. Hwang, "Complex networks: structure and dynamics," *Physics Reports*, vol. 424, no. 4-5, pp. 175–308, 2006.

[18] R. John, *Dynamic Complexity in System of Systems*, Engineering & Technology. Advanced Sytems. Boeing Company, 2007.

[19] L. K. Gallos, R. Cohen, P. Argyrakis, A. Bunde, and S. Havlin, "Stability and topology of scale-free networks under attack and defense strategies," *Physical Review Letters*, vol. 94, no. 18, Article ID 188701, 4 pages, 2005.

[20] D. Luo, Z. Yang, H. Duan, Z. Wu, and C. Shen, "Heuristic particle swarm optimization algorithm for air combat decision-making on CMTA," *Transactions of Nanjing University of Aeronautics & Astronautics*, vol. 23, no. 1, pp. 20–26, 2006.

[21] D. Stein, J. Witkoskie, S. Theophanis, and W. Kuklinski, "Random set tracking and entropy based control applied to distributed sensor networks," in *Proceedings of the Proceedings of SPIE*, vol. 6567, pp. 656709–656722, Beijing, China, November 2007.

[22] S. Li, *Research on the Mechanism of Cascading Dynamics and Behaviors of Complex Networks*, Beijing University of POSIS and Telecommunications, 2012.

[23] D. Shi, G. Chen, W. W. K. Thong, and X. Yan, "Searching for optimal network topology with best possible synchronizability," *IEEE Circuits and Systems Magazine*, vol. 13, no. 1, pp. 66–75, 2013.

[24] M. Jalili, "Enhancing synchronizability of diffusively coupled dynamical networks: a survey," *IEEE Transactions on Neural Networks and Learning Systems*, vol. 24, no. 7, pp. 1009–1022, 2013.

[25] J. Yan, X.-M. Li, L.-J. Liu, and B. Liu, "Combat network synchronization of air fleet formation," *Systems Engineering and Electronics*, vol. 36, no. 8, pp. 1566–1572, 2014.

Hindawi Publishing Corporation
Mathematical Problems in Engineering
Volume 2016, Article ID 8293582, 12 pages
http://dx.doi.org/10.1155/2016/8293582

Research Article

Mobility-Aware Video Streaming in MIMO-Capable Heterogeneous Wireless Networks

Hayoung Oh

School of DASAN University College, Ajou University, Suwon, Gyeonggi, Republic of Korea

Correspondence should be addressed to Hayoung Oh; hyoh@ssu.ac.kr

Received 18 March 2016; Revised 15 June 2016; Accepted 19 July 2016

Academic Editor: Zhao Cheng

Multiple input and multiple output (MIMO) is a well-known technique for the exploitation of the spatial multiplexing (MUX) and spatial diversity (DIV) gains that improve transmission quality and reliability. In this paper, we propose a quality-adaptive scheme for handover and forwarding that supports mobile-video-streaming services in MIMO-capable, heterogeneous wireless-access networks such as those for Wi-Fi and LTE. Unlike previous handover schemes, we propose an appropriate metric for the selection of the wireless technology and the MIMO mode, whereby a new address availability and the wireless-channel quality, both of which are in a new wireless-access network so that the handover and video-playing delays are reduced, are considered. While an MN maintains its original care-of address (oCoA), the video packets destined for the MN are forwarded with the MIMO technique (MUX mode or DIV mode) on top of a specific wireless technology from the previous Access Router (pAR) to the new Access Router (nAR) until they finally reach the MN; however, to guarantee a high video-streaming quality and to limit the video-packet-forwarding hops between the pAR and the nAR, the MN creates a new CoA (nCOA) within the delay threshold of the QoS/quality of experience (QoE) satisfaction result, and then, as much as possible, the video packet is forwarded with the MUX. Through extensive simulations, we show that the proposed scheme is a significant improvement upon the other schemes.

1. Introduction

Over recent years, "multiple input and multiple output" (MIMO) technology has grown rapidly in the field of wireless communications. MIMO links have provided a high spectral efficiency in wireless environments through multiple spatial channels and without a need for additional bandwidth requirements [1]. MIMO links provide the following two operational options: (a) simultaneous transmission of different data by multiple antennas that increases the data rate, called "spatial multiplexing" (MUX), and (b) simultaneous transmission of the same data by multiple antennas that increases the reliability or the transmission range, called "spatial diversity" (DIV). With the proliferation of MIMO-capable, heterogeneous wireless technologies and mobile electronic smart devices such as iPhones and iPads, there is a fast-growing interest in mobile video-streaming traffic for such mobile devices. According to the Cisco visual-networking index, mobile video traffic will grow 66-fold over a period of five years [2–4].

One of the main challenges regarding MIMO-capable, heterogeneous wireless technologies is the provision of the support for a robust mobile video service such as Internet Protocol television (IPTV), Voice over Internet Protocol (VoIP) [5], and video streaming [2, 3], whereby fast and seamless handover and forwarding schemes are supported between heterogeneous wireless-access networks. In this environment, seamless mobility and data forwarding are coupled according to user preferences, enabling mobile users to be "always best connected" (ABC) so that quality of service and quality of experience (QoS and QoE) are optimized and maintained; furthermore, the core network of the heterogeneous wireless-access networks continues to evolve into an all-IP-based network. Accordingly, to reduce the handover latency and solve the packet-loss problem, a fast MIPv6 (FMIPv6) handover [6] with an address preconfiguration and a fast IP connectivity has been proposed after the introduction of the Mobile IPv6 (MIPv6) [7] in the Internet Engineering Task Force (IETF); however, this handover proposal is still not robust for mobile video streaming in MIMO-capable, heterogeneous wireless technologies. Although Hierarchical MIPv6 (HMIPv6) [8] and Proxy Mobile IPv6 (PMIPv6) [9] have been proposed for location management and handover-latency enhancement, corresponding limits in the local mobility region persist; plus, even though the GPRS Tunneling Protocol (GTP) and the Dual Stack MIP (DSMIP) are proposed for the support of the IP mobility level between LTE and Wi-Fi, we have chosen to focus on FMIPv6 enhancement to cover the QoS and QoE of mobile video streaming, as well as the global mobility in MIMO-capable, heterogeneous wireless technologies.

Regarding FMIPv6, a mobile node (MN) is previously configured with only one of the new care-of addresses (CoAs) of a specific wireless network before it is attached to a new link. This address preconfiguration, however, is useless when the MN moves to another visited network, or when the change of wireless technology by the MN is in contrast with the corresponding anticipation; therefore, the selection of an inappropriate wireless technology occurs, leading to a fluctuating mobile video-streaming quality that is due to a lack of unused new addresses or an unreliable wireless-channel quality. In this case, FMIPv6 again follows the handover procedure of MIPv6 so that the handover latency increases undesirably. Attempts to improve both MIPv6 and FMIPv6 in a wireless network under the strong assumption of a perfect anticipation have already been completed.

Different from the previous works [10–13], specifically, the main goal of our proposed scheme is a mechanism that selects the “best,” according to an appropriate metric, wireless technology for a robust mobile-video-streaming service among all of the wireless technologies, whereby the handover and video latency are reduced on average, and the effects of perfect and imperfect handover predictions are analyzed in terms of MIMO-capable, heterogeneous wireless technologies.

To our knowledge, this is the first report regarding the problem concerning the need for robust mobile video streaming in terms of MIMO-capable, heterogeneous wireless technologies. Unlike FMIPv6, for which the preconfiguration of one tentative CoA at an MN handover is used, two of the verified tentative CoAs from heterogeneous wireless-access networks are exploited for the proposed scheme to prevent a fast handover from failing with any FMIPv6-related wireless technology for which there is no provisional CoA in a new visited network. By making a fast handover possible in any situation, the scheme reduces the average handover latency and the mobile-video-streaming delay by using a MIMO-transmission mode. We have therefore defined a metric that captures the contribution that each wireless technology provides for the quality improvement of mobile video streaming, while also considering the importance of video packets (in terms of video distortion and play-out deadlines), the QoE, and the video-packet-forwarding mode of MIMO technologies such as MUX and DIV with respect to MIMO-capable, heterogeneous wireless technologies.

Through a performance evaluation, we show that our scheme provides a mechanism that is more robust than those of the other schemes such as eFMIPv6 [10], FMIPv6, HMIPv6, the hybrid algorithm [14] and Handoff Protocol for Integrated Networks (HPINs) [15] for which the MIMO routing protocol (MIR) [16] of mobile-video-streaming services is considered.

The rest of this paper is organized as follows: We present related work and the general system architecture for the proposed scheme in Sections 2 and 3; regarding the MIMO-capable heterogeneous wireless technologies, a robust mobile-video-streaming scheme is described in Section 4; Section 5 presents the analysis and performance results; and lastly, we conclude the paper in Section 6.

2. Related Work

The authors of [17] propose a simulation platform for the analysis of the handover issue for downlink coordinated multipoint (CoMP) transmissions in LTE-A cellular systems. Among the variety of intercell interference coordination (ICIC) strategies, the authors applied a frequency-reuse factor of one in the cell-center areas and a higher reuse factor in the cell-edge areas. In [18], the authors propose a downlink soft handover scheme for cell-edge users in 4G-LTE systems to improve the cell-edge capacity. In the cell-edge areas, capacity loss generally exists; therefore, the authors of [18] used a multicell MIMO, with the cooperation of multiple base stations and different, adaptively exploited multi-cell MIMO transmissions, based on the spatial correlation of a downlink channel and the path loss of adjacent cells, whereby the ergodic link-level capacities are compared. In [19], the authors proposed a novel handover scheme for which the number of detected antennas in a MIMO-capable wireless communication system is used; through the diminishing of the MAC-feedback quantity in the base station, the scheme results in a diversification of the handover decision and a reduction of the MAC overhead. In [20], the authors introduce handover sequences by consisting of a comb cyclically shifted in the frequency domain to identify the MIMO cells. Orthogonal sequences in time domain are used to identify the antennas of MIMO within a cell. Sequence assignment to the cells follows a classical frequency-reuse scheme. With these sequences, the frequency-selective multicell channel of MIMO can be identified with high precision also at the cell edge. In [21], the authors carried out the research of influence by the multiantenna technology MIMO on realization of handover procedure in cellular radio access systems. By means of modeling possibilities, the authors showed both improvements and deterioration of duration of handover procedure with the use of MIMO in radio systems. In [22], the authors consider a novel adaptive multi-input multioutput (MIMO) semisoft handover technique for the quality of service (QoS). Semisoft handover permits both hard and soft handover advantages for OFDM networks. Specifically, they analyze the semisoft handover combined with the adaptive MIMO mode switching scheme. In [23], the authors implement the Variable Step Size Griffiths (VSSG) algorithm for steering the radiation pattern of the eNodeB with multiple input multiple output (MIMO) antenna's from −90 degrees to +90 degrees. After steering the main beam, the detection is performed using MUSIC algorithm for detecting the UE's located at cell boundaries during handover to provide better signal strength to meet the standards QoS of 4G-LTE. They also compared with capacity of single input single output (SISO) and multiple input multiple output (MIMO). However, above schemes mainly focus on validating the effectiveness of adaptive MIMO soft handover in the femtocell or cell edge networks or showing that the influence of the correlation between the signal qualities of the source and target base station (BS). In addition, they did not consider MIMO and video streaming.

In [14], the authors investigated the potentiality and benefits of a novel vertical-handover algorithm for which both hard and soft handovers are exploited in a dual-mode configuration, and it was compared with the traditional hard approach. Regarding the hard vertical-handover mechanism, the connectivity between the mobile users and the serving network is broken before the connection with a new network is established (namely, "break-before-make"); alternatively, the soft vertical-handover mechanism is "make-before-break" and generally improves the seamless connectivity. The algorithm of [14] aims to maintain seamless connectivity for those users moving in heterogeneous-network environments (i.e., comprised of WLAN hotspots and UMTS base stations), while still guaranteeing the user-QoS requirements. Notably, though, a fully forwarding MN scheme that is based on the MIMO mode from the pAR to the nAR in terms of the handover was not considered for these schemes; furthermore, the selection metric of the wireless technique was not simultaneously considered.

The authors of [24] propose a cross-layer and reactive handover procedure which employs optimized movement detection and address configuration schemes based on the standard specification for HMIPv6 mobility support. For that, they utilize the advantage of link layer notification in the link layer of an AP's protocol stack and the network layer of the AR which has a connection with the AP. However, their assumption that an AP knows the exact AR to which it is attached is strict nowadays and they did not consider MIMO and video streaming.

In [25], the authors present a data rate-guaranteed IP mobility management scheme for fast-moving vehicles with multiple wireless network interfaces. Different from other previous work, they assume the handover initiation is based on the measured data rate rather than the radio signal strength. To guarantee the required data rate, they consider multiple bidirectional IP tunnels locally constructed between the HMIPv6 MAP and the mobile gateway (MG). The packets are distributed in parallel over these tunnels during handover operation, while eliminating the possible delay and packet loss during handover operation. However, they consider not video streaming with MIMO but the UDP-based audio application traffic for the type of the application traffic.

In [26], the authors investigate the potential of applying FMIPv6 in vehicular environments by using IEEE 802.21 Media Independent Handover (MIH) services. With the aid of the lower three layers' information of the MIH enabled MN/MR and the neighboring access networks they design an "Information Element Container" to store static and dynamic L2 and L3 information of neighboring access networks. Plus, they propose a special cache maintained by the MN/MR to reduce the anticipation time in FMIPv6, thus increasing the probability of the predictive mode of operation for a cross-layer mechanism. The lower layer information of the available links obtained by MIH services and the higher layer information such as QoS parameter requirements of the applications are used by a Policy Engine (PE) to make intelligent handover decisions. However, they only consider a network scenario, where one WiMAX (IEEE 802.16) cell and one IEEE 802.11b WLAN Basic Service Set (BSS) are located based on one mobility service provider. Also, they did not consider video streaming with MIMO for the type of the application traffic.

In [27], the authors focus on mobility management at a convergent layer for heterogeneous networks, network layer with mobile Internet Protocols (MIPs), to support VoIP services in wireless heterogeneous networks. They identify four crucial parameters that affect the handover performances of the protocols, depending on the FER in the air link. These are the number of messages exchanged over the air link, the entities involved in the process, the retransmission strategy (maximum number of retransmissions allowed, back-off mechanism, and back-off timer), and the message sizes of the protocols. With one of them, to optimize the handover delay, the authors propose to use the adaptive retransmission proportional to the size of the messages involved in the transactions of the handover process. However, their scheme is not practical for mobile video streaming since the support of VoIP in mobile systems requires low handover latency (i.e., <400 ms) to achieve seamless handovers. Plus, they only focus on network layer handover; therefore, they do not consider link layer detection and retransmissions as well as the impact of correlated errors on the disruption time, error correction mechanisms, processing, and queuing delays.

In [15], the authors proposes a novel architecture called *Integrated InterSystem Architecture* (IISA) based on 3GPP/3GPP2-WLAN interworking models to permit the integration of any type of wireless networks. Furthermore, they propose a mobility management scheme called the *Handoff Protocol for Integrated Networks* (HPINs), which provides QoS guarantees for real-time applications of mobile users moving across various networks. HPIN allows the selection of the best available network at any given time, for both heterogeneous and homogeneous wireless networks. However, they assume a third-party entity called the *interworking decision engine* (IDE) to guarantee the seamless roaming and service continuity required in 4G/NGWNs. The routers extract QoS context information, and according to the context received, the intermediate router reserves corresponding resources and updates the path information.

3. System Architecture

Generally, regarding MIMO-capable, heterogeneous wireless technologies, several heterogeneous wireless networks can coexist; moreover, the Internet serves as a backbone that connects a home network and several heterogeneous visited networks including Wi-Fi and LTE. The home network is where the global IPv6 address (home address) of an MN exists. The IPv6 address that is based on the 48-bit MAC address of the MN is 128 bits and consists of the AR prefix (64 bits) and the Modified EUI-64. The home address is a unicast routable address that has been assigned to the MN and is used as the permanent MN address. Standard IP-routing mechanisms will deliver packets that are destined for an MN-home address. The domain of a visited network comprises several ARs and wireless APs that an MN can connect with [10]. We assume that each AR comprises an interface that is connected to a distinct set of APs and that the same network prefix cannot be assigned to the interface of a different AR; that is, ARs are distinguished by their own prefix. Generally, a CoA can be used to enable an MN so that it can send and receive packets to a Home Agent (HA) or a Correspondent Node (CN); the HA is a router in the MN-home network that the MN has registered its CoA with. While the MN is away from the home network, the HA intercepts the packets that are destined for the MN-home address, encapsulates them, and tunnels them to the MN's registered CoA; furthermore, the association between an MN's home address and a CoA is known as a "binding" for the MN. While away from the home network, an MN registers its new CoA (nCoA) with a home address, whereby the MN performs a binding registration by sending a binding update message to the HA; the HA reply to the MN is in the form of a Binding Acknowledgement message. The CN that can be either mobile or stationary is a peer node that the MN communicates with. The nCoA that is composed of the nAR prefix in a new visited network, and the MAC address of the MN is a unicast routable address that is associated with an MN while a new visited network is being visited. The nCoA is made after the Duplicate Address Detection (DAD) is completed. The DAD corresponds to most of the handover latency because it requires time in the order of seconds to detect whether the nCoA of the MN has been duplicated. Different from [10], the MN in this paper sophisticatedly selects the best wireless technology from among multiple wireless network interfaces (WNICs) and a MIMO forwarding scheme for robust mobile video streaming.

Parallel to the advances of heterogeneous wireless technologies and MIMO modes is the development of a robust mobile-video-streaming paradigm [2–4]; thus, we consider mobile video streaming over MIMO-capable, heterogeneous wireless networks where the AP can forward video packets to other APs with a combination of both the wireless network (i.e., Wi-Fi or LTE) and the MIMO transmission mode (i.e., MUX or DIV) based on the distance and channel quality. Similarly, through an inspection of the relation between the AP and the MN, the MN can also select the wireless technology (i.e., Wi-Fi or LTE) and the MIMO-transmission mode for a robust mobile-video-streaming service. To cover a general pair of wireless networks comprising the MIMO mode and the handover possibility, we designed an appropriate selection metric using the QoS and the QoE.

Based on the extensive evaluations, we obtained the following frequently used pair: a Wi-Fi and MUX mixture is generally used between the AP and MN over a reliable wireless link. Plus, an LTE and DIV mixture is generally used between the oAP and nAP due to the limit regarding the distance and channel quality; however, both cases can only be guaranteed where there is a possibility that the nCoA can be used for a successful handover. We will explain the proposed metric in terms of the covering of the nCoA-resource management, whereby the wireless techniques and the MIMO modes are selected.

4. A Robust Mobile-Video-Streaming Scheme for MIMO-Capable Heterogeneous Networks

In this section, we provide the details of the proposed scheme, whereby an appropriate wireless-technology metric, the MIMO mode, and the temporal reuse of verified tentative CoAs are selected for robust mobile video streaming in MIMO-capable, heterogeneous wireless networks, along with a depiction of the architectural view in Figure 1. For robust mobile video streaming, the MN of the previous visited network selects the "best," according to an appropriate metric, new visited network among all of the wireless technologies and a MIMO mode for the seamless handover whereby a tentative address management is proactively performed by the ARs. For an appropriate metric for the video quality of an encoded sequence, we used the average peak signal-to-noise ratio (PSNR) [28, 29] (i.e., the PSNR based on the luminance (Y) component of video sequences) that is measured in dB and averaged it over the entire duration of the video sequence. For the QoE, we applied the concept of a "temporal quality assessment" [30], whereby the difference of the corresponding pixel values in the two consecutive neighboring frames is first measured to estimate the motion of the objects in the video.

4.1. Metric Selection of the Wireless Technology and the Forwarding Scheme. To choose the "best" wireless technology, a metric that captures the contribution of each wireless technology regarding the mobile-video-quality improvement needs to be defined first with the system state. Let $Q_{w_i}(c_j)$ be the improvement of the mobile-video quality and the QoE at the MN(c_j) when the wireless technology w_i is selected, as follows:

$$Q_{w_i}\left(c_j\right) = \sum_{p=1}^{N} \left(1 - e_{p,w_i}\right) \cdot I_{p,w_i,m_i} \cdot \mathrm{TVM}_p \cdot R_{p,w_i}, \qquad (1)$$

where p means each video frame, N is the total video frames per a group of pictures (GoP) that is included in the MN(c_j), and e_{p,w_i} is the loss probability of the frame p in the wireless technology w_i that is due to latency or channel errors. e_{p,w_i} is given by the following:

$$e_{p,w_i} = \int_{\tau_{w_i}}^{\infty} f\left(t, w_i\right) dt + \left(1 - \int_{\tau_{w_i}}^{\infty} f\left(t, w_i\right) dt\right) \cdot f\left(s\right). \qquad (2)$$

In (2), the first part describes the probability of the late arrival of a video frame, and τ_{w_i} and $f(t, w_i)$ are the remaining

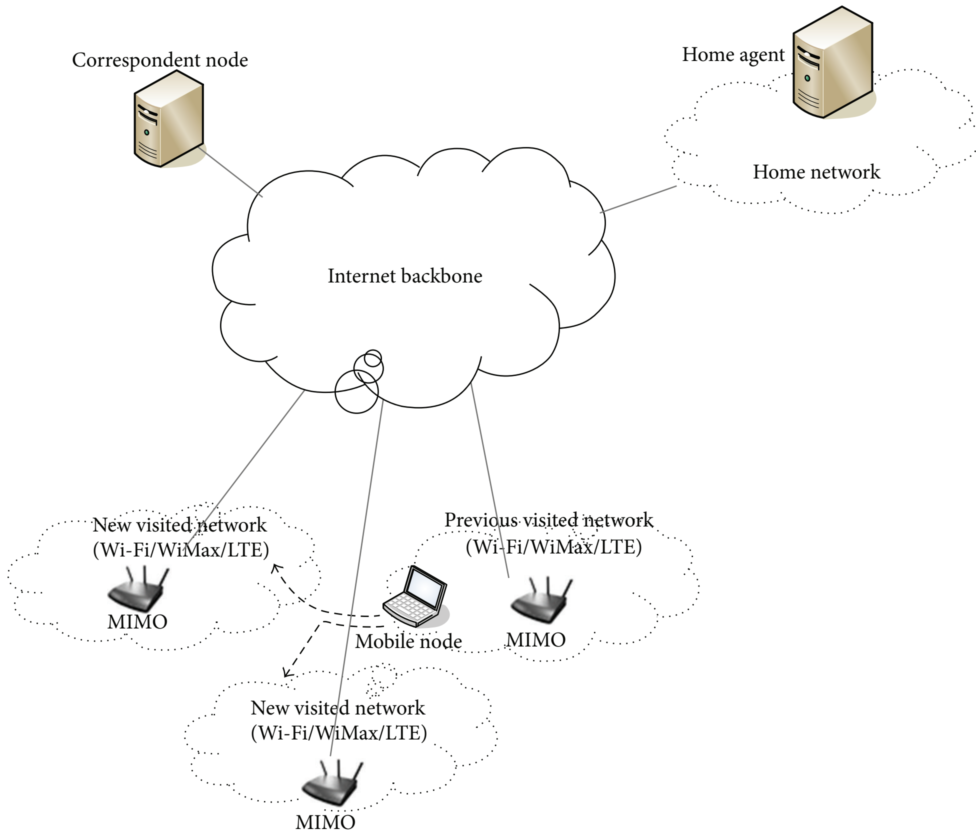

Figure 1: Architectural view of the proposed scheme.

time until the playout deadline and the distribution of the forward trip time in w_i, respectively. The late-arrival probability of a frame corresponds with the following frame-drop probability:

$$\begin{aligned}\int_{\tau_{w_i}}^{\infty} f(t, w_i)\, dt &= 1 - \int_{-\infty}^{\tau_{w_i}} f(t, w_i)\, dt \\ &= 1 - P\left(X \le \tau_{w_i}\right) \\ &= 1 - \left(1 - e^{-(1/4)\tau_{w_i}}\right) = e^{-(1/4)\tau_{w_i}}.\end{aligned} \tag{3}$$

The second part of (2) describes the loss probability (of a frame that is still on time) that is due to the effects of the wireless channel such as noise, fading, and interference; meanwhile, $f(s)$ is a snapshot of the loss probability per each state according to the channel characteristics of Wi-Fi or LTE. The states will be explained in detail during the presentation of the random-mobility model.

Intuitively, mobility causes glitches and stalls of mobile video, and it also causes fast, unpredictable variations of the channel quality that are shown Figure 3. In the case of Wi-Fi, it is only possible for an MN to use mobility within a specific transmission range. For that, we also utilize Figures 4 and 5 of [11–13]. However, different from Wi-Fi case similar with the previous works [11–13], in this paper we extend LTE case as well as Wi-Fi as shown in Figure 7. Figure 4 presents the next four MN states according to the initial MN state (0, 0) and without the MN speed, in a random-walk model. Figure 5 shows all of the nine possible states that are based only on the MN locations according to the random-mobility model. Although the Wi-Fi signal can reach the end of the transmission range, the reception probability is decreased, as shown in Figure 2, because the signal strength is very weak in the boundary of the transmission range; therefore, considering the δ effect shown in Figure 6, it is better for the MN to use other wireless technologies instead of Wi-Fi when the distance between the AP and the mobile MN is larger than 40 m.

If, however, we consider both the direction and the speed of the MN for the random-walk model, the mobile MN should naturally use LTE instead of Wi-Fi for seamless video streaming, as shown in Figure 7; moreover, the possible states can be extended, as shown in Figure 8, with three indexes. The circles indicate the Wi-Fi zones that are expressed by the state "x, y, 0" with a low MN speed, whereas if the MN moves fast toward the cloud boundary with the middle speed, the state "x, y, 1" that represents the Wi-Fi-boundary zone is used. The outlier of the cloud, expressed by the state "x, y, 2," is for LTE and the corresponding quick attainment of a high mobility. Lastly, our systems can be expressed with 27 states ("x, y, z") along with the direction and speed of the MN for both Wi-Fi and LTE. Based on the direction and speed, (1) is used for the selection of a wireless technology by the MN according to the priority that is deemed by the order (i.e., Wi-Fi and LTE) found at the initial location.

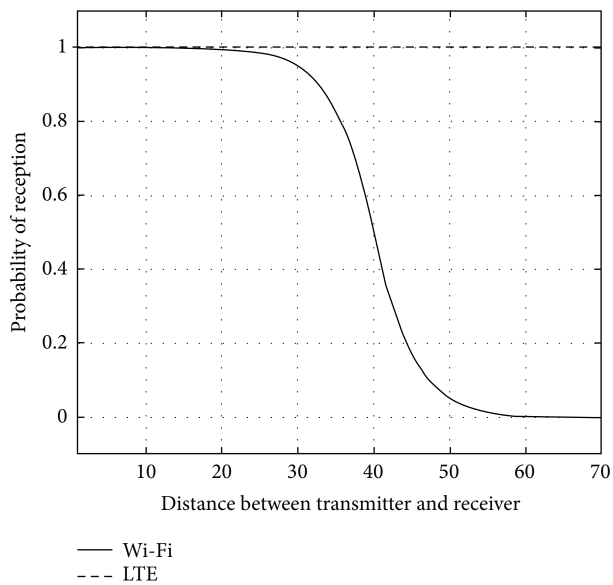

Figure 2: Reception probability under a typical fading model.

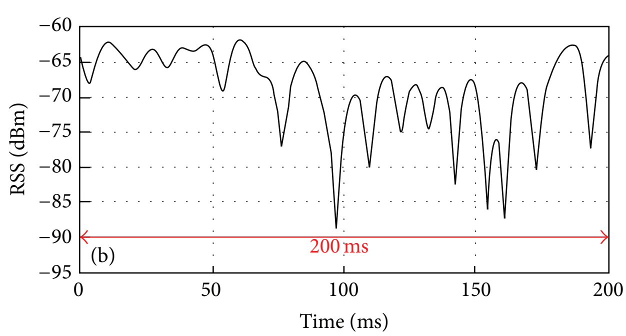

Figure 3: Unpredictable variations of channel quality due to random MN mobility.

I_{p,w_i,m_i} represents the improvement of the mobile-video quality, where the standard metric of video quality, PSNR, is used, if a frame p is received correctly and on time at the wireless technology w_i, and is in consideration of the MIMO-technique mode m_i between the MUX and the DIV. The PSNR is calculated on the frame and is most easily defined via the mean squared error (MSE), when the following noise-free $m \times n$ monochrome image I and its noisy approximation K are given:

$$\begin{aligned} \text{PSNR (dB)} &= 10 \cdot \log_{10}\left(\frac{\text{MAX}_I^2}{\text{MSE}}\right) \\ &= 10 \\ &\cdot \log_{10}\left(\frac{\text{MAX}_I^2}{(1/mn)\sum_{i=0}^{m-1}\sum_{j=0}^{n-1}\left[I(i,j) - K(i,j)\right]^2}\right). \end{aligned} \quad (4)$$

Here, MAX_I is the maximum pixel value of the frame that is possible.

To compute I_{p,w_i,m_i}, we decoded the entire video sequence with a packet that, according to $f(s)$, is missing and then computed the resultant distortion; plus, we recomputed I_{p,w_i,m_i} based on the MIMO mode. We assume that this computation is performed offline at the $\text{MN}(c_j)$ and that the distortion value is marked on each frame.

The DIV provides a long transmission possibility, and it improves the reliability of the wireless link for the same data with multiple antennas. As a result, even a disconnection scenario between two nodes in the DIV mode can form a well-designed forwarding method. In the case of MUX, the different data streams per each antenna can be transmitted between two nodes; therefore, if we use the MUX mode over reliable wireless links, the throughput can be improved very effectively.

For the proposed scheme, we opportunistically selected a MIMO forwarding scheme between the DIV and the MUX using (1); for example, in the following three scenarios, the DIV mode is selected:

(1) Over unreliable wireless link between the pAR and the mobile MN
(2) Far distance beween the pAR and the nAR
(3) Over unreliable wireless link between the nAR and the mobile MN

Furthermore, for the following two scenarios, the MUX mode is selected:

(1) Over reliable wireless links between the pAR and the mobile MN
(2) Over reliable wireless links between the nAR and the mobile MN

R_{p,w_i} is an indicator function that expresses whether it is possible for the wireless technology w_i to service the mobile video frame p with resources; the resources are the unused IP addresses that can be used for a temporal CoA_{w_i} by a visiting MN (see Section 4.2). We define $R_{p,w_i} = 1$ if the mobile video frame p is serviced at the wireless technology w_i, or otherwise, it is defined as 0.

TVM_p is calculated as the mean-square-value log of the difference between two consecutive frames (F_{p-1} and F_p) of the video (measured in dB) for the QoE [30]. The wireless technology w_i and the MIMO mode that maximizes the mobile video quality and the QoE improvement with the temporal CoA is therefore chosen for the proposed scheme. This is given with (5), as follows:

$$\max_{w_i} \quad Q_{w_i}\left(c_j\right). \quad (5)$$

4.2. Tentative Address Management (TAM). Unlike the previous works [10–13], each Access Router (AR), such as the nAR and the pAR, manages each tentative address pool containing the unused IP addresses that can be used as a temporal CoA by a visiting MN regarding the wireless technology w_i; these addresses are denoted by the verified tentative CoAs_{w_i}s. The AR ensures that the verified tentative CoAs_{w_i}s that are registered in the pool are not currently used by the other

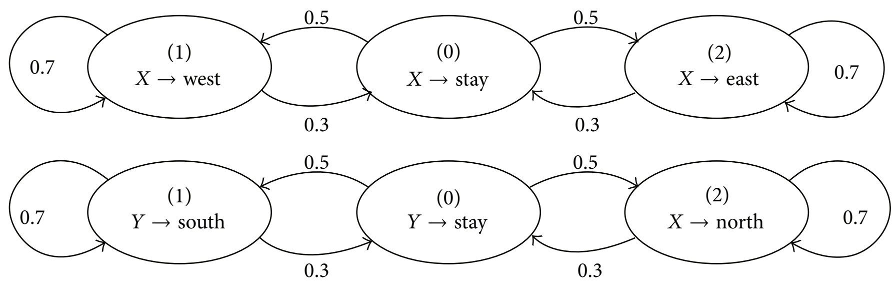

Figure 4: Flow chart of the probabilistic version of random-walk model.

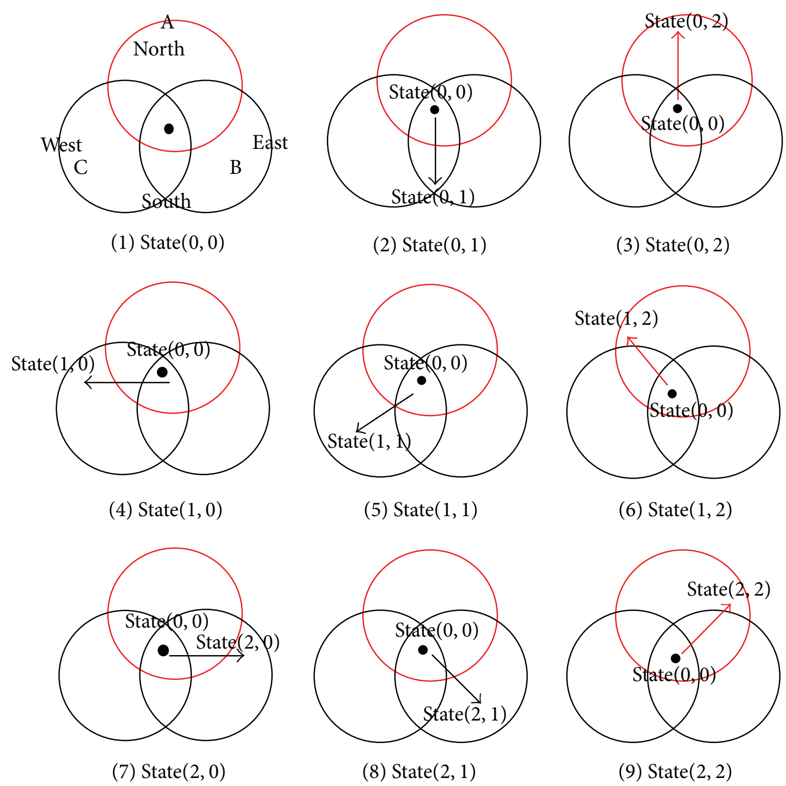

Figure 5: Possible next states of MN regarding random-walk model.

MNs by performing the DAD for each verified tentative address periodically. Basically, we assumed that each AR maintains as many of the verified tentative CoAs$_{w_i}$s according to the number of neighbor ARs in each of the possible wireless technologies. A verified tentative CoA$_{w_i}$ is deleted from the pool if it is proven that it is being used by another node through the DAD. If the number of verified tentative CoAs$_{w_i}$s is smaller than the number of neighbor ARs, then the router adds new verified tentative $CoAs_{w_i}$s into the pool by searching the available IP addresses using the already used MAC address of the other MNs and the AR prefix. In terms of the wireless technology w_i, we assumed that a modified Neighbor Router Advertisement (mNRA$_{w_i}$) including the several nonoverlapping verified tentative CoAs$_{w_i}$s can be periodically sent and received between each of the routers; as a result, each router of the wireless technology w_i can manage the available verified tentative CoAs$_{w_i}$s per the wireless technology of the access networks of a one-hop neighbor. Generally, the NRA contains router information [7], and we modified the reserved field in the NRA to include the several verified tentative CoAs$_{w_i}$s. When the pAR receives the modified Router Solicitation for Proxy (mRtSolPr$_{w_i}$) from the MN, it informs the modified Proxy Router Advertisement (mPrRtAdv$_{w_i}$) containing several verified tentative CoAs$_{w_i}$s about the neighboring access networks of the MN before it moves to one of the visited networks. The MN then sends a Last Packet (LP) message to the pAR informing it of the MN handover and moves to one of the new visited networks from the previous visited network. After the MN handover, the corresponding verified tentative CoA$_{w_i}$ of the new visited network that is included in the modified Fast Neighbor Advertisement (mFNA$_{w_i}$) message is used by the

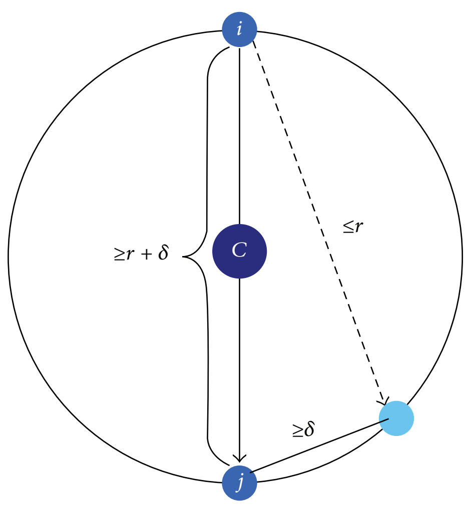

Figure 6: Distance relationship between the transmitter and a receiver.

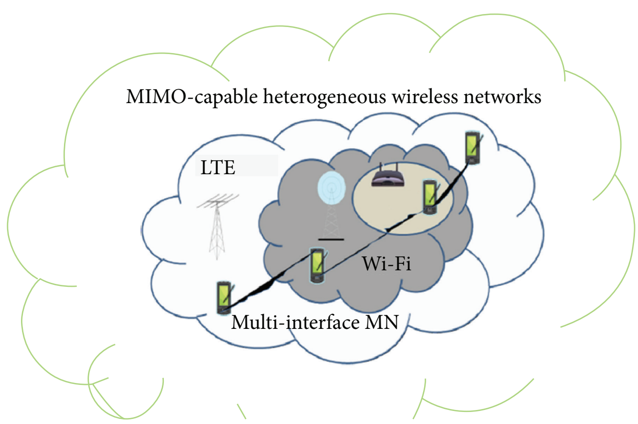

Figure 7: Mobile node (MN) seamlessly moving between different technologies.

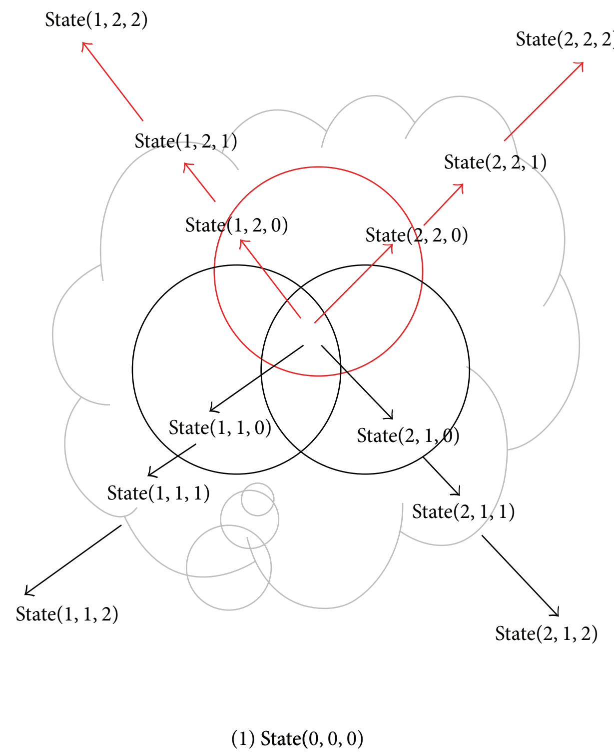

Figure 8: Extended random-walk model with the direction and speed of the MN.

MN to generate a fast IP connectivity that enables the MN to perform a binding update using the verified tentative CoA_{w_i}, that is, the $\mathrm{FBU1}_{w_i}$ and $\mathrm{BAcK1}_{w_i}$. After the MN acquires its original CoA_{w_i} that contains its own MAC address by performing the DAD, the fast IP connectivity for which the verified tentative CoA_{w_i} is used is returned to the normal IP connectivity for which the original CoA_{w_i} is used. The recycling of the verified tentative CoAs_{w_i}s is possible because these verified tentative CoAs_{w_i}s are temporarily used by the MNs in the wireless technology w_i for the reduction of the handover delay until the MN completes the binding updates through the use of its new original CoA_{w_i}, that is, the $\mathrm{BU2}_{w_i}$ and $\mathrm{BAcK2}_{w_i}$. Figure 9 shows the handover procedure of the proposed scheme for mobile video streaming in terms of MIMO-capable, heterogeneous wireless networks; using L2-layer triggers that are based on the MIH functionality [31], the MN detects mobility and the proposed metric of (1) is considered for seamless video streaming.

5. Performance Evaluation

To evaluate the performances of the mobile video streaming of our proposed scheme and the other schemes, an NS-3 simulation was performed with a variety of parameters (Table 1) such as coverage of AR, beacon interval, traffic type, and link delay. Figure 10 shows the network topology that was used in our simulation for which several entities including HA, CN, AR, and MN were used. The link delay that contains propagation delay, processing delay, and queuing delay was assigned to 5 ms for the MN-AR links and the AR-Router links and 10 ms for the Router-CN/HA links and the AR-AR links. The velocity at which the MN is moving across the network is up to 30 m/s. We used 2 Mbps standard video traffic such as Carphone, Foreman, and Mother and Daughter [32] that are constantly sent from the CN to the MN. For the performance measures for the proposed scheme and the other schemes, we used the average PSNR for the video quality of an encoded sequence, the handover delay, and the video delay.

5.1. Handover Delay under Perfect Prediction. Figure 11 shows the video-streaming delay based on handover schemes such as MIPv6, HMIPv6, FMIPv6, eFMIPv6 [10], the hybrid scheme [14], HPIN [15] and the proposed scheme when the MNs move according to Figure 10. The video-streaming delay of the proposed scheme was prominently reduced and is therefore an improvement over the previous work [14]. This improvement is a direct result of the ability of the MN

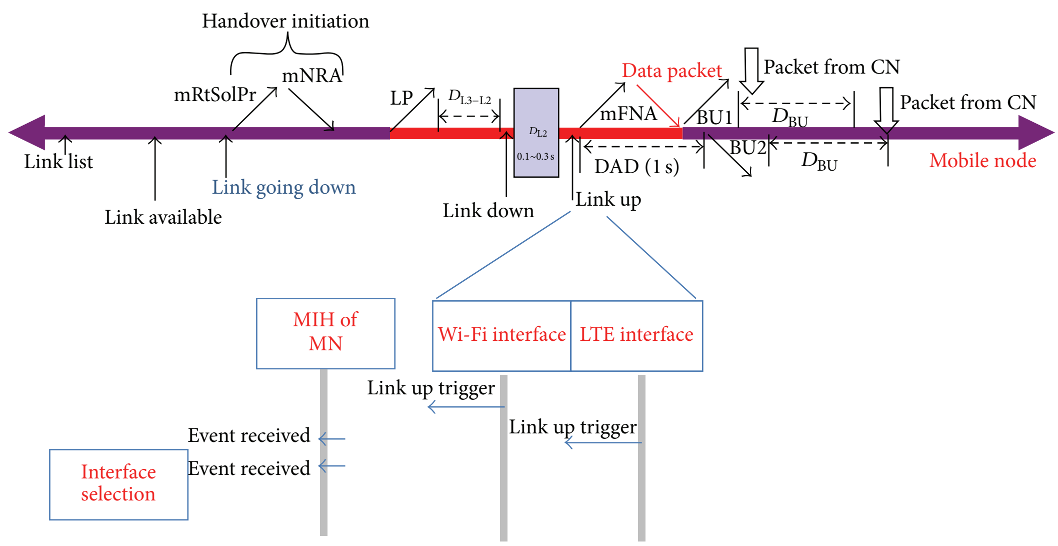

Figure 9: Handover procedure of the proposed scheme.

Table 1: Simulation properties.

Parameter	Value
Coverage of AR	120 m
Beacon interval	0.1 s
Traffic type	2 Mbps video traffic
Link delay (MN-AR links and AR-Router links)	5 ms
Link delay (Router-CN/HA links and AR-AR links)	10 ms
Velocity	1 m/s to 15 m/s
Channel model	Rayleigh fading
Simulation time	180 s
Video sequence	Carphone, Foreman, Mother and Daughter
Radius of LTE and WLAN	1000 m, 50 m
LTE and WLAN bandwidth	10 MHz, 20 MHz
Frequency of WLAN	2.412 GHz
Tx power	0.0134 W
Threshold (dBm) of LTE and WLAN	−64, −60

whereby it can receive video packets from the pAR until the MN sends the LP to the pAR, and the MN can also receive video packets as soon as it moves to new visited networks by using verified tentative CoAs that are based on the appropriate selection metric of the wireless technology with the MIMO-transmission mode; however, the Hierarchical MIPv6 (HMIPv6) [8] is proposed for the handover-latency enhancement in the local mobility region. We therefore focused on FMIPv6 enhancement in the proposed scheme to cover the global mobility as well as the local mobility. Even though the performance of HPIN [15] is very similar with the proposed scheme, the HPIN is not practical due the strong assumption of centralized scheme.

5.2. Handover Delay under Imperfect Prediction. To compare our proposed scheme with the hybrid scheme and eFMIPv6 in consideration of an imperfect handover prediction, we used the following mobility models: the random-walk model, the city section model, and the linear-walk model [33]. First, we analyzed and simulated the hybrid scheme, eFMIPv6, and our scheme using a random-walk model. It is useful to understand mobility patterns according to direction and speed, so unlike the previous work [10], we applied speed as well as direction for the random-walk model.

Figure 8 shows an example among a total of 27 states that are derived by the random-walk model whereby the combination of each x, y, and z state is used. Each state represents the direction (north, south, east, west, north-east, north-west, south-east, south-west, and stay) and the speed.

We randomly located the MN in a part of the overlapping area of three circles, as shown in Figure 5, and this area is a common part of the link-going-down range of each of the visited networks. The MN randomly chooses one of the initial 27 states with the same probability, followed by its changing into one of the next states. Regarding Figure 5, we assumed that Area A is the pAR of the MN and that the MN immediately

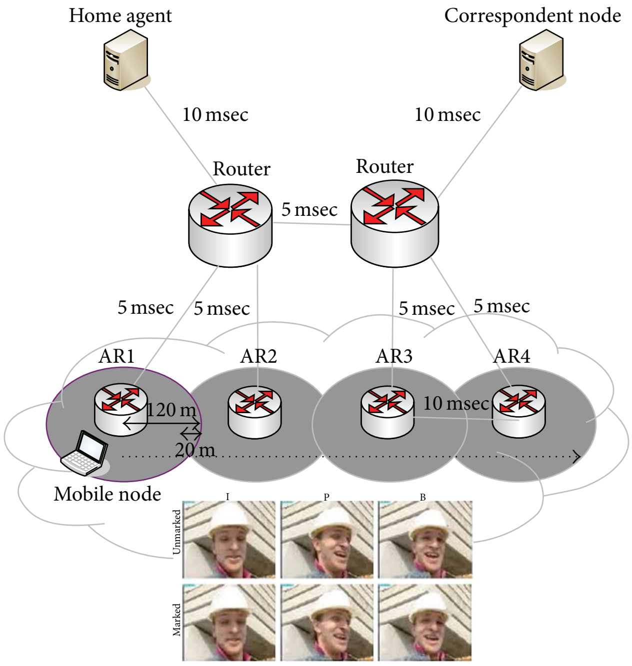

FIGURE 10: Simulation network topology.

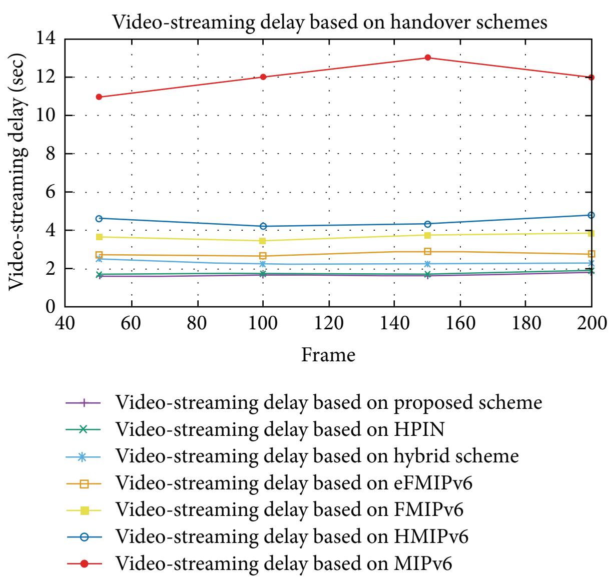

FIGURE 11: Video-streaming delay based on handover and forwarding schemes.

predicts a move to Area C. In this case, the handover succeeds if the MN actually hands over to Area C; otherwise, it fails. We first analyzed the handover-success probability (P_s) and the handover-failure probability (P_f) according to the MN initial state and based on the transition probability; then, we simulated the random-walk procedure with a sample size of 10,000 to verify the result of the analysis. P_s can be calculated when the MN moves to one of the following states in Area C: State$(1, 1, 0)$, State$(0, 1, 0)$, State$(2, 1, 0)$, State$(1, 1, 1)$, State$(0, 1, 1)$, State$(2, 1, 1)$, State$(1, 1, 2)$, State$(0, 1, 2)$, and

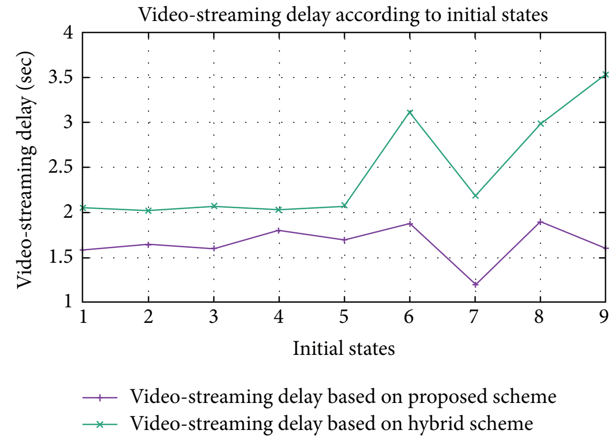

FIGURE 12: For the random-walk model, the video-streaming delay according to the initial states.

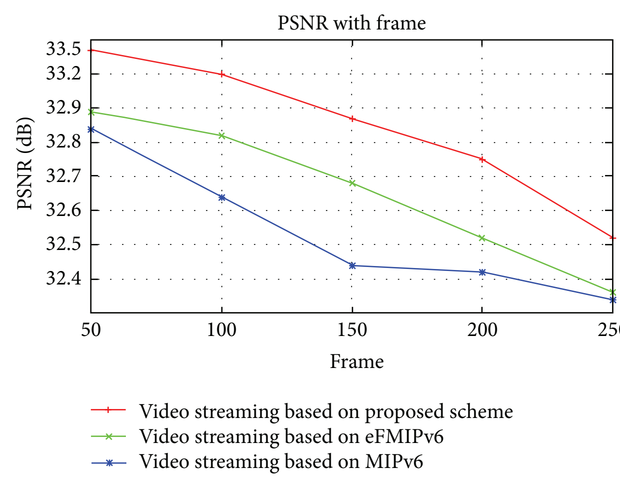

FIGURE 13: Peak signal-to-noise ratio (PSNR) with frame.

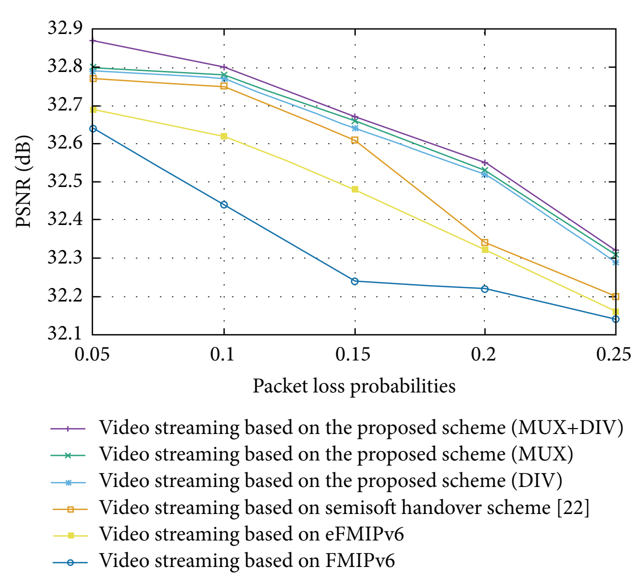

FIGURE 14: Peak signal-to-noise ratio (PSNR) with packet loss probabilities.

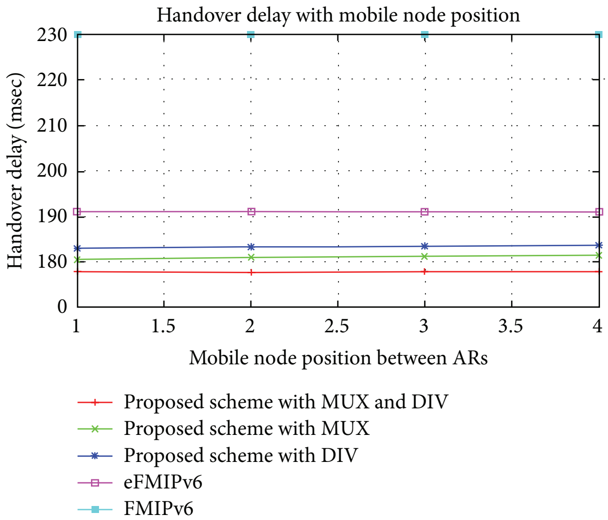

Figure 15: Handover delay with MN position.

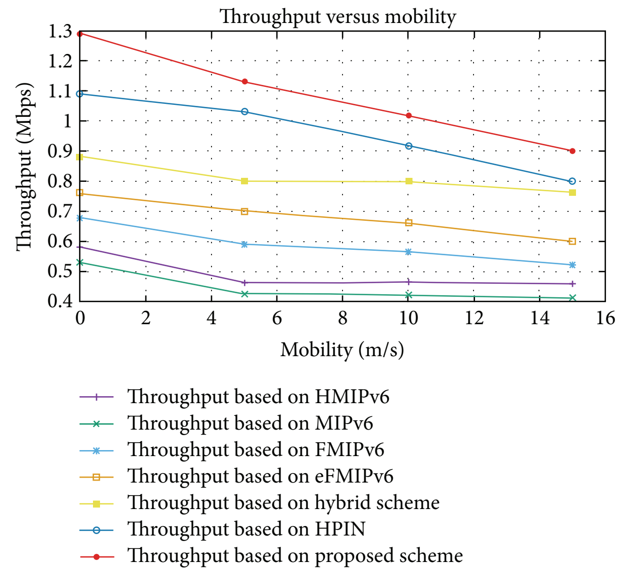

Figure 16: Throughput.

State(2, 1, 2). P_f can be calculated when the MN performs handovers for areas other than Area C.

Figure 12 shows the video-streaming delays of our proposed scheme and the hybrid scheme according to the initial state; the initial states are possible locations for the MN. As expected, our scheme provides a delay that is shorter than that of the hybrid scheme because it is more robust in handover-failure situations under a dynamic-mobility environment, and it forwards the video packet quickly by using the proposed metric of (1).

Figures 13, 14, and 15 show that the proposed scheme achieves a higher PSNR and a lower handover latency with the MN position compared with the other schemes; that is, when the transmitted flows are mobile video streams, the proposed scheme selects the proper wireless network w_i that comprises the temporal CoAs_{w_i} and the MIMO mode to minimize not only the handover delay but also the video delay. Figure 16 shows throughput gain of the proposed scheme with MIMO Tx techniques.

Additionally, Table 2 shows the complexity analysis of the proposed scheme and semisoft handover scheme inspects of graph theory. Actually, since our work is for each user's n-hop of multihop network with MUX scheme, complexity comparison with semisoft handover scheme seems to be ironic. n means the number of users (nodes) in n-hop neighborhood MIMO network and m is the number of relations (edges) in n-hop neighborhood MIMO network. Also, N means the number of every user (nodes) in whole MIMO network and M means the number of every relation (edges) in whole MIMO network.

Inspects of comparison analysis between the proposed scheme and semisoft handover scheme, our proposed scheme is seamless and practical with even partial information compared with the semisoft handover scheme with global information, since n is the number of a few MUX capable nodes in the proposed scheme while N is the number of total nodes of whole network in semisoft handover scheme.

Table 2: Complexity analysis.

	Semisoft handover [22]	Proposed scheme
Time complexity	$O(N+M)$	$O(n+m)$
Space complexity	$O(N)$	$O(n+m)$

6. Conclusion

With the remarkable development of wireless technologies and mobile video streaming, the need to support a robust mobile-video-streaming service that is based on a seamless handover in MIMO-capable, heterogeneous wireless technologies continues to grow. In this paper, we consider robust mobile video streaming over several heterogeneous wireless networks, whereby the appropriate selection metric of the wireless technology with a verified tentative CoA and the MIMO mode are used at the MN to maximize video quality and minimize the video and handover delays for a robust mobile-video-streaming service. Through a performance evaluation that is based on an extended random-walk model for which the direction and speed of the MN are used, we show that our proposed scheme is a mechanism that is more robust than the other schemes for mobile video streaming.

Competing Interests

The authors declare that there is no conflict of interests regarding the publication of this article.

Acknowledgments

This research was supported by the Basic Science Research Program through the National Research Foundation of Korea (NRF) that is funded by the Ministry of Science, ICT & Future Planning (NRF-2014R1A1A1003562).

References

[1] D. Gesbert, M. Shafi, D.-S. Shiu, P. J. Smith, and A. Naguib, "From theory to practice: an overview of MIMO space-time coded wireless systems," *IEEE Journal on Selected Areas in Communications*, vol. 21, no. 3, pp. 281–302, 2003.

[2] S. Aditya and S. Katti, "FlexCast: graceful wireless video streaming," in *Proceedings of the 17th Annual International Conference on Mobile Computing and Networking (MobiCom '11)*, ACM, Las Vegas, Nev, USA, September 2011.

[3] S. Jakubczak and D. Katabi, MIT, SoftCast + Scalable Robust Mobile Video, ACM Mobicom, 2011.

[4] Cisco Visual Networking Index.

[5] H. Fathi, R. Prasad, and S. Chakraborty, "Mobility management for VoIP in 3G systems: evaluation of low-latency handoff schemes," *IEEE Wireless Communications*, vol. 12, no. 2, pp. 96–104, 2005.

[6] R. Koodli, "Fast handovers for mobile IPv6 (FMIPv6)," IETF, RFC 4068, 2005.

[7] D. B. Johnson, C. E. Perkins, and J. Arkko, "Mobility support in IPv6," RFC 3775, IETF, 2004.

[8] H. Soliman, C. Castelluccia, K. E. Malki, and L. Bellier, "Hierarchical Mobile IPv6 Mobility Management (HMIPv6)," IETF RFC 4140, 2005.

[9] S. Gundavelli, K. Leung, V. Devarapalli, K. Chowdhury, and B. Patil, "Proxy Mobile IPv6, RFC5213," August 2008.

[10] H. Oh, "A robust mobile video streaming in heterogeneous emerging wireless systems," *KSII Transactions on Internet and Information Systems*, 2012.

[11] H. Oh, J. Yoo, C.-K. Kim, and S. H. Ahn, "VMIPv6: a seamless and robust vehicular MIPv6 for vehicular wireless networks and vehicular intelligent transportation systems (V-Winet/V-ITS)," *Journal of Information Science and Engineering*, vol. 26, no. 3, pp. 833–850, 2010.

[12] H. Oh, K. Yoo, J. Na, and C. Kim, "A seamless handover scheme in IPv6-based mobile networks," *International Journal of Ad Hoc and Ubiquitous Computing*, vol. 4, no. 1, pp. 54–60, 2009.

[13] H. Oh, K. Yoo, J. Na, and C.-K. Kim, "A robust seamless handover scheme for the support of multimedia services in heterogeneous emerging wireless networks," *Wireless Personal Communications*, vol. 52, no. 3, pp. 593–613, 2010.

[14] A. M. Vegni and E. Natalizio, "A hybrid (N/M)CHO soft/hard vertical handover technique for heterogeneous wireless networks," *Ad Hoc Networks*, vol. 14, pp. 51–70, 2014.

[15] C. Makaya and S. Pierre, "An architecture for seamless mobility support in IP-based next-generation wireless networks," *IEEE Transactions on Vehicular Technology*, vol. 57, no. 2, pp. 1209–1225, 2008.

[16] K. Sundaresan and R. Sivakumar, "Routing in ad-hoc networks with MIMO links," in *Proceedings of the 13th IEEE International Conference on Network Protocols (ICNP '05)*, pp. 85–95, IEEE, Boston, Mass, USA, November 2005.

[17] J.-S. Wang and J.-S. Sheu, "Study of handover techniques for 4G network MIMO systems," in *Proceedings of the International Conference on Electronics, Signal Processing and Communication Systems*, 2013.

[18] S. Cho and J.-W. Choi, "Downlink soft handover using multi-cell MIMO for 4G-LTE smart-phones," in *Proceedings of the IEEE International Conference on Consumer Electronics (ICCE '14)*, pp. 207–208, Las Vegas, Nev, USA, January 2014.

[19] H. Lee, H. Lee, and D.-H. Cho, "Novel handover decision method in wireless communication systems with multiple antennas," in *Proceedings of the IEEE 64th Vehicular Technology Conference (VTC '06)*, pp. 2099–2103, Montreal, Canada, September 2006.

[20] V. Jungnickel, K. Manolakis, L. Thiele, T. Wirth, and T. Haustein, "Handover sequences for interference-aware transmission in multicell MIMO networks," in *Proceedings of the International ITG Workshop on Smart Antennas (WSA '09)*, February 2009.

[21] S. A. Kravchuk, "Research of influence of multiantenna technology MIMO on realisation of handover in cellular radioaccess systems," in *Proceedings of the 21st International Crimean Conference on Microwave & Telecommunication Technology (CriMiCo '11)*, pp. 353–354, Sevastopol, Ukraine, September 2011.

[22] J.-T. Lim and D.-H. Cho, "Gain analysis of adaptive MIMO semisoft handover in LTE-OFDM systems," in *Proceedings of the IEEE 81st Vehicular Technology Conference (VTC Spring '15)*, pp. 1–5, Glasgow, UK, May 2015.

[23] B. Megha and Y. S. Lalitha, "Downlink capacity improvement for LTE using multi-cell MIMO during handover," *International Journal of Innovative Research in Science, Engineering and Technology*, 2015.

[24] Y.-H. Han, J. Choi, and S.-H. Hwang, "Reactive handover optimization in IPv6-based mobile networks," *IEEE Journal on Selected Areas in Communications*, vol. 24, no. 9, pp. 1758–1772, 2006.

[25] J.-T. Park and S.-M. Chun, "QoS-guaranteed IP mobility management for fast-moving vehicles with multiple network interfaces," *IET Communications*, vol. 6, no. 15, pp. 2287–2295, 2012.

[26] Q. B. Mussabbir, W. Yao, Z. Niu, and X. Fu, "Optimized FMIPv6 using IEEE 802.21 MIH services in vehicular networks," *IEEE Transactions on Vehicular Technology*, vol. 56, no. 6, pp. 3397–3407, 2007.

[27] H. Fathi, S. S. Chakraborty, and R. Prasad, "Optimization of mobile IPv6-based handovers to support VoIP services in wireless heterogeneous networks," *IEEE Transactions on Vehicular Technology*, vol. 56, no. 1, pp. 260–270, 2007.

[28] D. Salomon, *Guide to Data Compression Methods*, Springer, Berlin, Germany, 2002.

[29] PSNR, https://en.wikipedia.org/wiki/Peak_signal-to-noise_ratio.

[30] A. J. Chan, A. Pande, E. Baik, and P. Mohapatra, "Temporal quality assessment for mobile videos," in *Proceedings of the 18th Annual International Conference on Mobile Computing and Networking (Mobicom '12)*, pp. 221–232, Istanbul, Turkey, 2012.

[31] Y. Y. An, B. H. Yae, K. W. Lee, Y. Z. Cho, and W. Y. Jung, "Reduction of handover latency using MIH services in MIPv6," in *Proceedings of the 20th International Conference on Advanced Information Networking and Applications (AINA '06)*, pp. 229–234, IEEE, Vienna, Austria, April 2006.

[32] YUV Sequence, http://trace.eas.asu.edu/yuv/.

[33] T. Camp, J. Boleng, and V. Davies, "A survey of mobility models for ad hoc network research," *Wireless Communications and Mobile Computing*, vol. 2, no. 5, pp. 483–502, 2002.